MULTI-BODY TRAJECTORY DESIGN IN THE EARTH-MOON REGION UTILIZING POINCARÉ MAPS

by

Paige A. Whittington

A Thesis

Submitted to the Faculty of Purdue University

In Partial Fulfillment of the Requirements for the degree of

Master of Science in Aeronautics and Astronautics

School of Aeronautics and Astronautics

West Lafayette, Indiana

May 2022

THE PURDUE UNIVERSITY GRADUATE SCHOOL
STATEMENT OF COMMITTEE APPROVAL

Dr. Kathleen C. Howell, Chair

School of Aeronautics and Astronautics

Dr. Diane C. Davis

a.i. solutions, Inc.

Dr. James M. Longuski

School of Aeronautics and Astronautics

Approved by:

Dr. Gregory A. Blaisdell

To my family that always encourages me to reach for the stars

ACKNOWLEDGMENTS

I want to first thank my family who have always encouraged me to push the boundaries of my potential. My grandparents, Al and Sally, introduced me to the world of space exploration through trips to NASA's Kennedy Space Center in elementary school. To a child, space is a fantastical story, but the encouragement of my parents, Paula and Gary, as well as my sister, Jenna, helped me understand that it is a reality I could one day touch. Their unwavering support allowed me to turn my dreams into reality through dedication, perseverance, and love.

I also want to thank my advisor, Professor Kathleen Howell. Your excellent teaching and ideas have enabled me to grow as a researcher, and I am grateful for the time I have spent learning in your research group. I hope to use the skills and knowledge I have learned under you to inspire future women in aerospace engineering as you have done.

I am very grateful to my friends and colleagues in the Multi-Body Dynamics Research Group who provided me continuous advice over the years. You are all extremely talented and kind people who I had the privilege of bouncing ideas off of and learning through your research endeavors. I wish you the best in your personal and professional lives.

I also wish to express my appreciation for the internship experiences I was provided at NASA's Johnson Space Center through USRA, CACI, and the Pathways Program. These opportunities allowed me to apply my knowledge from graduate school, learn alongside field professionals, and understand the reality of the space industry first hand.

Finally, I would like to thank my committee members, Professor James Longuski and Dr. Diane Davis, who took the time to review my thesis and provide feedback. I would additionally like to recognize the funding for this research provided by the National Science Foundation Graduate Research Fellowship Program (GRFP) under grant number DGE-1842166.

TABLE OF CONTENTS

LIST OF TABLES

LIST OF FIGURES

ABSTRACT

The 9:2 lunar synodic resonant near rectilinear halo orbit (NRHO) is the chosen orbit for the Gateway, a future lunar space station constructed by the National Aeronautics and Space Administration (NASA) as well as several commercial and international partners. Designing trajectories in this sensitive lunar region combined with the absence of a singular systematic methodology to approach mission design poses challenges as researchers attempt to design transfers to and from this nearly stable orbit. This investigation builds on previous research in Poincaré mapping strategies to design transfers from the 9:2 NRHO using higher-dimensional maps and maps with non-state variables. First, Poincaré maps are applied to planar transfers to demonstrate the utility of hyperplanes and establish that maps with only two or three dimensions are required in the planar problem. However, with the addition of two state variables, the spatial problem presents challenges in visualizing the full state. Higher-dimensional maps utilizing glyphs and color are employed for spatial transfer design involving the 9:2 NRHO. The visualization of all required dimensions on one plot accurately reveals low cost transfers into both a 3:2 planar resonant orbit and an L_2 vertical orbit. Next, the application of higher-dimensional maps is extended beyond state variables. Visualizing time-of-flight on a map axis enables the selection of faster transfers. Additionally, glyphs and color depicting angular momentum rather than velocity lead to transfers with nearly tangential maneuvers. Theoretical minimum maneuvers occur at tangential intersections, so these transfers are low cost. Finally, a map displaying several initial and final orbit options, discerned through the inclusion of Jacobi constant on an axis, eliminates the need to recompute a map for each initial and final orbit pair. Thus, computation time is greatly reduced in addition to visualizing more of the design space in one plot. The higher-dimensional mapping strategies investigated are relevant for transfer design or other applications requiring the visualization of several dimensions simultaneously. Overall, this investigation outlines Poincaré mapping strategies for transfer scenarios of different design space dimensions and represents initial research into non-state variable mapping methods.

1. INTRODUCTION

Thirty-nine years is the time it took humanity to progress from the first person in space in 1961 to establishing a permanent presence in low Earth orbit (LEO) with the first International Space Station (ISS) crew in 2000 [1], [2]. Twenty-two years later in 2022, the world is ready to establish a residence beyond Earth orbit. The planned multinational Artemis missions will return humans to the surface of the Moon and establish the Gateway lunar space station [3]. These sixty-one years of humans in space have been accompanied by drastic improvements in computing technology and in-depth research into astrodynamics. This development in computation power has enabled advanced modeling of dynamical motion in space, thus, facilitating the search for low cost and low time-of-flight pathways through space that can be reliably utilized as humans permanently move beyond LEO.

1.1 Motivation

For the Artemis missions, the Gateway is planned to be a hub for lunar activity. Its orbit, the 9:2 lunar synodic resonant near rectilinear halo orbit (NRHO), is designed to provide access to the Moon and the Earth as well as to minimize eclipses to ensure constant communication and solar power. Additionally, this orbit has a perilune above the Moon's north pole, so the majority of time in the orbit is spent in view of the Moon's south pole, enabling nearly constant communication for lunar south pole missions [4], [5]. For this orbit to serve its planned purpose, it is essential for spacecraft to be able to enter and depart the 9:2 NRHO from various orbits and energy levels.

To obtain multiple routes into and out of the 9:2 NRHO, a network of pathways through space and transfers with the NRHO must be constructed. The Gateway's orbit is not able to be modeled as a two-body orbit, so a higher-fidelity model, the Circular Restricted Three-Body Problem, is utilized. To design transfers within this model, adequate tools are needed that are informed by mission constraints. The use of maps to visualize transfer options is prevalent throughout planar transfer design; however, spatial orbits possess additional dimensions that require alternative visualization strategies. Additionally, for crewed missions to and from the Gateway, transfer time is an important consideration. However, maneuver

cost is frequently of greater consequence for robotic missions. This nearly stable, 6.55 day NRHO has manifolds – structures than approach and depart an orbit at no cost – that remain in its vicinity for several revolutions. CubeSat or lander missions interested in reducing ΔV benefit from utilizing these structures. Contrarily, crewed missions benefit from impulsive maneuvers to leave the 9:2 NRHO without spending a week or more departing it. Both impulsive departure trajectories and manifolds represent potential intermediate transfer segments that warrant further investigation.

1.2 Previous Contributions

1.2.1 Multi-Body Dynamics

The study of the n-body problem started hundreds of years ago with scientists attempting to derive an accurate model to explain and predict the motion of the stars and planets. A fundamental development occurred in the early 1500's with Copernicus's introduction of the first heliocentric model of the universe, representing a shift in thinking away from a geocentric universe [6]. Several decades later, Kepler improved this model by proposing that planetary orbits are elliptical, not circular [7]. However, it was not until Isaac Newton developed his laws of motion and theory of gravitation, published in *Principia* in 1687, that Newton derived Kepler's three laws of planetary motion [8], [9]. These laws are fundamental in the representation of two-body, or Keplerian, orbits.

In 1722, Leonhard Euler introduced the Circular Restricted Three-Body Problem, built upon a rotating reference frame [10]. This medium-fidelity model possesses equilibrium solutions not present in the n-body problem and enables motion nonexistent in the two-body problem. The accuracy and usefulness of the three-body problem was demonstrated in 1772 when Joseph Lagrange proclaimed the existence of triangular libration points and correctly predicted, 134 years before they were confirmed, that asteroids would exist at these points in the Sun-Jupiter system [7].

The periodic motion available in the CR3BP has been validated and demonstrated via several flown missions. In 1978, International Sun-Earth Explorer-3 (ISEE-3) became the first spacecraft to use a libration point periodic orbit, a Sun-Earth L_1 halo, constructed in the

CR3BP. Other missions to Sun-Earth L_1 multi-body orbits include Solar Heliosphere Observatory (SOHO), Advanced Composition Explorer (ACE), and Genesis [11]. The ARTEMIS mission, launched in 2007, was the first mission to stationkeep Earth-Moon Lagrange point orbits [12]. Most recently, the James Webb Space Telescope, launched in 2021, is currently in a Sun-Earth L_2 halo [13]. Named in 1968 by Robert Farquhar, halo orbits are found in spatial families near each of the three collinear Lagrange points. As calculated by Howell, these orbit families persist for all systems (for values of mass ratios, μ, between 0 and 1), and the L_2 and L_3 halo families possess stable orbits for all values of μ [14]. For this investigation, the L_2 halo family in the Earth-Moon system is of specific interest.

1.2.2 Poincaré Maps

Poincaré mapping strategies have been used by many researchers to design transfers between periodic orbits in the three-body problem. As emphasized by Howell, modern mapping strategies are possible due to the development of computers [15]. This increase in available technology as well as easier access to personal computers with such computational power has resulted in the ability to improve mapping strategies and design novel transfers. Researchers frequently leverage two-dimensional maps for planar transfer design in the CR3BP. Examples of planar transfers constructed with two- and-three dimensional maps include Koon et al. [16], Vaquero [17], and Parker et al. [18] among others.

For spatial transfer design, a map requires a minimum of four state variables to visualize the full state. Successful spatial transfer design is possible using maps with a subset of the the required variables; however, such strategies limits the visualization of the design space. One example of the ability to generate spatial transfers in this manner is presented by Mar and Howell [19]. The visualization of greater than three dimensions has been investigated by various researchers. The space plus color method advocated by Geisel [20] as well as Patsis and Zachilas [21] provides a four-dimensional map. These maps display the full state for spatial transfers with a fixed Jacobi constant value throughout. Glyphs, or arrows, added to scatter points also display more than three variables on one map. Bolliger [22] and Haapala [23] used glyphs to generate initial guesses for spatial transfers. Additionally, Haapala and

Howell employed vector-chain glyph maps to visualize six state variables and locate periodic orbits from periapse maps [24]. In addition to the construction of transfers between two orbits, Poincaré maps have been applied to visualize escape and capture trajectories. Davis used color to distinguish between these regions on a periapse map to create trajectories that transit through the P_2 region [25]. Bonasera and Bosanac also created color coded periapse maps but with the aid of unsupervised learning techniques to categorize disparate regions on their maps [26], [27]. While useful for identifying geometries, their methodology requires large computational power and time and is not informed by mission constraints.

1.3 Thesis Overview

This investigation builds upon previous Poincaré mapping strategies to design transfers in the Earth-Moon region in the Circular Restricted Three-Body Problem. Higher-dimensional maps are generated to select initial guesses for spatial transfers originating from the 9:2 lunar synodic resonant near rectilinear halo orbit (NRHO). Alternative maps displaying non-state variables are analyzed and used to construct planar and spatial transfers. This document is organized as follows:

- **Chapter 2:** Background – Circular Restricted Three-Body Problem – The n-body problem is introduced. Due to the absence of an analytical solution in the n-body problem, a medium-fidelity model, the Circular Restricted Three-Body Problem (CR3BP), is introduced to examine the motion of spacecraft under the influence of two larger primaries. The CR3BP assumptions, equations of motion, and integral of the motion are presented. Differential corrections and continuation methods are employed to construct periodic orbits and periodic orbit families. Finally, invariant manifolds and Poincaré maps are introduced to set up transfer design.

- **Chapter 3:** Poincaré Maps and Trajectory Design in the CR3BP – The theoretical minimum maneuver is derived as a metric to compare maneuver effectiveness. A transfer targeter is formulated, and planar transfers in the Earth-Moon system leveraging manifolds are introduced. The effects of hyperplane selection on planar transfer options

are investigated as well as the necessary map dimensions for fixed versus changing Jacobi constant transfers. Finally, spatial transfers are discussed along with complexities associated with applying mapping strategies to design them.

- **Chapter 4:** Types of Poincaré Maps and Their Applications – The 9:2 NRHO is analyzed in further detailed and presented as the initial orbit for spatial transfers in this investigation. A method for implementing impulsive maneuvers to create arcs for use in a transfer initial guess is introduced and implemented later in this chapter. The need for higher-dimensional Poincaré maps is established and the implications for fixed and changing Jacobi constant transfers are investigated. Finally, the use of non-state variables for map axes is introduced along with their ability to construct mission constraint informed transfers. Throughout this chapter, various transfers between the 9:2 NRHO and a 3:2 planar resonant orbit as well as between the 9:2 NRHO and an L_2 vertical orbit are designed.

- **Chapter 5:** Concluding Remarks – A summary of this investigation and concluding remarks are presented. Observations for higher-dimensional map applications as well as transfers from the 9:2 NRHO to a 3:2 planar resonant orbit and an L_2 vertical orbit are conveyed. Recommendations for future work are given.

2. BACKGROUND – CIRCULAR RESTRICTED THREE-BODY PROBLEM

The universe consists of countless stars and planets, each with their own gravitational fields, that may or may not influence the motion of other bodies, including spacecraft, due to their location. Interest in an understanding of this general motion lead to the formulation of several dynamical models by which to analyze the gravitational influence and trajectories of bodies in space. Specifically, the development of the Circular Restricted Three-Body Problem provided insight into the Earth-Moon system not possible with the two-body problem. The addition of a third body reveals periodic motion, equilibrium solutions, and more that is not prevalent in lower-fidelity models. Following a discussion of the general n-body problem, this chapter introduces the Circular Restricted Three-Body Problem along with its assumptions, equations of motion, and integral of the motion. This model is then leveraged along with differential corrections schemes and continuation methods to construct periodic orbits and periodic orbit families. Finally, invariant manifolds and Poincaré maps are introduced for use in transfer design in the following chapters.

2.1 The n-body Problem

The n-body problem models the motion of n bodies each under the influence of the remaining $n-1$ bodies. Consider Figure 2.1 that depicts a system of n particles, each with a constant mass. These particles are depicted relative to an inertial reference frame, $(\hat{X}, \hat{Y}, \hat{Z})$, where carets denote unit vectors. Position vectors relative to the origin of this inertial frame are defined as $\bar{r}_{\mathrm{i}}$ where the subscript specifies the particle of interest and the overbar indicates a vector. Additionally, the position vector between two individual particles is denoted $\bar{r}_{\mathrm{i}n}$ where the subscripts indicates the position of particle P_n relative to particle P_{i}. To determine the force on particle P_{i} due to the influence of the other particles, Equation (2.1) results from Newton's second law of motion [9],

$$\bar{f}_{\mathrm{i}} = m_{\mathrm{i}}\bar{r}_{\mathrm{i}}'' = -\tilde{G}\sum_{\substack{\mathrm{j}=1 \\ \mathrm{j}\neq\mathrm{i}}}^{N} \frac{m_{\mathrm{i}}m_{\mathrm{j}}}{r_{\mathrm{ji}}^3}\bar{r}_{\mathrm{ji}} \tag{2.1}$$

In this equation, $\bar{r}_{\mathrm{i}}''$ is the acceleration vector for P_{i} where the primes indicate the derivative with respect to dimensional time and an inertial observer. Further, $\tilde{G}$ is the universal gravitational constant and the distance between any two particles is expressed as $r_{\mathrm{ji}} = |\bar{r}_{\mathrm{i}} - \bar{r}_{\mathrm{j}}|$ where no overbar indicates the magnitude of the vector. Since no integrals of the motion exist, researchers have explored various numerical methods as well as simplified versions of the n-body problem to understand the complex dynamical motion.

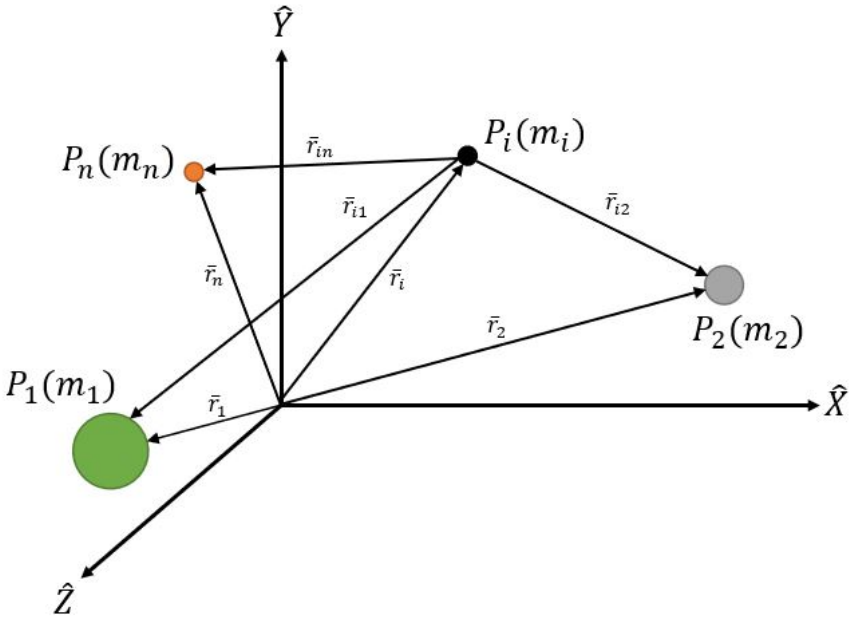

Figure 2.1. Force on particle i in a system of n particles.

2.2 The Circular Restricted Three-Body Problem

In the absence of an analytical solution or any integrals of the motion in the n-body problem, simplifying the model offers insight into the motion. Reducing the number of bodies to two exposes Keplerian motion, and the benefit to a model representing Keplerian orbits is an analytical solution. But, to expand the available solution space and obtain further insight into a system where multiple (i.e., > 2) gravitational bodies are significant to the behavior, the Kepler problem is augmented by the addition of a third gravitational force to reveal dynamical motion that does not exist in the two-body problem. Even the

additional of just one body introduces new types of behavior. Thus, there are now three bodies, P_1, P_2, and P_3 with masses m_1, m_2, and m_3, respectively, that each influence the motion of the other two bodies.

The force equation is revisited to determine the resultant force on P_3 due to the existence of P_1 and P_2. For this system of three bodies, $\bar{r}_{31}$ is defined as the distance from P_3 to P_1 and $\bar{r}_{32}$ is the distance from P_3 to P_2. The magnitudes of these vectors are $r_{13} = r_{31}$ and $r_{23} = r_{32}$, respectively. Applying Equation (2.1) to model the motion of P_3 in a system of three total particles results in

$$\bar{f}_3 = m_3\bar{r}_3'' = -\frac{\tilde{G}m_3m_1}{r_{13}^3}\bar{r}_{13} - \frac{\tilde{G}m_3m_2}{r_{23}^3}\bar{r}_{23} \tag{2.2}$$

This second-order vector equation represents six scalar, first-order nonlinear differential equations. The equations for the force on P_1 and P_2 due to the other two bodies also each represent six scalar, first-order nonlinear differential equations. Thus, there are now eighteen coupled differential equations that would require eighteen constants of integration to obtain an analytical solution. Due to insufficient integrals of the motion, the general three-body problem lacks a complete solution; however, specific assumptions in the three-body problem add a better understanding of the solution space.

2.2.1 Assumptions: CR3BP

Although the general three-body problem does not possess a closed-form solution, some simplifying assumptions enable useful analysis in the problem. Such is particularly true for assumptions that reflect representative physical problems in the solar system. The first of these assumptions is that the mass of the third body is significantly less that the mass of the first and second bodies, i.e., $m_3 << m_1, m_2$. This assumption is reasonable for many examples, e.g., modeling the motion of a spacecraft or small body such as a comet relative to the Sun or planets. Thus, the third body does not influence the motion of the first two bodies. Therefore, the motion of P_1 and P_2 is assumed Keplerian and is modeled as a two-body problem as opposed to P_3 which can move outside the plane of motion of the primaries. Further, it is assumed that P_1 and P_2 have circular orbits about their barycenter. These

assumptions reduce the general three-body problem into the Circular Restricted Three-Body Problem (CR3BP).

2.2.2 Deriving the CR3BP Equations of Motion

Figure 2.2 illustrates a set of coordinate frames and vectors useful in the CR3BP. For this problem, the origin of both the inertial and the rotating reference frame, $(\hat{X}, \hat{Y}, \hat{Z})$ and $(\hat{x}, \hat{y}, \hat{z})$ respectively, are defined at the center of mass, or barycenter B, of P_1 and P_2. Defined as being infinitesimally small, P_3 does not affect the barycenter location. Note also that P_1 is arbitrarily defined as the larger primary. As apparent in Figure 2.2, the rotating reference frame is defined such that the $\hat{x}$-axis is defined from P_1 towards P_2, $\hat{z}$ is out-of-plane and parallel to the angular momentum vector of the primaries, and $\hat{y}$ completes the dextral orthonormal triad. The rotating frame is related to the inertial frame through the angle θ which lies in the plane of motion of the primaries and evolves at a constant rate.

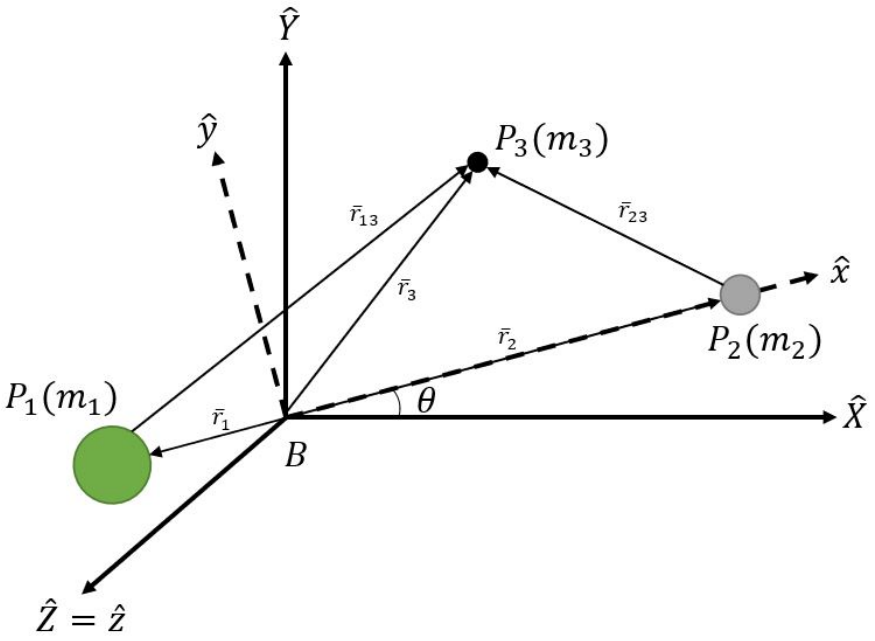

Figure 2.2. Circular Restricted Three-Body Problem diagram.

To derive the equations of motion, revisit the equation for the force on P_3 due to P_1 and P_2. Rewriting Equation (2.2) and dividing by m_3 results in

$$\bar{r}_3'' = -\frac{\tilde{G}m_1}{r_{13}^3}\bar{r}_{13} - \frac{\tilde{G}m_2}{r_{23}^3}\bar{r}_{23} \tag{2.3}$$

Next, the vectors $\bar{r}_{13}$ and $\bar{r}_{23}$ are decomposed into their components in the rotating frame. Let $\bar{r}_3 = \tilde{x}\hat{x} + \tilde{y}\hat{y} + \tilde{z}\hat{z}$ be the coordinates in the rotating reference frame of P_3. Additionally, r_1 is the distance of P_1 from the barycenter and r_2 is the distance of P_2 from the barycenter. Using vector addition, $\bar{r}_{13}$ and $\bar{r}_{23}$ can be written as

$$\bar{r}_{13} = (r_1 + \tilde{x})\hat{x} + \tilde{y}\hat{y} + \tilde{z}\hat{z} \tag{2.4}$$

$$\bar{r}_{23} = (-r_2 + \tilde{x})\hat{x} + \tilde{y}\hat{y} + \tilde{z}\hat{z} \tag{2.5}$$

Their magnitudes are, therefore,

$$r_{13} = \sqrt{(r_1 + \tilde{x})^2 + \tilde{y}^2 + \tilde{z}^2} \tag{2.6}$$

$$r_{23} = \sqrt{(-r_2 + \tilde{x})^2 + \tilde{y}^2 + \tilde{z}^2} \tag{2.7}$$

To express the left side of Equation (2.3) in terms of rotating coordinates as viewed by an inertial observer, the basic kinematic equation is applied twice. First, define $\bar{r}_3' = \frac{{}^I d\bar{r}_3}{dt}$ as the rate of change of $\bar{r}_3$ as seen by an inertial observer, denoted with a superscript I. Then, the prime symbol indicates the derivative with respect to dimensional time. This derivative is related to the derivative as seen by a rotating observer, as denoted with a superscript R, as follows

$$\bar{r}_3' = \frac{{}^I d\bar{r}_3}{dt} = \frac{{}^R d\bar{r}_3}{dt} + {}^I\bar{\omega}^R \times \bar{r}_3 \tag{2.8}$$

where ${}^I\bar{\omega}^R = N\hat{z}$ is the average angular velocity, or mean motion, of the rotating frame with respect to the inertial frame. Note that N is constant due to the circular motion of the primaries. Applying the basic kinematic equation a second time,

$$\bar{r}_3'' = \frac{{}^I d\bar{r}_3'}{dt} = \frac{{}^R d\bar{r}_3'}{dt} + {}^I\bar{\omega}^R \times \bar{r}_3' = \frac{{}^R d^2\bar{r}_3}{dt^2} + 2{}^I\bar{\omega}^R \times \frac{{}^R d\bar{r}_3}{dt} + {}^I\bar{\omega}^R \times {}^I\bar{\omega}^R \times \bar{r}_3 \tag{2.9}$$

Applying Equations (2.8) and (2.9) to $\bar{r}_3$ as written in terms of rotating coordinates yields

$$\bar{r}_3'' = (\tilde{x}'' - 2N\tilde{y}' - N^2\tilde{x})\hat{x} + (\tilde{y}'' + 2N\tilde{x}' - N^2\tilde{y})\hat{y} + \tilde{z}''\hat{z} \tag{2.10}$$

For coordinates expressed in terms of a rotating reference frame, rather than an inertial reference frame, the Coriolis and centripetal accelerations are apparent. Equation (2.9) incorporates the Coriolis and centripetal accelerations in its second and final terms [25], as noted,

$$\bar{a}_{Coriolis} = 2{}^I\bar{\omega}^R \times \frac{{}^R d\bar{r}_3}{dt} = -2N\tilde{y}'\hat{x} + 2N\tilde{x}'\hat{y} \tag{2.11}$$

$$\bar{a}_{centripetal} = {}^I\bar{\omega}^R \times {}^I\bar{\omega}^R \times \bar{r}_3 = -N^2\tilde{x}\hat{x} - N^2\tilde{y}\hat{y} \tag{2.12}$$

Substituting $\bar{r}_3''$ in terms of rotating coordinates as well as the new vector definitions for $\bar{r}_{13}$ and $\bar{r}_{23}$ into Equation (2.3) and separating by components results in the following scalar equations of motion,

$$\tilde{x}'' - 2N\tilde{y}' - N^2\tilde{x} = -\frac{\tilde{G}m_1(r_1 + \tilde{x})}{r_{13}^3} - \frac{\tilde{G}m_2(-r_2 + \tilde{x})}{r_{23}^3} \tag{2.13}$$

$$\tilde{y}'' + 2N\tilde{x}' - N^2\tilde{y} = -\frac{\tilde{G}m_1\tilde{y}}{r_{13}^3} - \frac{\tilde{G}m_2\tilde{y}}{r_{23}^3} \tag{2.14}$$

$$\tilde{z}'' = -\frac{\tilde{G}m_1\tilde{z}}{r_{13}^3} - \frac{\tilde{G}m_2\tilde{z}}{r_{23}^3} \tag{2.15}$$

These are the three scalar, dimensional differential equations for the motion of P_3 under the gravitational influence of two larger masses.

To analyze motion in the general system and introduce quantities more suitable for numerical integration, it is convenient to nondimensionalize the equations of motion using characteristic quantities of length, mass, and time, i.e., ℓ^*, m^*, and t^*. To simplify the problem, the characteristic length ℓ^* is defined as the constant distance between the larger and smaller primaries such that this nondimensionalized distance equals 1. Thus,

$$\ell^* = r_1 + r_2 \tag{2.16}$$

The characteristic length enables the distance between the two larger primaries to be unity since the semi-major axis is nondimensionalized as,

$$a = \frac{\tilde{a}}{\ell^*} = \frac{r_1 + r_2}{r_1 + r_2} = 1 \tag{2.17}$$

The problem is further simplified by selecting the characteristic mass to be

$$m^* = m_1 + m_2 \tag{2.18}$$

Using m^*, let the nondimensionalization of m_2 be defined as

$$\mu = \frac{m_2}{m^*} \tag{2.19}$$

As a result, the characteristic mass is written as

$$m^* = m_1 + m_2 = m_1 + \mu m^* \tag{2.20}$$

Simplifying

$$1 = \frac{m_1}{m^*} + \mu \tag{2.21}$$

Rearranging, it is apparent that the nondimensionalization of m_1 yields

$$\frac{m_1}{m^*} = 1 - \mu \tag{2.22}$$

The nondimensional location of the barycenter along $\hat{x}$ relative to P_1 reveals the physical significance of the nondimensionalized masses, i.e.,

$$r_B = \frac{\sum m r_{\mathrm{i}}}{\sum m} = \frac{\mu(1)}{(1-\mu)+\mu} = \mu \tag{2.23}$$

It is observed from Equation (2.23) that the nondimensional distance between P_1 and the barycenter is μ and, thus, the distance between P_2 and the barycenter is $1 - \mu$.

It is also convenient if the nondimensional gravitational constant is $G = 1$. Then, since the dimensions of the dimensional $\tilde{G}$ are $(\frac{distance^3}{mass*time^2})$, the nondimensional quantity is evaluated as,

$$G = \frac{\tilde{G} m^* (t^*)^2}{(\ell^*)^3} = 1 \tag{2.24}$$

Thus, the characteristic time t^* is deduced from Equation (2.24), i.e.,

$$t^* = \sqrt{\frac{(\ell^*)^3}{\tilde{G} m^*}} \tag{2.25}$$

For this investigation, P_1 is the Earth and P_2 is the Moon, and the corresponding characteristic quantities are summarized in Table 2.1. Characteristic quantities eliminate units from the equations of motion. For clarity, $\bar{r}_{13}$ and $\bar{r}_{23}$ are first nondimensionalized as follows,

$$\bar{d} = \frac{\bar{r}_{13}}{\ell^*} \tag{2.26}$$

$$\bar{r} = \frac{\bar{r}_{23}}{\ell^*} \tag{2.27}$$

Using these nondimensional values, an updated diagram for the CR3BP is illustrated in Figure 2.3. As apparent in this diagram, the vectors $\bar{d}$ and $\bar{r}$ are defined in the rotating frame as

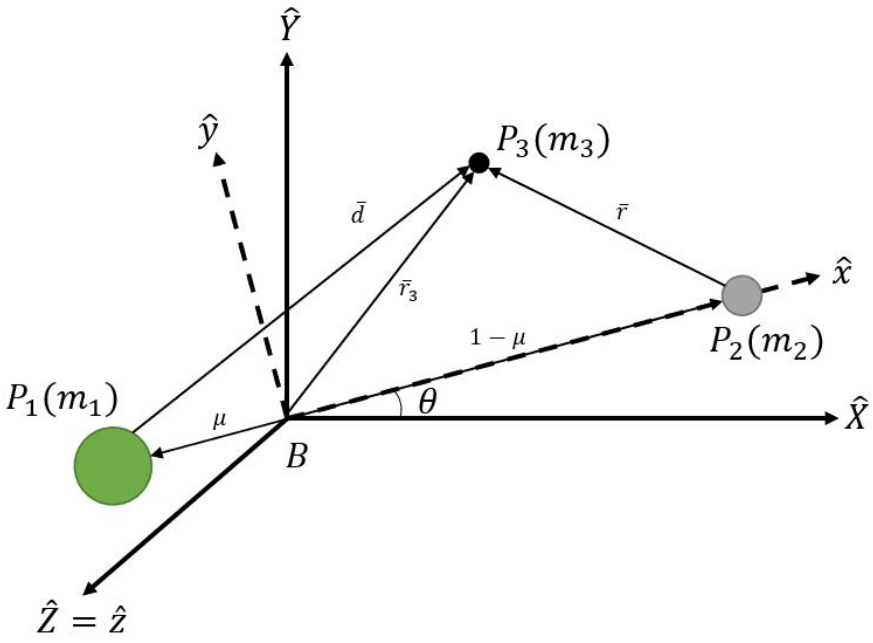

Figure 2.3. Nondimensional CR3BP diagram.

$$\bar{d} = (x+\mu)\hat{x} + y\hat{y} + z\hat{z} \tag{2.28}$$

$$\bar{r} = (x-1+\mu)\hat{x} + y\hat{y} + z\hat{z} \tag{2.29}$$

where $\bar{r}_3 = x\hat{x} + y\hat{y} + z\hat{z}$ are the coordinates of P_3 in nondimensional units, denoted [nd], in the rotating frame. It is also necessary to nondimensionalize the mean motion for use in the equations of motion. Since the dimension of the mean motion is $(\frac{1}{time})$, multiplying by t^* yields,

$$n = Nt^* = \sqrt{\frac{\tilde{G}(m_1+m_2)}{(r_1+r_2)^3}}t^* = \sqrt{\frac{\tilde{G}m^*}{(\ell^*)^3}}\sqrt{\frac{(\ell^*)^3}{\tilde{G}m^*}} = 1 \tag{2.30}$$

It is evident from Equation (2.30) that the angular velocity of the rotating frame with respect to the inertial frame is constant.

Substituting in the new nondimensionalized values for m_1, m_2, G, mean motion, and the position vectors into Equations (2.13), (2.14), and (2.15) results in three scalar, second-order,

Table 2.1. Characteristic quantities for the Earth-Moon system

System	μ	ℓ^* (km)	m^* (kg)	t^* (s)
Earth-Moon	0.0121	384400	6.043e+24	375280.216263673

nondimensional differential equations for the motion of P_3 due to the gravitational influences of P_1 and P_2.

$$\ddot{x} - 2n\dot{y} - n^2 x = -\frac{(1-\mu)(x+\mu)}{d^3} - \frac{\mu(x-1+\mu)}{r^3} \tag{2.31}$$

$$\ddot{y} + 2n\dot{x} - n^2 y = -\frac{(1-\mu)y}{d^3} - \frac{\mu y}{r^3} \tag{2.32}$$

$$\ddot{z} = -\frac{(1-\mu)z}{d^3} - \frac{\mu z}{r^3} \tag{2.33}$$

The dots above the variables represent a derivative with respect to nondimensional time and relative to an inertial observer expressed in rotating frame coordinates. In the above equations, the magnitudes of $\bar{d}$ and $\bar{r}$ are defined as follows

$$d = \sqrt{(x+\mu)^2 + y^2 + z^2} \tag{2.34}$$

$$r = \sqrt{(x-1+\mu)^2 + y^2 + z^2} \tag{2.35}$$

Notice that the equations of motion are autonomous since time does not explicitly appear. Additionally, a pseudo-potential function, U^*, written as

$$U^* = \frac{1-\mu}{d} + \frac{\mu}{r} + \frac{1}{2}n^2(x^2 + y^2) \tag{2.36}$$

allows the equations of motion to be rewritten as

$$\ddot{x} - 2\dot{y} = \frac{\partial U^*}{\partial x} \tag{2.37}$$

$$\ddot{y} + 2\dot{x} = \frac{\partial U^*}{\partial y} \tag{2.38}$$

$$\ddot{z} = \frac{\partial U^*}{\partial z} \tag{2.39}$$

Despite alternate formulations for the equations of motion, there remains three second-order differential equations that require six constants of integration to deliver an analytical solution. Unfortunately, no such solution exists, so other types of analysis are pursued to gain insight into the CR3BP.

2.2.3 Equilibrium Solutions - The Lagrange Points

An equilibrium solution for the CR3BP represents a location relative to the rotating frame where a spacecraft with zero velocity and acceleration remains indefinitely. Such a particular solution in the CR3BP provides intuition when investigating the solution space. Discussed by Joseph Lagrange in 1772, the CR3BP has five equilibrium solutions, called Lagrange points, that are located by setting the gradient of the pseudo-potential equal to zero [28].

$$\frac{\partial U^*}{\partial x} = \frac{\partial U^*}{\partial y} = \frac{\partial U^*}{\partial z} = 0 \tag{2.40}$$

The locations of these five Lagrange points relative to the two primaries are plotted in Figure 2.4. This diagram applies to various systems including the Earth-Moon, Sun-Earth, and Sun-Jupiter systems where P_1 is the larger primary. As shown in Figure 2.4, there are three collinear Lagrange points labeled L_1, L_2, and L_3 and two triangular points labeled L_4 and L_5. In the diagram, γ_1 is the distance from the smaller primary to L_1, γ_2 is the distance from the smaller primary to L_2, and γ_3 is the distance from the larger primary to L_3.

Since position and velocity in the CR3BP is measured with respect to the barycenter, it is also necessary to define the location of the Lagrange points relative to the barycenter. For L_1 let the coordinates be defined as $\bar{r}_{L_1} = x_1\hat{x} + y_1\hat{y} + z_1\hat{z}$, for L_2 the position vector is $\bar{r}_{L_2} = x_2\hat{x} + y_2\hat{y} + z_2\hat{z}$, and so on. Based on the diagram, it is evident that the collinear Lagrange

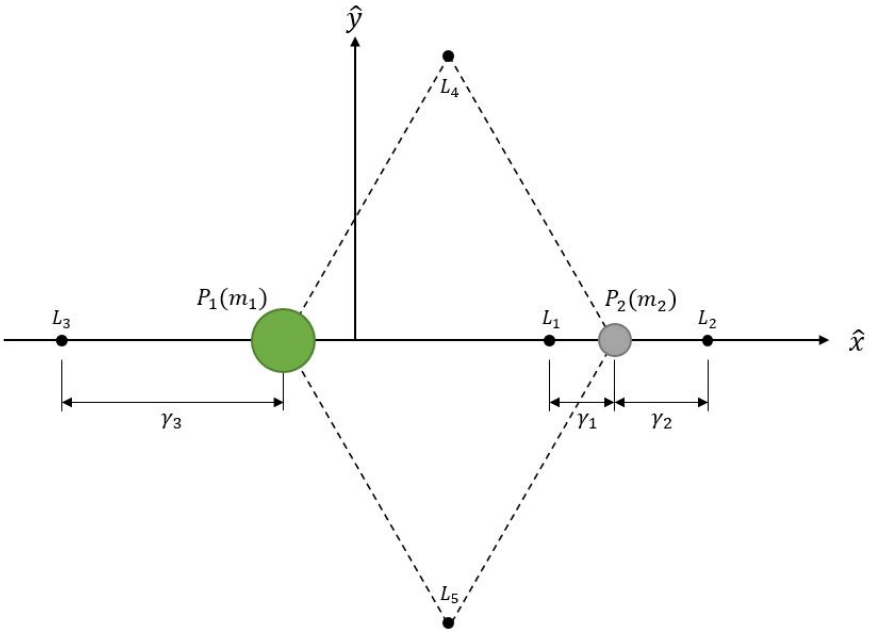

Figure 2.4. Lagrange point locations in the rotating frame.

points have y and z components equal to zero. Further, the x components can be written as follows since it has been previously established that the distance of the smaller primary from the barycenter is $1-\mu$ and the distance of the larger primary from the barycenter is μ.

$$x_1 = 1 - \mu - \gamma_1 \tag{2.41}$$

$$x_2 = 1 - \mu + \gamma_2 \tag{2.42}$$

$$x_3 = -(\mu + \gamma_3) \tag{2.43}$$

Using the nondimensional differential equations of motion and the coordinates of the Lagrange points in terms of γ_i, a Newton-Raphson algorithm allows for the determination of γ_i which are used to calculate numerical values for the positions of the collinear Lagrange points. Table 2.2 lists the results for the collinear equilibrium points in the Earth-Moon

system. To dimensionalize, both γ_i and x_i are multiplied by the ℓ^* corresponding to the Earth-Moon system.

Table 2.2. Collinear Lagrange point locations for the Earth-Moon system.

Lagrange Point	γ_i [nd]	γ_i [km]	x_i [nd]	x_i [km]
L_1	0.1509	$5.8072 * 10^4$	0.8369	$3.2200 * 10^5$
L_2	0.1678	$6.4574 * 10^4$	1.1557	$4.4465 * 10^5$
L_3	0.9929	$3.8202 * 10^5$	-1.0051	$-3.8670 * 10^5$

Unlike the collinear equilibrium points, L_4 and L_5 form equilateral triangles with the two primaries in the plane of motion of P_2 about P_1. This further implies that $x_4 = x_5$, $y_5 = -y_4$, and $z_4 = z_5 = 0$. Using geometry, L_4 and L_5 are located at

$$x_{4,5} = \frac{1}{2} - \mu \tag{2.44}$$

$$y_{4,5} = \pm\frac{\sqrt{3}}{2} \tag{2.45}$$

where μ is the mass parameter for the system of interest. Table 2.3 contains the locations of the triangular Lagrange points in the Earth-Moon system.

Table 2.3. Triangular Lagrange point locations for the Earth-Moon system.

Lagrange Point	x_i [nd]	x_i [km]	y_i [nd]	y_i [km]
L_4	0.4878	$1.8770 * 10^5$	0.8660	$3.3320 * 10^5$
L_5	0.4878	$1.8770 * 10^5$	-0.8660	$-3.3320 * 10^5$

2.2.4 Integral of the Motion - Jacobi Constant

Recall the pseudo-potential function in Equation (2.36). As the pseudo-potential is a function of only position states, the system is assumed conservative, and, thus, an energy

adjacent integral of the motion is found to exist. To do this, consider an arbitrary velocity vector in the rotating frame.

$$^{R}\bar{v} = \dot{x}\hat{x} + \dot{y}\hat{y} + \dot{z}\hat{z} \tag{2.46}$$

Taking the dot product of Equation (2.46) with each of the three equations of motion written in terms of the pseudo-potential (Equations (2.37)-(2.39)) and adding the resulting three scalar equations together results in

$$\dot{x}\ddot{x} + \dot{y}\ddot{y} + \dot{z}\ddot{z} = \frac{dU^*}{dt} \tag{2.47}$$

Integrating gives

$$\dot{x}^2 + \dot{y}^2 + \dot{z}^2 = 2U^* - C \tag{2.48}$$

where the integration constant C has been defined as negative for convenience. Rearranging reveals

$$C = 2U^* - v^2 \tag{2.49}$$

or

$$C = (x^2 + y^2) + \frac{2(1-\mu)}{d} + \frac{2\mu}{r} - v^2 \tag{2.50}$$

where d and r are defined as in Equations (2.34) and (2.35). Equations (2.49) and (2.50) are equivalent formulas to calculate the only constant of integration for the CR3BP – the Jacobi constant.

2.2.5 Zero Velocity Surfaces

The existence of the Jacobi constant leads directly to the existence of surfaces that constitute the bounds of motion on P_3, allowing for an immediate understanding of the available solution space given values for C and μ. These bounding surfaces are calculated by

setting the velocity, v, to zero in Equation (2.50). Thus, the formula for these Zero Velocity Surfaces (ZVSs) is

$$C = (x^2 + y^2) + \frac{2(1-\mu)}{d} + \frac{2\mu}{r} \tag{2.51}$$

From this equation it is known that a spacecraft with a Jacobi constant value of C and a position that falls on a ZVS must have zero velocity.

Slicing a ZVS where it intersects the $\hat{x}$-$\hat{y}$ plane results in a Zero Velocity Curve (ZVC). Examining motion confined to this plane reveals dynamical insights for a system, so, frequently, only the portion of the ZVSs that lie in the $\hat{x}$-$\hat{y}$ plane is considered. To examine these ZVCs, first consider that a ZVC corresponding to the Jacobi constant value of a Lagrange point must pass through that Lagrange point since equilibrium points possess no velocity. To find the C values corresponding to the collinear Lagrange points, the position of each point is used in Equation (2.51). It is know that the y and z components of L_1, L_2, and L_3 are equal to zero, so the Jacobi constant values for these points are calculated using

$$C_{L_\mathrm{i}} = x_\mathrm{i}^2 + \frac{2(1-\mu)}{[(x_\mathrm{i}+\mu)^2]^{1/2}} + \frac{2\mu}{[(x_\mathrm{i}-1+\mu)^2]^{1/2}} \tag{2.52}$$

The Jacobi constant values for the collinear Lagrange points in the Earth-Moon system are as follows in Table 2.4.

Table 2.4. Jacobi constant values for the collinear Lagrange points in the Earth-Moon system.

System	C_{L_1}	C_{L_2}	C_{L_3}
Earth-Moon	3.1883	3.1722	3.0121

To illustrate the general geometry of the ZVCs over a range of C, Figure 2.5 has been provided where each ZVC has been labeled with its corresponding Jacobi constant value. Note that a Jacobi constant value that does not result in a ZVC does not mean that a ZVS does not exist. The surface simply does not intersect the $\hat{x}$-$\hat{y}$ plane. While ZVCs offer insight into where a spacecraft can or cannot go at certain energy levels, they does not offer any

information on what these paths might look like, how to reach a desired location, or what periodic motion is possible. Calculating this motion requires numerical methods as well as an understanding of stability.

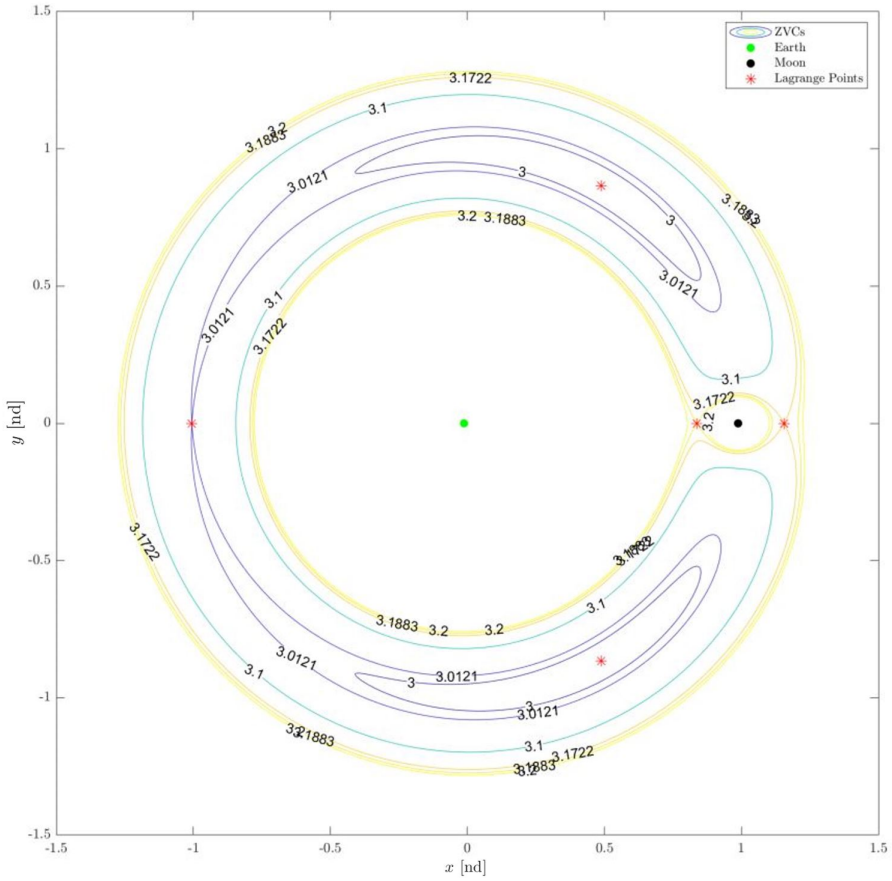

Figure 2.5. Zero velocity curves for various Jacobi constant values in the Earth-Moon rotating frame.

2.3 Differential Corrections

The six first-order differential equations of motion for the CR3BP are obtained from the three second-order differential equations. These six equations of motion are written in a state-space representation as

$$\dot{\bar{x}} = \bar{f}(\bar{x}, t) \tag{2.53}$$

where

$$\bar{x}(t) = [x(t)\ y(t)\ z(t)\ \dot{x}(t)\ \dot{y}(t)\ \dot{z}(t)]^T \tag{2.54}$$

is the six-dimensional state vector. Numerically integrating this equation given initial conditions provides position and velocity states over time, but it does not provide any indication about what trajectory or orbit is actually desired or how to achieve it.

2.3.1 State Transition Matrix

If it is assumed that numerical integration results in a trajectory, $\bar{x}$, that is nearby some desired trajectory, $\bar{x}^d$, comparing the states on the calculated trajectory and the desired trajectory at some time t results in Figure 2.6. This isochronous variation in states is labeled $\delta\bar{x}(t)$. It is clear from Figure 2.6 that the state on the calculated trajectory at time t is defined as $\bar{x}(t) = \bar{x}^d(t) + \delta\bar{x}(t)$. Taking the derivative of this results in

$$\dot{\bar{x}} = \dot{\bar{x}}^d + \delta\dot{\bar{x}} = \bar{f}(\bar{x}^d + \delta\bar{x}, t) \tag{2.55}$$

Using a Taylor series expansion and neglecting higher order terms yields

$$\dot{\bar{x}} \approx \bar{f}(\bar{x}^d, t) + \frac{\partial \bar{f}}{\partial \bar{x}}|_{\bar{x}^d}\delta\bar{x} \tag{2.56}$$

Knowing that $\dot{\bar{x}} = \dot{\bar{x}}^d + \delta\dot{\bar{x}}$ and $\bar{f}(\bar{x}^d, t) = \dot{\bar{x}}^d$, $\dot{\bar{x}}^d$ is canceled out.

$$\delta\dot{\bar{x}} \approx \frac{\partial \bar{f}}{\partial \bar{x}}|_{\bar{x}^d}\delta\bar{x} = A(t)\delta\bar{x} \tag{2.57}$$

In Equation (2.57), A(t) relates the variation of the derivative of the state to the variation of the state, and, as $A(t) = \frac{\partial \bar{f}}{\partial \bar{x}}|_{\bar{x}^d}$, expanding this out reveals

$$A(t) = \begin{bmatrix} 0 & I_3 \\ \frac{\partial \dot{\bar{v}}(t)}{\partial \bar{\rho}(t)} & \Omega \end{bmatrix} \tag{2.58}$$

where $\bar{\rho}(t)$ and $\bar{v}(t)$ are position and velocity vectors, respectively, which together make up the state vector, i.e., $\bar{x}(t) = [\bar{\rho}(t)\ \bar{v}(t)]$. Additionally, I_3 is the 3×3 identity matrix and Ω is defined as

$$\Omega = \begin{bmatrix} 0 & 2 & 0 \\ -2 & 0 & 0 \\ 0 & 0 & 0 \end{bmatrix} \tag{2.59}$$

Further, since the relationship between $\delta\dot{\bar{x}}$ and $\delta\bar{x}$ is linear, a linear combination of solutions is a solution. Therefore, a general solution to Equation (2.57) is written in matrix form as

$$\delta\bar{x}(t) = \Phi(t, t_0)\delta\bar{x}(t_0) \tag{2.60}$$

where $\Phi(t_0, t_0)$ is the identity matrix. Note that $\Phi(t, t_0)$ is a square matrix that, due to the relationship developed in Equation (2.57), satisfies

$$\dot{\Phi}(t, t_0) = A(t)\Phi(t, t_0) \tag{2.61}$$

The matrix $\Phi(t, t_0)$ is known as the state transition matrix (STM) and relates the state at an initial time to the state after some time t. From Equation 2.60, it is apparent that the STM is the derivative of the state at time t with respect to the state at the initial time t_0.

$$\Phi(t, t_0) = \frac{\partial\bar{x}(t)}{\partial\bar{x}(t_0)} \tag{2.62}$$

Numerically integrating the six first-order differential equations of motion along with Equation (2.61) provides position and velocity states over time along with information on how the final state varies with respect to variation in the initial state. This additional information is used to determine the necessary change in initial conditions in order for the calculated trajectory to match the desired trajectory.

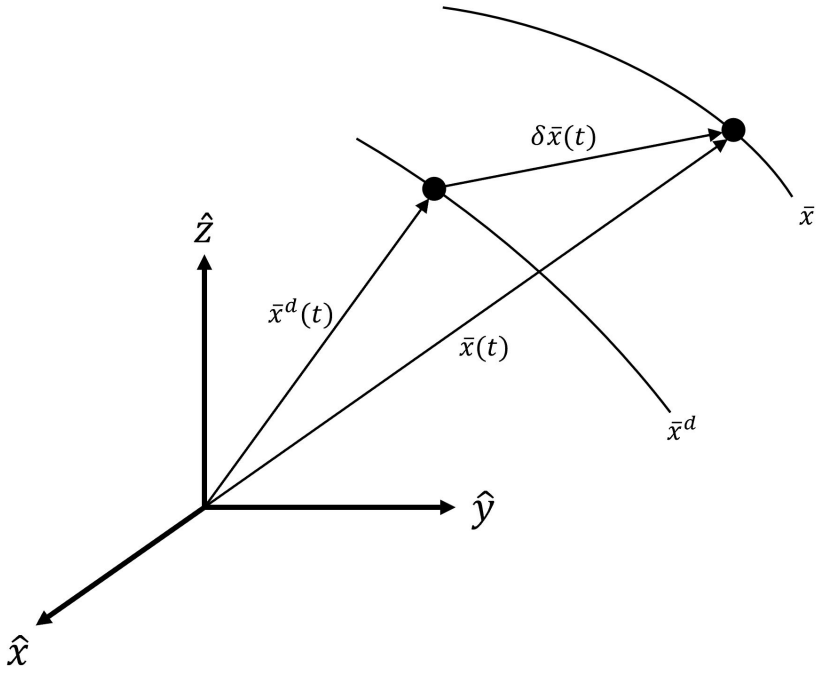

Figure 2.6. Desired trajectory, $\bar{x}^d$, and actual trajectory, $\bar{x}$, at time t.

2.3.2 Single Shooting

Using the equations of motion and STM, it is now possible to determine the change in the initial conditions of P_3 required to reach a specified position or velocity target. Assume, as in Figure 2.7, that an initial state, $\bar{x}_0$, is propagated for a time, t, to create an initial guess for a desired trajectory. Clearly, the initial position, velocity, or both must change for the resultant trajectory to reach the target final state, $\bar{x}_t^d$. Constraints on the problem, such as a need to depart at a certain location, dictate which initial states are able to change to reach the solution. Depending on the problem, it is also possible to allow certain final states to vary. For example, if only the final position is of interest, the final velocity may be any value. A variable with no required value is termed a free variable.

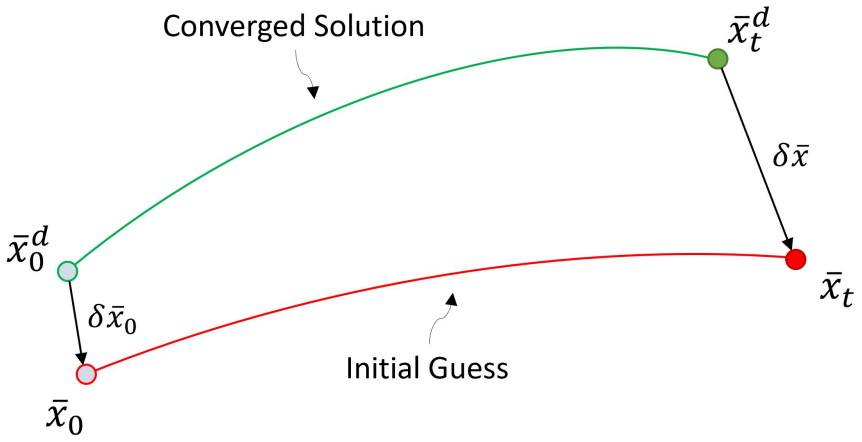

Figure 2.7. Single Shooting Algorithm Diagram.

To create a mathematical formulation for this problem, a design vector $\bar{X}$ is constructed from the n free variables in the problem.

$$\bar{X} = \begin{bmatrix} X_1 \\ X_2 \\ \vdots \\ X_n \end{bmatrix} \tag{2.63}$$

The variables that are not allowed to change, including the targeted variables, are combined into the constraint vector. These m constraints are formulated such that when each constraint is satisfied the vector equals zero.

$$\bar{F}(\bar{X}) = \begin{bmatrix} F_1(\bar{X}) \\ F_2(\bar{X}) \\ \vdots \\ F_m(\bar{X}) \end{bmatrix} = \bar{0} \tag{2.64}$$

To satisfy the constraints, and thus converge on a solution, the free variables are modified until a design vector $\bar{X}^C$ is found such that $\bar{F}(\bar{X}^C) = \bar{0}$. The magnitude of the constraint

vector after the last iteration must be within a specified tolerance to obtain a converged solution. The Taylor-series expansion for $\bar{F}(\bar{X})$ is written as

$$\bar{F}(\bar{X}) \approx \bar{F}(\bar{X}^{\mathrm{j}}) + D\bar{F}(\bar{X}^{\mathrm{j}}) \cdot (\bar{X}^{\mathrm{j}+1} - \bar{X}^{\mathrm{j}}) = \bar{0} \tag{2.65}$$

where j represents the iteration number since generally a numerical update method is required. To relate the design and constraint vectors, the $m \times n$ Jacobian matrix of $\bar{F}$ is calculated.

$$D\bar{F}(\bar{X}^{\mathrm{j}}) = \frac{\partial \bar{F}}{\partial \bar{X}} = \begin{bmatrix} \frac{\partial F_1}{\partial X_1} & \frac{\partial F_1}{\partial X_2} & \cdots & \frac{\partial F_1}{\partial X_n} \\ \frac{\partial F_2}{\partial X_1} & \frac{\partial F_2}{\partial X_2} & \cdots & \frac{\partial F_2}{\partial X_n} \\ \vdots & \vdots & \ddots & \\ \frac{\partial F_m}{\partial X_1} & \frac{\partial F_m}{\partial X_2} & & \frac{\partial F_m}{\partial X_n} \end{bmatrix} \tag{2.66}$$

This Jacobian matrix is recalculated at every iteration for use in an update equation.

There are three different methods to calculate $\bar{X}^C$ depending on the values of n and m. If $n = m$, then $D\bar{F}(\bar{X}^{\mathrm{j}})$ is square and, thus, invertible. This common update equation is

$$\bar{X}^{\mathrm{j}+1} = \bar{X}^{\mathrm{j}} - D\bar{F}(\bar{X}^{\mathrm{j}})^{-1}\bar{F}(\bar{X}^{\mathrm{j}}) \tag{2.67}$$

If $n > m$ then an excess of design variables results in infinite possible solutions. To select a solution that is most similar to the initial guess, a minimum-norm solution is used on the underdetermined system.

$$\bar{X}^{\mathrm{j}+1} = \bar{X}^{\mathrm{j}} - D\bar{F}(\bar{X}^{\mathrm{j}})^T \left[D\bar{F}(\bar{X}^{\mathrm{j}}) \cdot D\bar{F}(\bar{X}^{\mathrm{j}})^T\right]^{-1} \bar{F}(\bar{X}^{\mathrm{j}}) \tag{2.68}$$

Finally, if $n < m$ the system is overdetermined and there is no solution. However, the least squares method may be used as an update equation [29].

$$\bar{X}^{\mathrm{j}+1} = \bar{X}^{\mathrm{j}} - \left[D\bar{F}(\bar{X}^{\mathrm{j}})^T \cdot D\bar{F}(\bar{X}^{\mathrm{j}})\right]^{-1} D\bar{F}(\bar{X}^{\mathrm{j}})^T \bar{F}(\bar{X}^{\mathrm{j}}) \tag{2.69}$$

Depending on the formulation of the problem and, therefore, the number of design variables and constraints, one of these three update equations is utilized.

Periodic Orbit Computation

When locating and constructing symmetric, periodic orbits in the CR3BP, it is efficient to utilize the Mirror Theorem. Introduced in 1955 by Roy and Ovenden, the Mirror Theorem states that if a body has a velocity vector perpendicular to its radial vector at two points then a periodic orbit exists [30]. Extrapolating this concept further, the CR3BP possesses symmetry about the $\hat{x}$-$\hat{z}$ plane for perpendicular crossings of this plane. Therefore, if it is desired to create a consistently repeating trajectory, it is sufficient to locate a trajectory with two perpendicular crossings of the $\hat{x}$-axis. To find such a periodic solution, assume an initial point is selected to be on the $\hat{x}$-axis with a negative y-velocity. To start and end on the axis, $y_0 = y_f = 0$ where a subscript 0 indicates initial time and a subscript f indicates final time. To leave and arrive perpendicularly, it is required that $\dot{x}_0 = \dot{x}_f = 0$. For simplicity, the motion is restricted to be planar, i.e., $z = \dot{z} = 0$, and, thus, only the in-plane components need to be considered.

To locate the desired curve from an initial guess, a single shooting algorithm is used where only the initial y-velocity and time-of-flight are allowed to vary. Therefore, the design vector is

$$\bar{X} = \begin{bmatrix} \dot{y}_0 \\ t \end{bmatrix} \tag{2.70}$$

and the requirements on the final state result in the following constraint vector.

$$\bar{F}(\bar{X}) = \begin{bmatrix} y_f \\ \dot{x}_f \end{bmatrix} = \bar{0} \tag{2.71}$$

Figure 2.8 demonstrates the iterative process that takes place using a single shooting algorithm to arrived at the solid converged trajectory. The equations of motion and the STM at the initial perpendicular crossing are numerically integrated until the trajectory reaches the next $\hat{x}$-axis crossing. If the crossing is not exactly perpendicular, the design variables are updated and the trajectory is re-propagated. This process is repeated until the constraint vector equals zero, indicating a perpendicular crossing. The converged solution that departs

and arrives at the $\hat{x}$-axis perpendicularly is then mirrored across the $\hat{x}$-$\hat{z}$ plane to obtain a complete periodic orbit. A specific example of a planar periodic orbit constructed in this manner is an L_1 Lyapanov as illustrated in Figure 2.9. Being a Lyapunov orbit, it encircles a Lagrange point, and, as discussed, the converged trajectory possessing two perpendicular crossings is mirrored across the $\hat{x}$-axis to provide the full Lyapunov orbit in solid black.

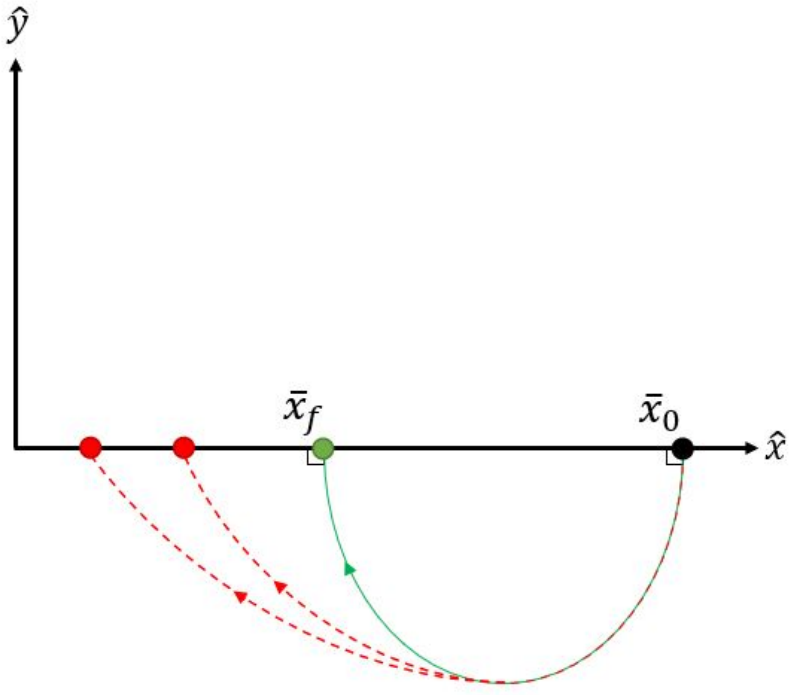

Figure 2.8. Single shooting to locate a periodic orbit.

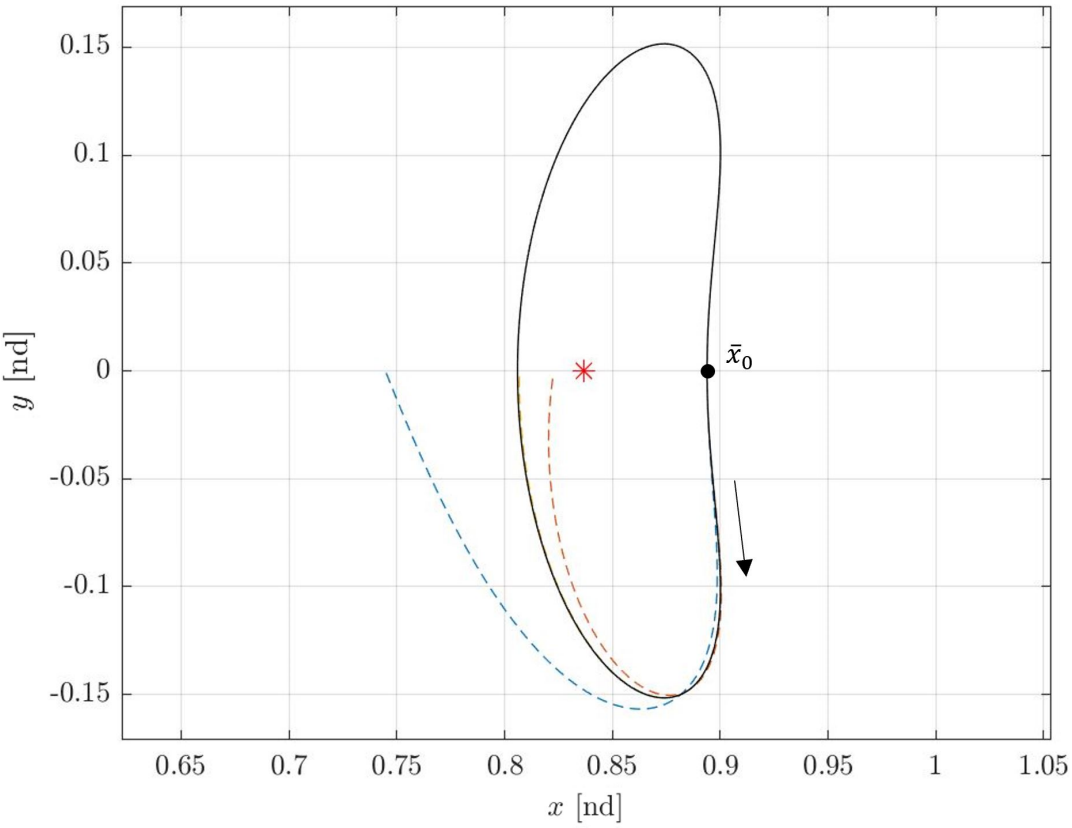

Figure 2.9. Targeting an L_1 Lyapunov orbit.

2.3.3 Multiple Shooting

Recall that the STM is derived using a linear approximation; however, the equations of motion describe a nonlinear system. Therefore, the longer the propagation time, the less accurate the approximation. But what if a desired trajectory has a long time-of-flight? It is practical to split a long trajectory into smaller segments and simultaneously target them for position and velocity continuity. This process, illustrated in Figure 2.10, essentially performs several single shooting algorithms simultaneously and is known as a multiple shooting algorithm.

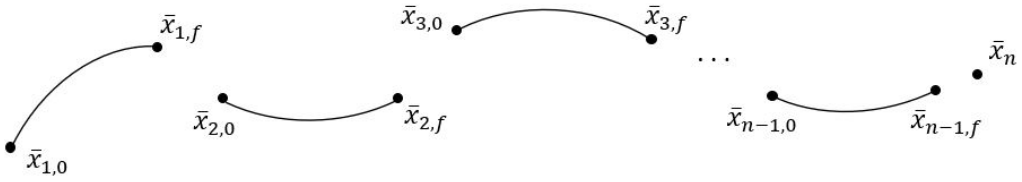

Figure 2.10. Multiple shooting algorithm diagram.

Assume that an initial guess for a trajectory is discretized into n patch points. These points are compiled to form the design vector as they are permitted to vary to locate a continuous, converged trajectory.

$$\bar{X} = \begin{bmatrix} \bar{x}_1 \\ \bar{x}_2 \\ \vdots \\ \bar{x}_{n-1} \\ \bar{x}_n \end{bmatrix} \tag{2.72}$$

Let the first $n-1$ points be propagated for a time t from their initial state, $\bar{x}_{\mathrm{i},0}$, to a final state, $\bar{x}_{\mathrm{i},f}$. To find a converged, continuous trajectory it is necessary that $\bar{x}_{\mathrm{i},f} = \bar{x}_{\mathrm{i}+1,0}$. Thus, the end of each segment is continuous in position and velocity with the beginning of the next segment. Rearranging these expressions so they equal zero, the constraint vector is formulated as

$$\bar{F}(\bar{X}) = \begin{bmatrix} \bar{x}_{1,f} - \bar{x}_{2,0} \\ \bar{x}_{2,f} - \bar{x}_{3,0} \\ \vdots \\ \bar{x}_{n-1,f} - \bar{x}_n \end{bmatrix} = \bar{0} \tag{2.73}$$

The $D\bar{F}(\bar{X})$ matrix for this multiple shooting algorithm has dimensions $6(n-1) \times 6n$ and is of the form

$$D\bar{F}(\bar{X}) = \begin{bmatrix} \frac{\partial \bar{x}_{1,f}}{\partial \bar{x}_{1,0}} & -I_6 & & & & 0 \\ & \frac{\partial \bar{x}_{2,f}}{\partial \bar{x}_{2,0}} & -I_6 & & & \\ & & \frac{\partial \bar{x}_{2,f}}{\partial \bar{x}_{2,0}} & -I_6 & & \\ & & & \ddots & \ddots & \\ 0 & & & & \frac{\partial \bar{x}_{n-1,f}}{\partial \bar{x}_n} & -I_6 \end{bmatrix} \tag{2.74}$$

where I_6 is the 6×6 identity matrix. The matrix has two clear diagonals with the rest of the values as zero. Recognizing the form of the partial derivatives, the $D\bar{F}(\bar{X})$ matrix can also be written as

$$D\bar{F}(\bar{X}) = \begin{bmatrix} \Phi_1 & -I_6 & & & & 0 \\ & \Phi_2 & -I_6 & & & \\ & & \Phi_3 & -I_6 & & \\ & & & \ddots & \ddots & \\ 0 & & & & \Phi_{n-1} & -I_6 \end{bmatrix} \tag{2.75}$$

Adding or removing design variables and constraints effects the exact formulation of $D\bar{F}(\bar{X})$. For example, if time along each arc is a design variable, then the partials with respect to the time of each arc also need to be calculated.

Periodic Orbit Computation

Unlike a single shooting targeter, multiple shooting does not frequently leverage the symmetric properties of the CR3BP. An initial guess for a full periodic orbit is broken into pieces by a chosen number of patch points. This process creates orbit segments which are individually propagated for use in a multiple shooting algorithm. Position and velocity continuity at all points ensures a smooth orbit, and, for periodic orbits, the final arc is constrained to end at the initial patch point. Because this multiple shooting setup creates a singular orbit, the position and velocity constraints ensure that the Jacobi constant value of

the entire orbit is fixed. This implicit constraint often results in an overconstrained system that is rectified by removing a single constraint that has a value not likely to change signs at the chosen patch point or by implementing a method to invert the singular STM.

Of great interest to current exploration missions is the 9:2 lunar synodic resonant near rectilinear halo orbit (NRHO). While considered a relatively stable orbit, orbits in the NRHO region of the halo family as defined by Zimovan, Howell, and Davis present convergence challenges due to their proximity to the Moon [31]. As a result, it may be beneficial to utilize a multiple shooting targeter. Figure 2.11(a) illustrates the 9:2 NRHO broken into segments which are propagated individually for use in a multiple shooter to obtain the converged result in Figure 2.11(b).

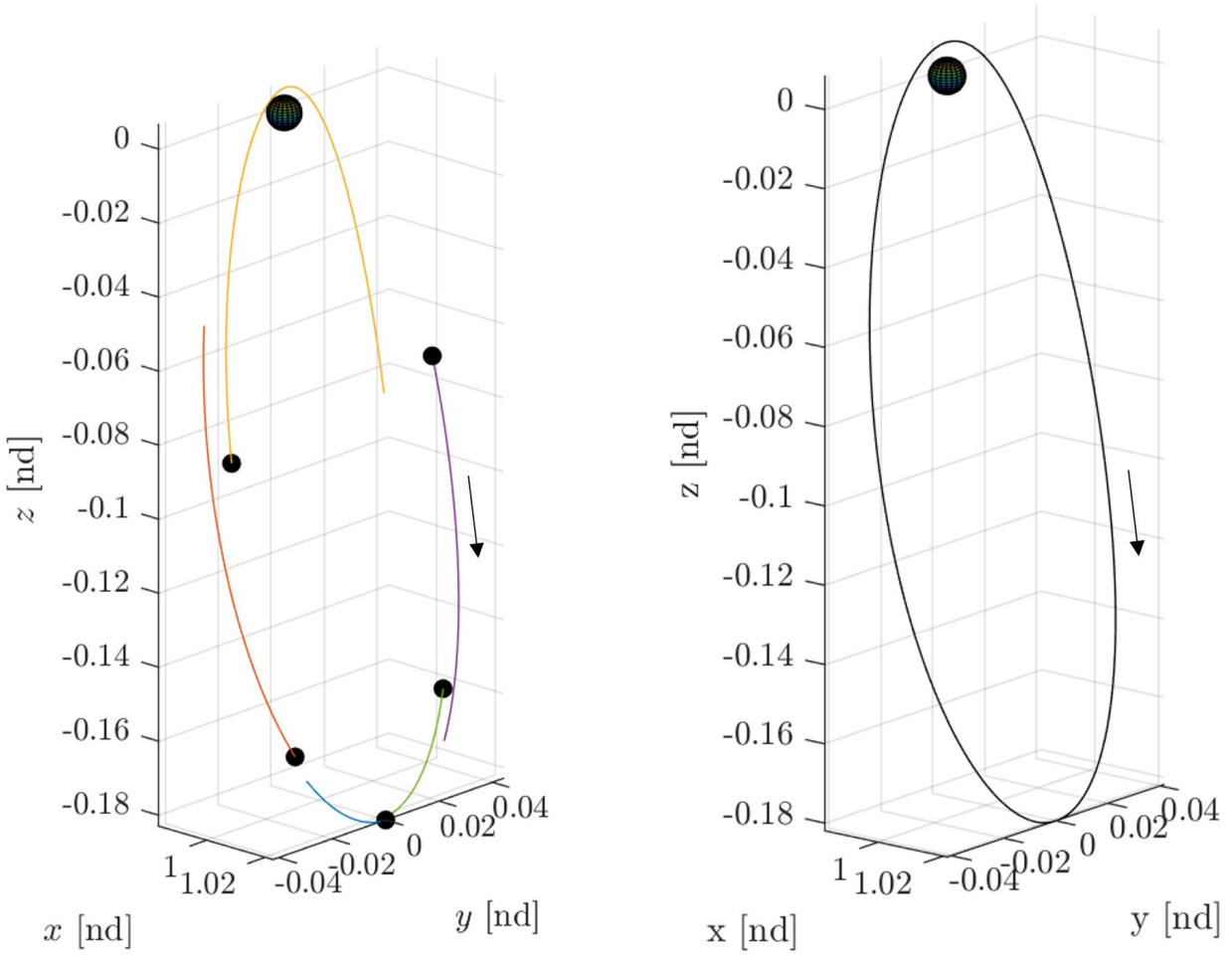

(a) Initial guess for 9:2 synodic NRHO.

(b) Converged 9:2 synodic NRHO.

Figure 2.11. Multiple shooting algorithm application.

2.4 Continuation Methods

Periodic orbits frequently occur in families that evolve smoothly and posses similar geometries. Periodic orbit families provide an understanding of the available flow in the design space and present numerous options for departure, arrival, and intermediate segments for transfers. Additionally, these families, often centered around a Lagrange point or primary, enable the informed selection of desired characteristics. For example, if a particular geometry is preferred for a transfer, an orbit is selected from a family with said geometry. To reduce the ΔV required to overcome any change in energy, this orbit is often chosen to possess a similar Jacobi constant value to other segments of the transfer. A combination of differential corrections and a continuation method are required to calculate periodic orbit families. While many continuation methodologies exist, two main techniques are utilized in this investigation.

2.4.1 Natural Parameter Continuation

Natural parameter continuation is used to locate other family members of a given orbit by stepping along a chosen parameter such as a state variable, period, or Jacobi constant. Once this parameter is increased or decreased, the remaining initial conditions are either taken from the previous converged solution or are extrapolated from the previous solutions. After an initial guess is obtained, either a single shooter or multiple shooter is used to converge on the new family member.

Choice of parameter step size is an important consideration for natural parameter continuation to compute the entire family. A step size that is too large risks that the targeter will fail to converge or jump to a solution outside of the family. While still a valid solution in the CR3BP, such a converged orbit is not within the desired family. Contrarily, a step size that is too small locates an orbit within the family, but the computation time necessary to solve for the entire family is much higher. An adaptive step size is often a suitable resolution to this problem.

Periodic Orbit Family Computation

Recall the L_1 Lyapunov orbit computed with a single shooting algorithm in Figure 2.9. To locate another periodic orbit nearby with a similar geometry, the initial state from the converged orbit is shifted slightly to the right along the $\hat{x}$-axis and all other state variables are kept the same. Recall that this initial state is the perpendicular crossing to the right of L_1. The initial conditions are then propagated until the $\hat{x}$-axis is crossed, and this resulting trajectory is used as an initial guess in a single shooting algorithm to determine the $\dot{y}_0$ necessary to converge on a periodic orbit. This process of incrementing the chosen parameter and targeting is repeated until the targeter fails to converge at the given tolerance. Figure 2.12 shows the L_1 Lyapunov family that is obtained through natural parameter continuation. Each orbit is colored according to its respective Jacobi constant value and the Earth and Moon are plotted to scale. While natural parameter continuation is described as the process of incrementing a continuation parameter and using the previous state for the initial guess, once several orbits have been obtained, extrapolation frequently provides a better guess for the initial state variables. A better initial guess tends to reduce the number of iterations and improves the probability of convergence.

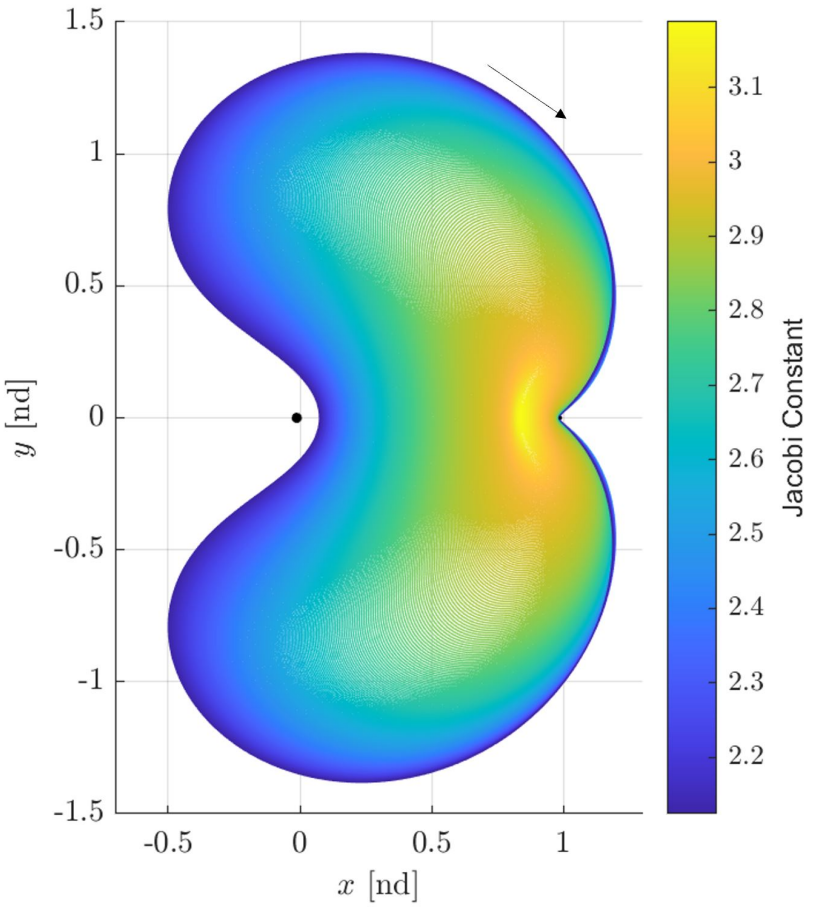

Figure 2.12. L_1 Lyapunov family in the Earth-Moon system colored by Jacobi constant value.

2.4.2 Pseudo-Arclength Continuation

Natural parameter continuation steps along a single variable and repeatedly updates the initial conditions to locate the next family member. Clearly, this benefits from a parameter that evolves linearly along the family with no major jumps or turns. Cusps in a parameter make it advantageous to use a continuation method that is impervious to such changes. Pseudo-arclength continuation steps along the null space of $D\bar{F}(\bar{X})$ and, thus, is not affected by variations in individual variables. This method is possible since adding a multiple of the null space does not affect the linear solution. First let

$$\Delta\bar{X}^{\mathrm{j}} = null(D\bar{F}(\bar{X}^{\mathrm{j}})) \tag{2.76}$$

To step along the null space and obtain the initial guess for the next family member,

$$\bar{X}^{\mathrm{j}+1} = \bar{X}^{\mathrm{j}} + \Delta s \Delta \bar{X}^{\mathrm{j}} \tag{2.77}$$

is used where Δs is the step size. To enforce the new solution to occur at this step along the null space, the following pseudo-arclength constraint is needed.

$$(\bar{X}^{\mathrm{j}+1} - \bar{X}^{\mathrm{j}})^T \Delta \bar{X}^{\mathrm{j}} - \Delta s = 0 \tag{2.78}$$

This constraint results in an augmented constraint vector

$$\bar{G}(\bar{X}^{\mathrm{j}+1}) = \begin{bmatrix} \bar{F}(\bar{X}^{\mathrm{j}+1}) \\ (\bar{X}^{\mathrm{j}+1} - \bar{X}^{\mathrm{j}})^T \Delta \bar{X}^{\mathrm{j}} - \Delta s \end{bmatrix} = \bar{0} \tag{2.79}$$

as well as an augmented Jacobian matrix.

$$D\bar{G}(\bar{X}^{\mathrm{j}+1}) = \begin{bmatrix} D\bar{F}(\bar{X}^{\mathrm{j}+1}) \\ \Delta \bar{X}^{\mathrm{j}^T} \end{bmatrix} \tag{2.80}$$

Finally, the augmented constraint vector and Jacobian matrix are utilized in an appropriate iterative update method.

Periodic Orbit Family Computation

The L_2 southern halo family is an example of a family with a parameter that does not evolve linearly. If natural parameter is initially used to step along z, it is eventually necessary to switch directions to compute the entire family. The initial z-position, z_0, versus Jacobi constant is illustrated for a subset of the family in Figure 2.13. Since Jacobi constant value evolves smoothly along families, clearly there is a sharp reversal in the trend of z_0 along the L_2 southern halo family. With pseudo-arclength continuation, the need to switch step directions or parameters is avoided entirely. Pseudo-arclength also benefits from a larger step size because all states are adjusted simultaneously to create a generally more accurate initial guess. The L_2 southern halo family obtained with pseudo-arclength continuation is

illustrated in Figure 2.14, and each family member is colored according to its Jacobi constant value.

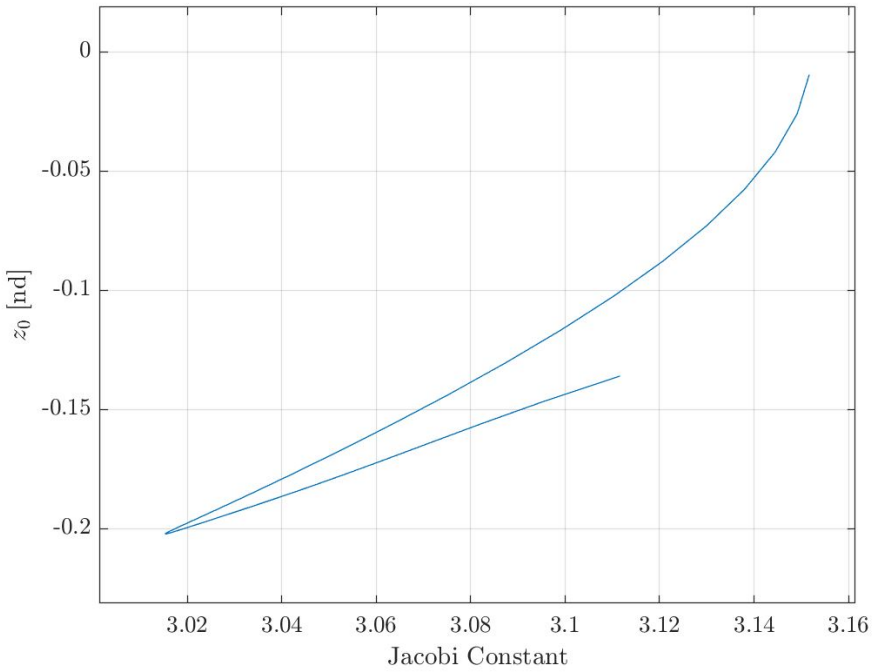

Figure 2.13. Initial z-position compared to Jacobi constant for the Earth-Moon L_2 southern halo family.

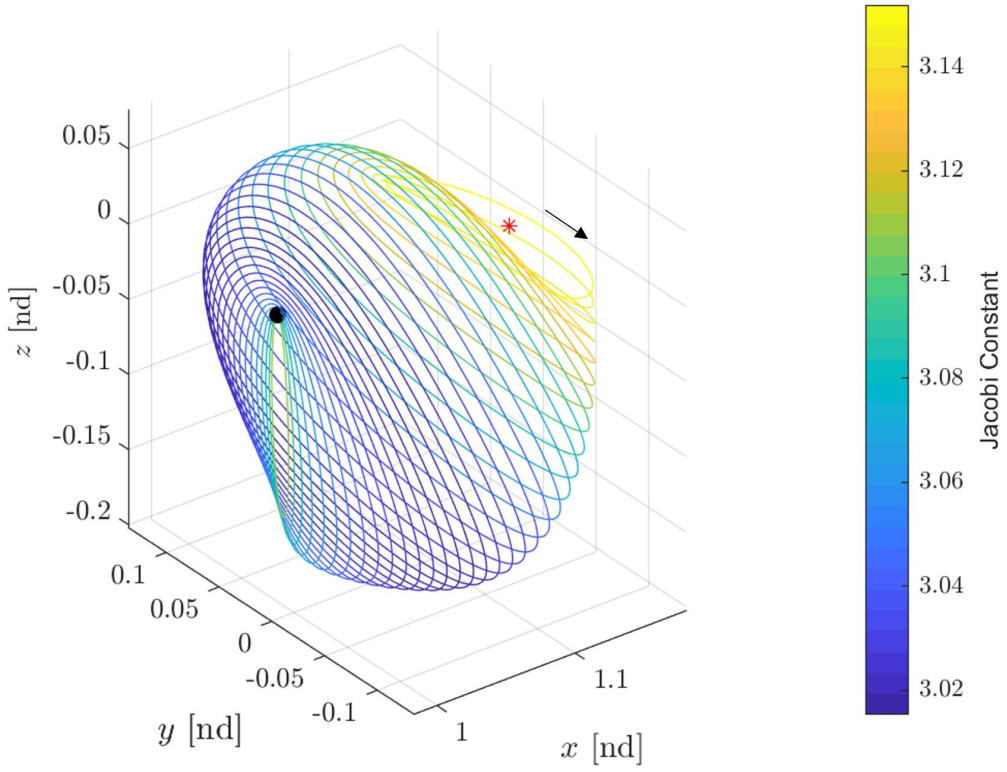

Figure 2.14. L_2 southern halo family in the Earth-Moon system colored by Jacobi constant value.

2.5 Periodic Orbit Families

An abundance of information is obtained through evaluation of periodic orbit families. In addition to the orbits themselves providing transfer options and insight into the dynamical motion of the system, stability properties and, thus, an understanding of long-term behavior is obtained. Changes in stability properties across a family are also often indicative of additional families that intersect the given family. This concept leads to a web of interconnected families and helps enable the discovery of new periodic orbit families.

2.5.1 Monodromy Matrix and its Eigenstructure

Determining the stability of a periodic orbit is important in evaluating its long-term behavior which, for stationkeeping problems, tends to directly correlates to the propellant needed to maintain a desired orbit. The more stable the orbit, the slower it will depart. But,

rather than determining the stability of a specific location on the orbit, the stability of the entire orbit is assessed and leveraged to find additional pathways through space. To analyze orbital stability, the STM after a full orbit is calculated. This matrix is called the monodromy matrix and is denoted $\Phi(t_0 + T, t_0)$ where T is the orbital period and t_0 is the initial time. The monodromy matrix, calculated starting from any point on the orbit, relates the variation in state after a period to the variation in initial state. To calculate, it is often convenient to use the final STM from the numerical propagation of the full, converged periodic orbit. Note that using a single shooter often targets only half the orbit if it leverages the Mirror Theorem, and the STM for a half-orbit is not equivalent to the monodromy matrix.

Since the monodromy matrix for the spatial problem is 6×6, six eigenvalues, λ_i, exist. For a periodic orbit, these eigenvalues will occur in reciprocal pairs with one pair equal to unity due to the orbit's periodicity and membership in a family of solutions. Furthermore, since the monodromy matrix provides a linear, discrete time mapping of the orbit, the stability bound is the unit circle as opposed to the imaginary axis for continuous time. As a result, the stability of the eigenvalues are categorized as follows.

1. If $|\lambda_i| > 1$, then perturbations grow with time and result in departing the orbit. The eigenvalue lies outside the unit circle and is unstable.

2. If $|\lambda_i| = 1$, then the eigenvalue lies on the unit circle and is marginally stable.

3. If $|\lambda_i| < 1$, then small perturbations tend towards zero. The eigenvalue lies within the unit circle and is stable.

2.5.2 Bifurcations

Each member of a periodic orbit family possesses its own stability properties, and evaluating any changes in stability along a family can potentially indicate an intersection with another family. Such an occurrence is called a bifurcation and is characterized by two dis-

tinct families sharing a particular member. To locate stability changes, it is convenient to use the stability index defined as

$$\nu_{\mathrm{i}} = \frac{1}{2}\left(|\lambda_{\mathrm{i}}| + \frac{1}{|\lambda_{\mathrm{i}}|}\right) \tag{2.81}$$

Eigenvalues occur in reciprocal pairs, so there are only three distinct stability indices using this definition. This formulation also prevents the loss of information from complex eigenvalues that occurs in certain families when the magnitude is not used in the stability index definition. When the stability index crosses the stability bound – unity for discrete time – there is a change in the characterization of the eigenvalues such as a complex pair becoming a real pair or vice versa. The unitary eigenvalue pair always exists, so there is always a stability index equal to one.

The first crossing of the stability bound in the L_2 Lyapunov family indicates a bifurcation to the L_2 halo family as illustrated in Figure 2.15. The bifurcating orbit, shown in black, belongs to both families and has two stability indices equal to one. From this orbit, it is possible to continue the L_2 Lyapunov family, continue into the L_2 southern halo family as shown, or continue up into the L_2 northern halo family.

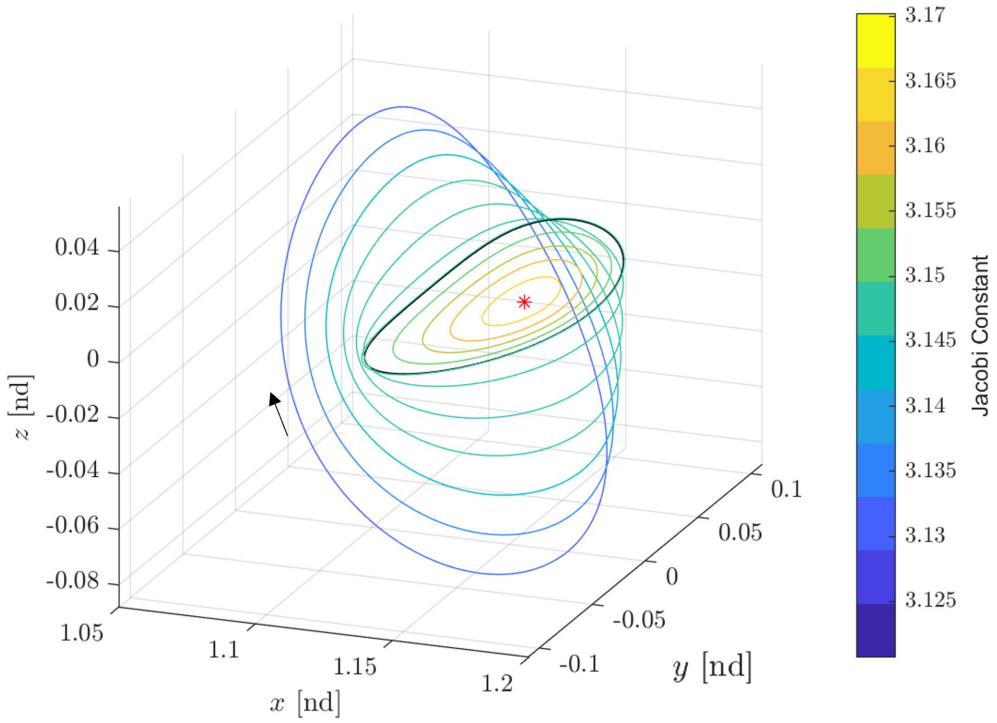

Figure 2.15. Bifurcation from the L_2 Lyapunov family to the L_2 southern halo family in the Earth-Moon system.

2.5.3 Lagrange Point Orbit Families

The L_1 Lyapunov and L_2 southern halo families illustrated in Figure 2.12 and 2.14 are both examples of Lagrange point orbit families. From the L_1 Lyapunov single shooting example, it is evident that this family encircles the L_1 Lagrange point. The L_2 southern halo family bifurcates from an L_2 Lyapunov orbit, which surrounds L_2 as its name implies, and remains in the vicinity of this Lagrange point. There are a several periodic orbit families near each of the five Lagrange points, all of which provide further understanding of the system and potential structures to be used in transfers.

L_2 Vertical Family

Starting with the L_2 Lyapunov family, two bifurcations are needed to arrive at the L_2 vertical family in Figure 2.16. This family is spatial with many of its members possessing large positive and negative out-of-plane components. The whole family, as depicted in Figure

2.16(a), has members strictly in the L_2 vicinity as well as members which extend out near L_3, providing several options to traverse this space if desired. Figure 2.16(b) illustrates motion in the L_2 vertical family close to the L_2 Lagrange point which resembles an elongated figure eight. Observe that the motion across most of the family is almost entirely out-of-plane with the exception of the two crossings of the $\hat{x}$-$\hat{y}$ plane.

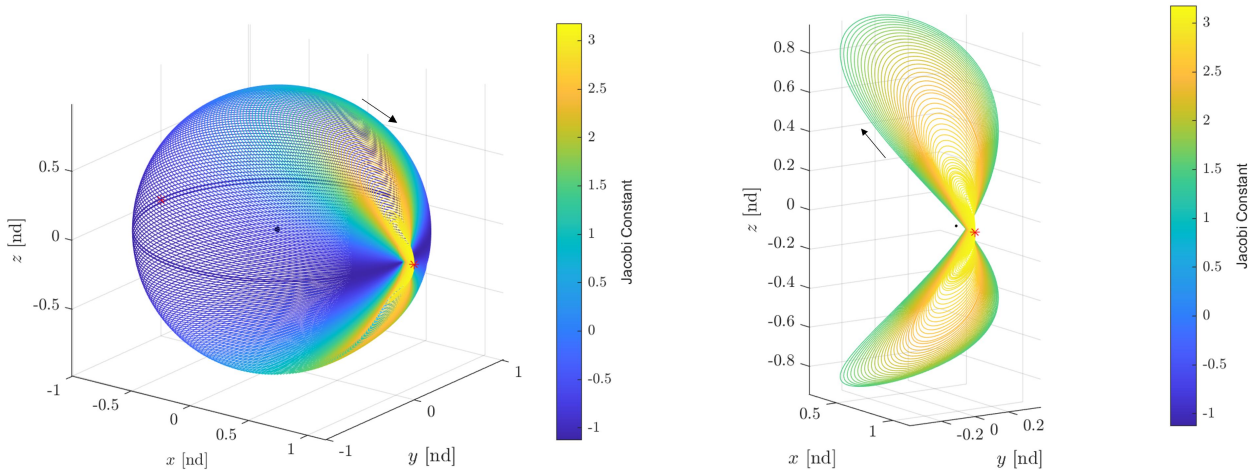

(a) Entire L_2 vertical family.

(b) Subset of the L_2 vertical family.

Figure 2.16. L_2 vertical family in the Earth-Moon system colored by Jacobi constant value.

2.5.4 Resonant Orbit Families

Another type of periodic orbit family of interest to this investigation is defined by a simple integer ratio between the orbital period and the period of the given system. For the Earth-Moon system, the period of the system is defined by the Moon's orbital period about the Earth, T_{Moon}. Thus, a resonant orbit in this system has the following resonance ratio

$$\frac{T_{orbit}}{T_{Moon}} = \frac{k_1}{k_2} \tag{2.82}$$

provided k_1 and k_2 are integers. This orbital resonance application is a subset of a larger universal marvel in which two or more bodies possess orbital parameters in ratios with each other. Large mass differences or close passes as a result of such resonance can lead to changes

in parameters and possible ejection from the system. The Kirkwood gaps in the asteroid belt serve as a prudent example of destabilization as a result of orbital resonance [32].

Planar 3:2 Resonant Orbit Family

A subset of the planar 3:2 resonant orbit family is illustrated in Figure 2.17 colored by Jacobi constant value. From Equation (2.82), the resonance ratio clearly indicates that the orbit completes three full periods in the time the Moon completes two revolutions of the Earth.

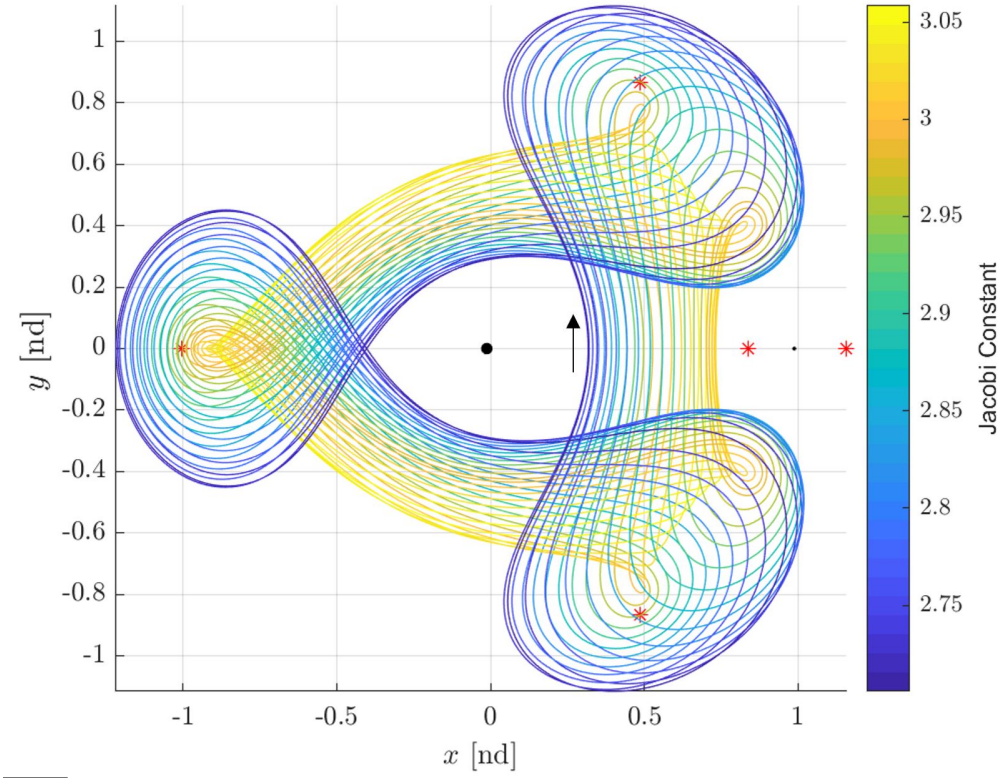

Figure 2.17. 3:2 planar resonant orbit family in the Earth-Moon system colored by Jacobi constant value.

Spatial 3:2 Resonant Orbit Family

As for Lagrange point orbit families, there exists many spatial resonant orbit families which bifurcate from planar resonant orbit families. Bifurcating from the planar 3:2 resonant

orbit family, the spatial 3:2 resonant orbit family extends beyond the lunar vicinity and encircles the Earth. Compared with the L_2 halo and L_2 vertical families, the spatial 3:2 resonant orbit family does not posses large maximum out-of-plane components.

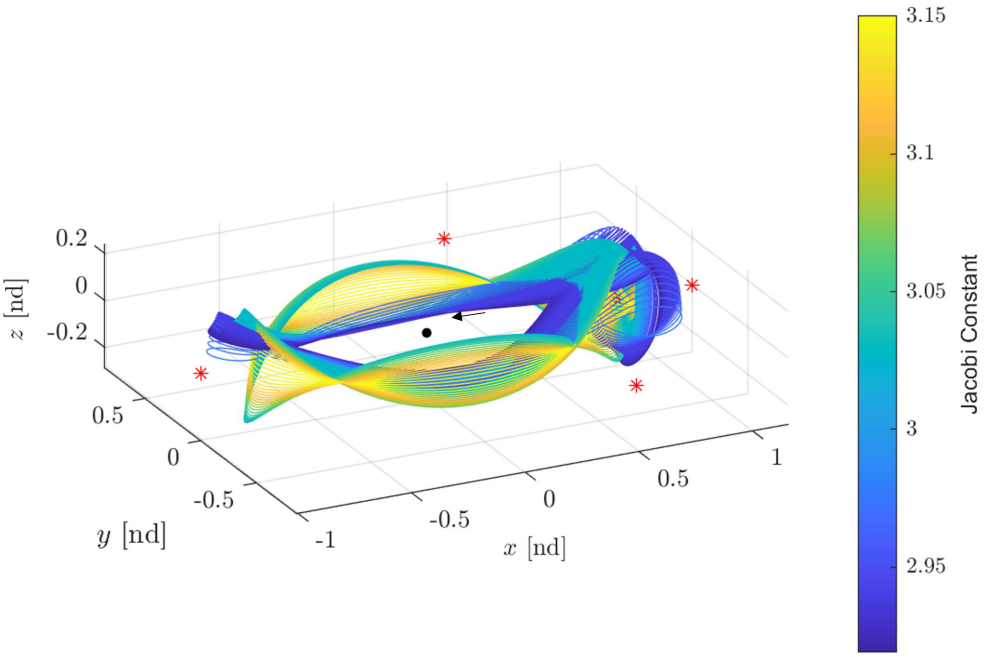

Figure 2.18. 3:2 spatial resonant orbit family in the Earth-Moon system colored by Jacobi constant value.

2.6 Invariant Manifold Theory

Stability properties reveal the nature of flow in the vicinity of an orbit which is often leveraged to depart from or arrive at an orbit at no cost. Specifically, invariant manifolds can be calculated using the eigenstructure of the monodromy matrix, and any point mass on these manifolds will remain on these manifolds indefinitely approaching or leaving the periodic orbit from which the monodromy matrix is calculated. Recall that eigenvalues of the monodromy matrix occur in reciprocal pairs. If $|\lambda_1| < 1$ then its reciprocal has the property $|\lambda_2| = \frac{1}{|\lambda_1|} > 1$. Thus, a periodic orbit with a stable mode also possesses an unstable mode. This means there exists flow that departs and flow that arrives at the orbit.

Since orbits are periodic, the eigenvalues of the monodromy matrix and, thus, the associated modes are independent of the fixed point from which λ_{i} are calculated. Contrarily, the eigenvectors, $\bar{v}_{\mathrm{i}}$, are dependent on the fixed point but can be transitioned using the STM by

$$\bar{v}_{\mathrm{i}}(t_1) = \Phi(t_1, t_0)\bar{v}_{\mathrm{i}}(t_0) \tag{2.83}$$

At each point along the orbit, the eigenvector that corresponds to the stable eigenvalue, $\bar{v}_s$, indicates the direction that the flow asymptotically approaches the fixed point, and, similarly, the eigenvector corresponding to the unstable eigenvalue, $\bar{v}_u$, identifies the direction that flow will asymptotically depart the fixed point. These eigenvectors are the only directions that flow can depart and arrive from.

Consider a particle shifted off of a fixed point of a periodic orbit in the direction of the stable and unstable eigenvectors. To do this, the stable eigenvector, the unstable eigenvector, the negative of the stable eigenvector, and the negative of the unstable eigenvector are first normalized by position to obtain $\bar{V}^{S+}$, $\bar{V}^{U+}$, $\bar{V}^{S-}$, and $\bar{V}^{U-}$, respectively. Next, the following equations are used to step along each normalized eigenvector

$$\bar{x}_{u+} = \bar{x}^* + d * \bar{V}^{U+} \tag{2.84}$$

$$\bar{x}_{u-} = \bar{x}^* + d * \bar{V}^{U-} \tag{2.85}$$

$$\bar{x}_{s+} = \bar{x}^* + d * \bar{V}^{S+} \tag{2.86}$$

$$\bar{x}_{s-} = \bar{x}^* + d * \bar{V}^{S-} \tag{2.87}$$

where $\bar{x}^*$ is the fixed point and d is a selected step size. In this investigation, the eigenvectors are normalized by position so the step size has physical meaning. For this normalization, $d = 50\ km$ is selected which is large enough so that the manifolds do not take a long time to depart the fixed point. Manifolds are only tangent to the eigenvectors at the fixed point, so

a step that is too large does not provide an accurate approximation. This step size of 50 km is small enough that the manifolds are sufficiently approximated.

The manifolds of a planar 3:2 resonant orbit with $C = 2.8107$, propagated for $t = 15\ [nd] = 65.2257\ days$ in Figure 2.19, provide a visual representation of how flow approaches the orbit on the stable manifold in blue and departs the orbit on the unstable manifolds in red. Despite the plots displaying only position space, the full six-dimensional eigenvectors are used to increment the entire state to step along a manifold, not just the position components. Note that the manifolds remain close to the resonant orbit for a duration before departing the vicinity for the unstable manifolds or after arriving for the stable manifolds. This geometry is a product of the maximum stability index. The larger the unstable eigenvalue, and thus the stability index, the faster the manifolds depart and approach the vicinity. Additionally, recall that an orbit with a stable mode must also possess an unstable mode. Both of these modes, which always exist together, are required for manifolds to exist. Manifolds present energy efficient pathways on which to travel through the system. By connecting manifolds from different orbits, new transfer options are available, and, if the Jacobi constant values of the initial and final orbits are equivalent, zero-cost transfers are now possible.

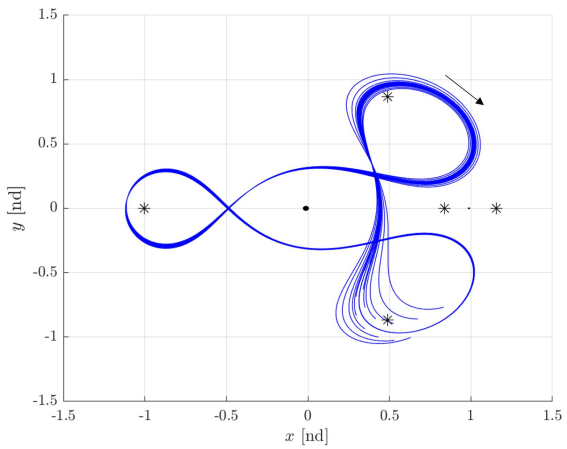

(a) Stable manifolds of a 3:2 planar resonant orbit.

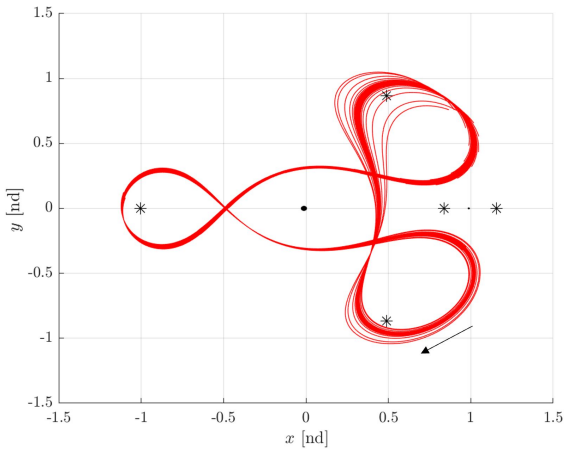

(b) Unstable manifolds of a 3:2 planar resonant orbit.

Figure 2.19. Manifolds of a 3:2 planar resonant orbit in the Earth-Moon system.

2.7 Poincaré Maps

Manifolds allow a spacecraft to depart or arrive at a periodic orbits at no cost, but, to travel from one orbit to another, it is necessary to connect these manifolds. Manifold connections are located with Poincaré maps, a tool to examine the vast design space through dimension reduction. Introduced by Henri Poincaré's in 1893 to analyze the CR3BP, Poincaré maps enable the visualization of transfer options through the application of hyperplanes, Σ [33]. Hyperplanes, defined at a physical location or in terms of an event such as an apse, are "inserted" into the design space, and manifolds or trajectories of interest are propagated to determine any crossings of Σ. These crossings are then plotted together on a map to determine if a segment arriving from somewhere and a segment going towards somewhere intersect. If such segments are identified, they are used as an initial guess for a transfer targeter.

To gain an intuition for Poincaré maps, consider a hyperplane inserted in space such that it intersects a periodic orbit. Then, suppose this periodic orbit and a subset of its manifold trajectories are propagated to their first crossing of Σ. A periodic orbit, as diagrammed in Figure 2.20, continuously intersects the map at the same fixed point, $\bar{x}^*$, since, by definition of periodicity, an orbit repeats the same path in six-dimensional space. Stable manifold trajectories approach the fixed point while unstable manifold trajectories diverge from the fixed point at each consecutive map crossing. Thus, unlike periodic orbits, manifold trajectories do not intersect the hyperplane at the same location at each map crossing.

For planar trajectories, a hyperplane defined at a physical variable, for example $y = 0$, often results in a two-dimensional map. The planar problem has four state variables since $z = \dot{z} = 0$ for all time. Further, the selected hyperplane eliminates the need to visualize y since this value has been fixed for crossings of Σ. If the initial and final orbits of a transfer have the same Jacobi constant value, another variable is determined. Since the Jacobi constant value is constant, the Jacobi constant equation will yield the same final state variable for an intersection on the two-dimensional map. Thus, for a planar transfer with a fixed value of C, only a two-dimensional Poincaré map is required. This concept is directly applicable to spatial transfers. Fixing the Jacobi constant value and defining Σ at a state

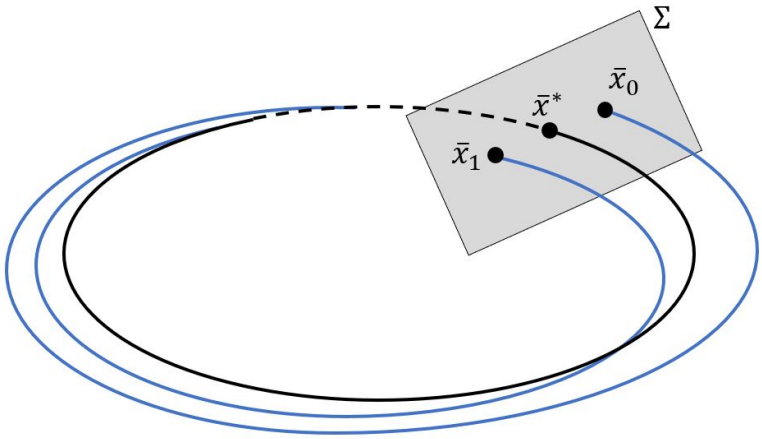

Figure 2.20. Poincaré map diagram.

variable reduces the six-dimensional space to four. As discussed in later chapters, visualizing four or more dimensions creates various challenges and opportunities when exploring spatial transfers.

The applications of Poincaré maps expand beyond connecting periodic orbit manifolds. Any type of trajectory arc can be displayed on a map, provided it intersects the hyperplane. For example, applying a maneuver on a periodic orbit results in a trajectory that departs the orbit. Then, instead of using the orbit's manifolds, trajectories resulting from maneuvers at different locations on the orbit are propagated to determine crossings of the hyperplane. A map then reveals if these trajectories intersect other such arcs, orbits, or manifolds.

3. POINCARÉ MAPS AND TRAJECTORY DESIGN IN THE CR3BP

Poincaré maps are a versatile and powerful tool for trajectory analysis and construction in the CR3BP. Through strategic placement of a hyperplane, intersections of orbits, their associated manifolds, and other arcs are examined to construct favorable transits through space. Any combination and number of intermediate segments may be leveraged, but it is often convenient to limit the number of arcs to restrict complexity and numerical challenges. For corrections purposes, larger arcs are often decomposed with patch points to aid in differential corrections convergence properties. The focus of this investigation is the design of cislunar transfers in the Earth-Moon system with distinct initial and final orbits as well as the aid of Poincaré mapping strategies. Planar trajectory design is introduced first in this chapter before expanding into spatial transfers. In all cases, maps are utilized to generate an initial guess for the intermediate arcs along a transfer. While intermediate arcs can include, but are not limited to, tangential departures, tangential arrivals, and resonant arcs, this chapter focuses on stable and unstable manifolds. With maps to visualize the solution space, it is feasible to sort through the vast options and select arcs that result in transfers with desired characteristics.

3.1 Theoretical Minimum Maneuver

The theoretical minimum ΔV is the minimum maneuver magnitude that is necessary to shift a trajectory's current Jacobi constant value to a different value of Jacobi constant. This minimum value is envisioned as a single tangential maneuver at a specific location to change the energy. Additionally, this value offers a qualitative assessment of the effectiveness of a maneuver. To calculate the theoretical minimum ΔV, let two trajectories be described with distinct Jacobi constants such that

$$C_1 = 2U_1^* - v_1^2 \tag{3.1}$$

$$C_2 = 2U_2^* - v_2^2 \tag{3.2}$$

It is known that $U_1^* = U_2^*$ if these two segments meet in position space as the pseudo-potential, U^*, is a function only of position. The difference in Jacobi constant is then reduced to

$$\Delta C = v_2^2 - v_1^2 \tag{3.3}$$

Determining the difference in the velocity magnitude as

$$\Delta V = \sqrt{v_1^2 + v_2^2 - 2v_1 v_2 cos\theta} \tag{3.4}$$

it is clear that the minimum ΔV occurs when $cos\theta = 1$. Rearranging Equation (3.3) to solve for v_2, Equation (3.4) is expressed as follows,

$$\Delta V_{min} = \sqrt{2v_1^2 + \Delta C - 2v_1\sqrt{\Delta C + v_1^2}} \tag{3.5}$$

where ΔV_{min} is the minimum velocity change necessary to overcome the given difference in Jacobi constant value. It is apparent that the theoretical minimum ΔV occurs when two trajectory segments are tangent. Any additional change in direction will only increase the maneuver magnitude.

3.2 Transfer Design

To construct a transfer between two periodic orbits, a multiple shooting targeting algorithm is formulated. A transfer leveraging manifolds requires the incorporation of a manifold constraint between a periodic orbit and its associated manifold trajectory in place of the standard position and velocity continuity between arcs. In this investigation, the transfer targeting algorithm that leverages manifolds to connect periodic orbits is based on the method implemented by Haapala as well as Haapala and Howell to compute free and low cost transfers [23], [24]. This algorithm is applicable to both planar and spatial transfers.

The diagram of this transfer scheme in Figure 3.1 depicts an initial orbit defined by a state $\bar{x}_1$ and a final orbit defined by a state $\bar{x}_2$. As demonstrated in later sections, the manifold trajectories for the transfer initial guess are selected from a Poincaré map and are generally located near each other in position space. In Figure 3.1 the green box highlights the selected unstable manifold state, $\bar{x}_{u,f}$, and the selected stable manifold state, $\bar{x}_{s,0}$ from a generated map. The unstable manifold state is propagated backwards in time until it reaches the initial orbit. The end of this propagation occurs first in time so this state is denoted $\bar{x}_{u,0}$ and the time along the manifold is T_u. The stable manifold state is propagated forward in time for T_s until it reaches its final state, $\bar{x}_{s,f}$. The states that define each of the selected orbits are also propagated forward in time, for τ_1 and τ_2 respectively, until the manifold step off location is reached. The step offs onto the manifolds from the orbits are performed as described in Section 2.6. Note the step offs are not considered trajectory arcs; instead, the step offs are used in the manifold constraints

$$\bar{x}_u - \bar{x}_{u,0} = \bar{x}_u^* + d * \bar{V}^U - \bar{x}_{u,0} = \bar{0} \tag{3.6}$$

$$\bar{x}_s - \bar{x}_{s,f} = \bar{x}_s^* + d * \bar{V}^S - \bar{x}_{s,f} = \bar{0} \tag{3.7}$$

where each step off from an orbit must be continuous in position and velocity with its associated manifold trajectory. Unless allowing for a maneuver, the final states of all other arcs are continuous in both position and velocity with the beginning of the next arcs.

For this investigation, $\bar{x}_1$ and $\bar{x}_2$ are not included in the design vector. Thus, the initial and final orbits are not able to change, and the initial and final Jacobi constant values are fixed. After the design and constraint vectors are constructed, the transfer targeting algorithm iterates until the magnitude of the constraint vector is within a specified tolerance. The converged transfer has a time-of-flight (TOF) of $T_u + T_s$ as this is the time to travel from the step off location on the initial orbit to the step off location on the final orbit.

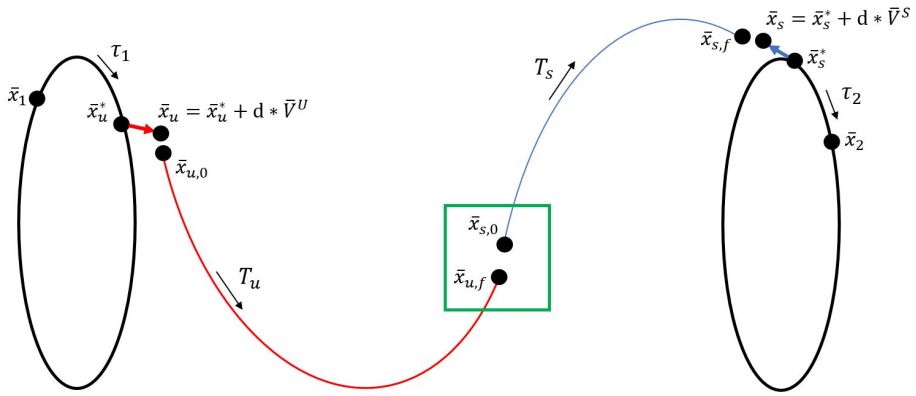

Figure 3.1. Transfer targeting diagram using manifold trajectories.

3.3 Planar Transfers

By definition, planar transfers are defined such that $z = \dot{z} = 0$ for all time, reducing the dimensionality of the problem and, thus, easing the visualization of the design space. The state space is then comprised of x, y, $\dot{x}$, $\dot{y}$. Selection of a hyperplane, Σ, may involve only the states, e.g., $y = y_c$, which then determines one scalar function of the states and reduces the unknown states by one. Subsequently, any crossings of Σ are recorded. The remaining unknown state variables are then plotted on a map to locate potential transfers. Some specific design scenarios illustrate the flexibility of this strategy. Thus, to demonstrate the trajectory design process as well as the significance and versatility of Poincaré maps, transfers between L_1 Lyapunov and L_2 Lyapunov orbits are constructed in this section.

3.3.1 Fixed Jacobi Constant Transfers

Consider planar L_1 and L_2 Lyapunov orbits, both defined by a value of $C = 3.15$. To construct a transfer between these two orbits plotted in Figure 3.2, the manifolds are propagated towards the Moon, as demonstrated in Figure 3.3, until each of the paths reaches $\Sigma : x = 1 - \mu$. If $\Delta C = 0$ is introduced from Equation (3.5), then the theoretical minimum ΔV is zero if a tangential intersection occurs. Therefore, a Poincaré map allows a search for a heteroclinic connection, that is, a free transfer between two distinct orbits. Because both orbits possess the same value of C, a map with only two variables is required, as the Jacobi

constant equation offers a scalar relationship between the states. Thus, an intersection in any two states on a planar Poincaré map, is an intersection of all four states.

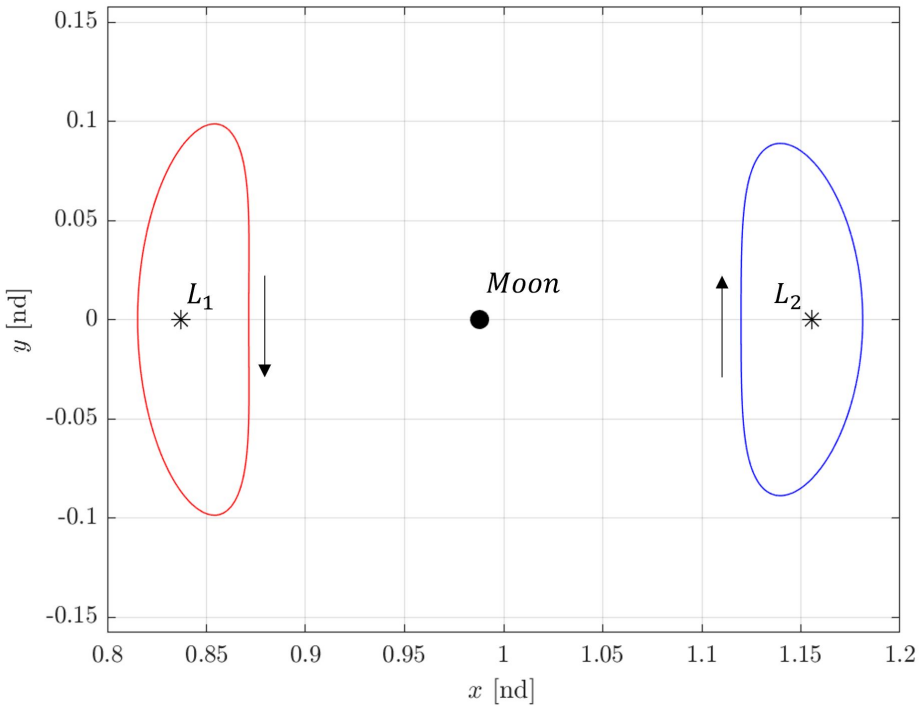

Figure 3.2. Selected L_1 Lyapunov and L_2 Lyapunov orbits with $C = 3.15$ for transfer design in the Earth-Moon system.

Since all crossings of the hyperplane are located at $x = 1 - \mu$, any two of the three remaining state variables are available to create a map. Two different Poincaré maps for this transfer scenario are displayed in Figure 3.4. The direct correlation in Figure 3.4(a) provides limited information for transfers as the stable and unstable manifold points nearly overlay each other in much of the interesting region in the plot, suggesting that there exists many free transfer options. In comparison, the options in Figure 3.4(b) appear more limited. A zoomed-in view of the y vs $\dot{y}$ map in Figure 3.5 reveals that there are two specific intersections of the stable and unstable manifolds numerically, determined through extrapolation, the propagation of additional manifolds, or the application of differential methods. Figure 3.4 highlights the value of selecting variables for Poincaré maps that offer the most information. At the selected hyperplane, i.e., $x = 1 - \mu$, the velocity direction is notable. As the distance from the Moon increases, the velocity perpendicular to its position vector relative to the

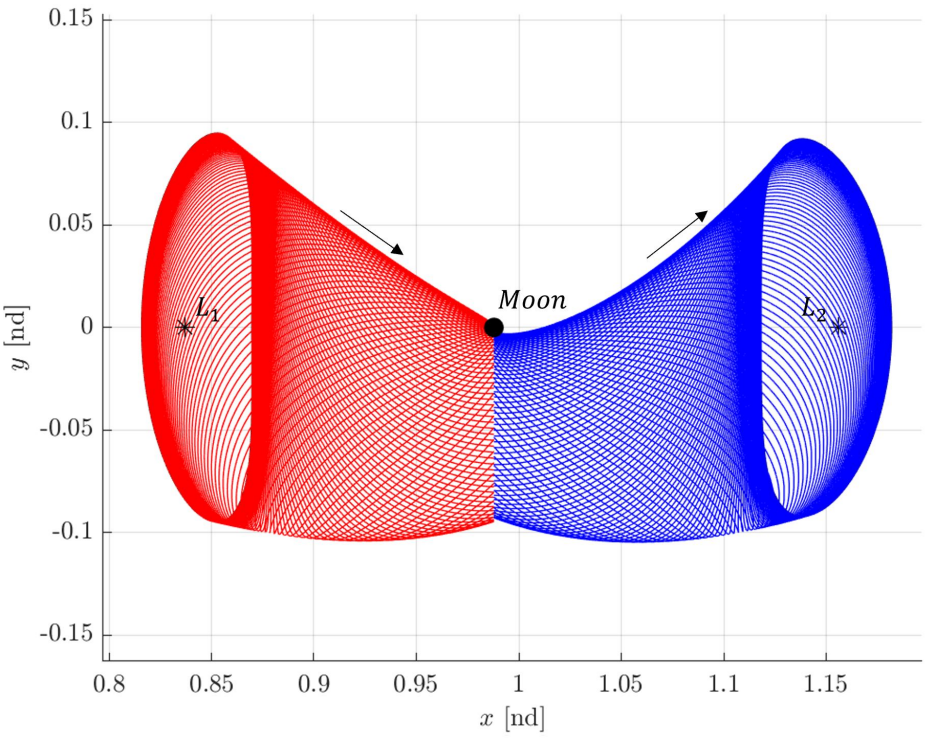

Figure 3.3. L_1 Lyapunov unstable manifolds and L_2 Lyapunov stable manifolds that approach the Moon for C=3.15.

Moon decreases. Thus, due to this correspondence, a map of y vs $\dot{x}$ does not yield as insightful information as a map of y vs $\dot{y}$.

Manifolds form a higher-dimensional surface as the number of fixed points on the originating orbit approaches infinity, so the curves in Figure 3.5 overlap and, thus, two specific manifold trajectories intersect in all dimensions given the correct fixed points on the initial and final orbits. Selecting the unstable and stable manifold states closest to an intersection on this map and employing a numerical corrections scheme produces a heteroclinic transfer, i.e., $\Delta V = 0$. Propagating the circled unstable and stable manifold states in this map backward and forward in time, respectively, results in an initial guess that is discontinuous at the hyperplane $x = 1 - \mu$. After applying the transfer targeter described in Section 3.2, the converged transfer is plotted in Figure 3.6. This transfer is ballistic and, thus, is continuous in position and velocity space with a time-of-flight, or time along the manifolds, of $5.813\ [nd] = 25.278\ days$.

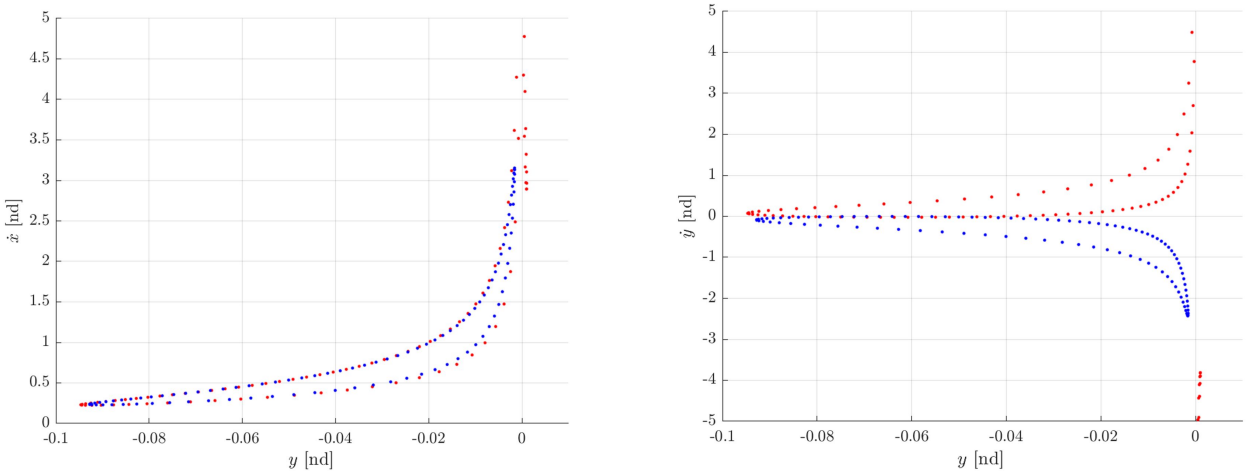

(a) y vs $\dot{x}$ (b) y vs $\dot{y}$

Figure 3.4. Two-dimensional Poincaré maps for L_1 Lyapunov unstable manifold trajectories and L_2 Lyapunov stable manifold trajectories with fixed $C = 3.15$.

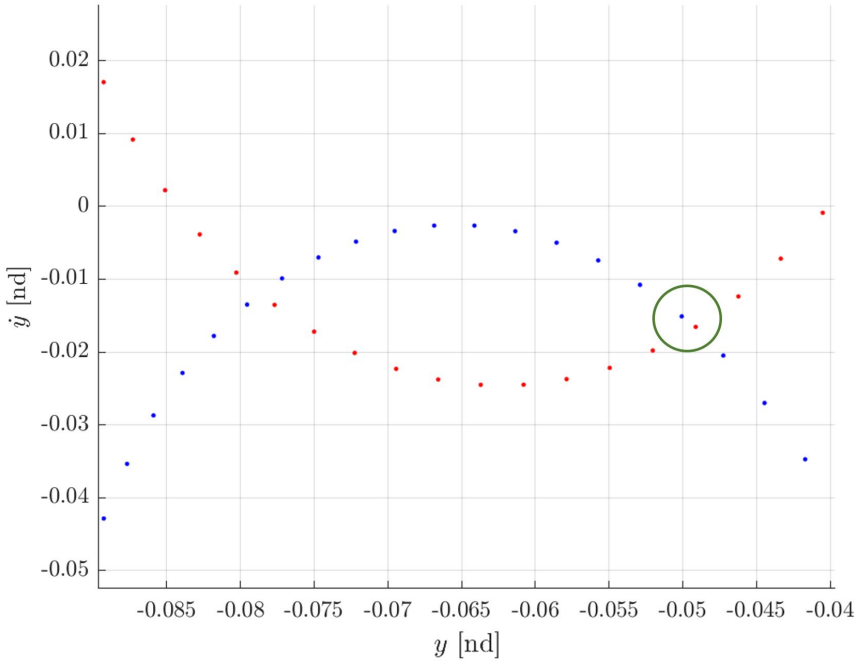

Figure 3.5. Zoomed-in Poincaré map for L_1 Lyapunov unstable manifold trajectories and L_2 Lyapunov stable manifold trajectories with fixed $C = 3.15$.

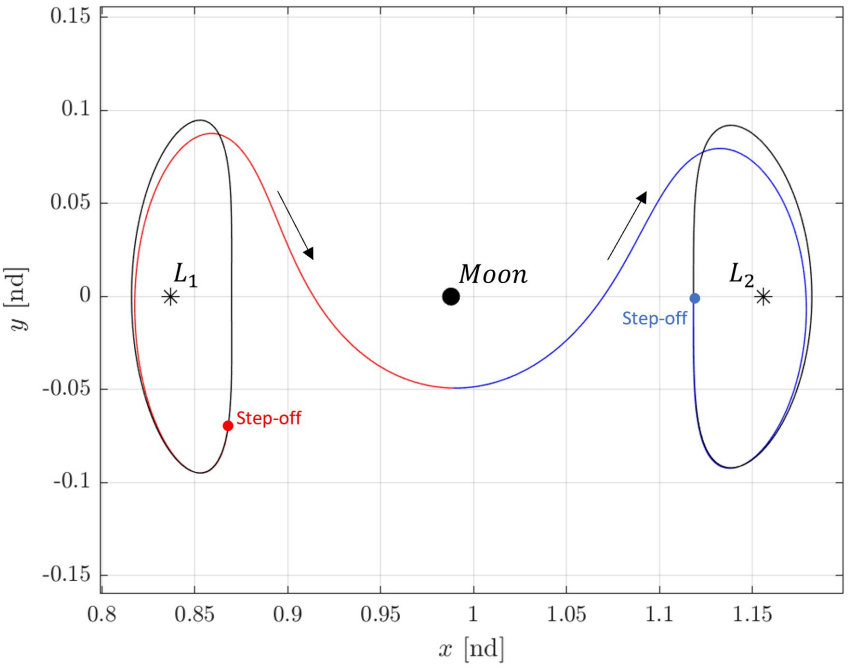

Figure 3.6. L_1 Lyapunov to L_2 Lyapunov heteroclinic transfer for $C = 3.15$ in the Earth-Moon system. The Moon is plotted to scale.

3.3.2 Varying Hyperplane Location in Configuration Space

In additional to the selection of map variables (in terms of the states), the utility of Poincaré maps to aid in transfer design is the definition of the hyperplane. For transfer design, a hyperplane – either physical or defined in terms of an event – is selected such that the dynamical flow intersects the hyperplane several times, presenting various options. The location or definition of the hyperplane is frequently informed by various types of mission constraints. For example, defining a physical hyperplane at the position $x = 1 - \mu$ in configuration space, a transfer designed from an L_1 Lyapunov orbit to an L_2 Lyapunov orbit is potentially low cost as the intersecting trajectories' velocity vectors are nearly tangent at this hyperplane. This outcome is advantageous because a tangential maneuver results in the lowest possible maneuver cost.

Geometrical hyperplanes can be defined in various orientations in configuration space and highlight a desired transfer. For L_1 and L_2 Lyapunov orbits with the same value of Jacobi constant, $C = 3.15$, there exist manifold structures that cross the $\hat{x}$-axis near the Moon, so a hyperplane is easily defined at $y = 0$. Additionally, by restricting intersections to those that occur left of the Moon, the resulting manifold trajectories in Figure 3.7 and, thus, the resulting maps in Figure 3.8 possess crossings that yield initial guesses from the near-intersections. The heteroclinic connection in Figure 3.9, produced via corrections of the initial guess corresponding to the circled intersection in Figure 3.8(a), highlights the versatility of hyperplanes. While both the $x = 1 - \mu$ and the $y = 0$ hyperplanes result in heteroclinic transfers, clearly the manifold intersection occurs at a different location in configuration space. However, note that the transfer utilizing $\Sigma : y = 0$ has a time-of-flight of $5.813\ [nd] = 25.278\ days$ which is approximately that of the converged transfer using $\Sigma : x = 1 - \mu$. This is not surprising since both options have a fixed Jacobi constant of 3.15. Verified by comparing the six-dimensional state along the two converged transfers, the same transfer trajectory is obtained using different hyperplanes with the main difference being the location where the unstable and stable manifold trajectories meet.

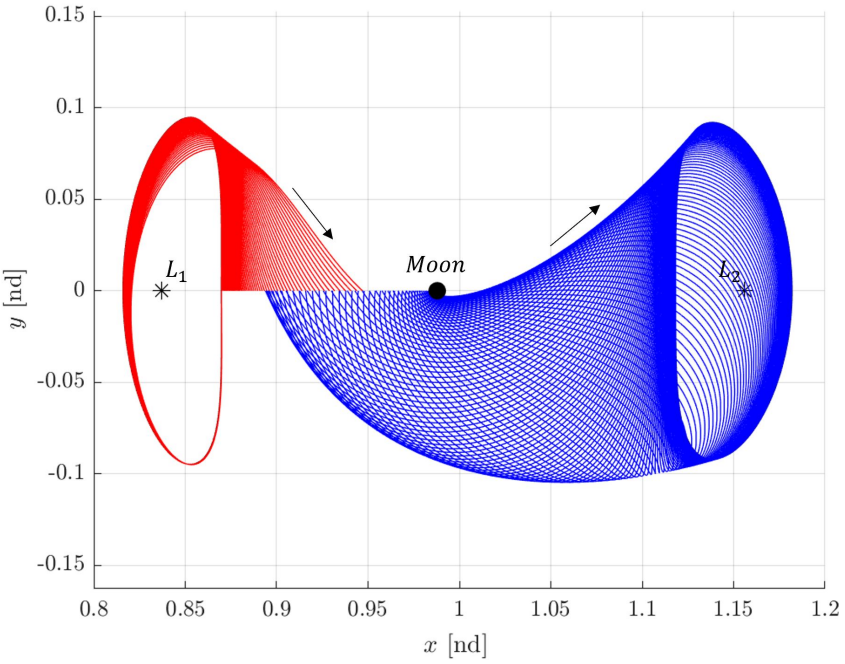

Figure 3.7. L_1 Lyapunov unstable manifolds and L_2 Lyapunov stable manifolds for fixed $C = 3.15$ that intersect the $y = 0$ hyperplane on the left side of the Moon.

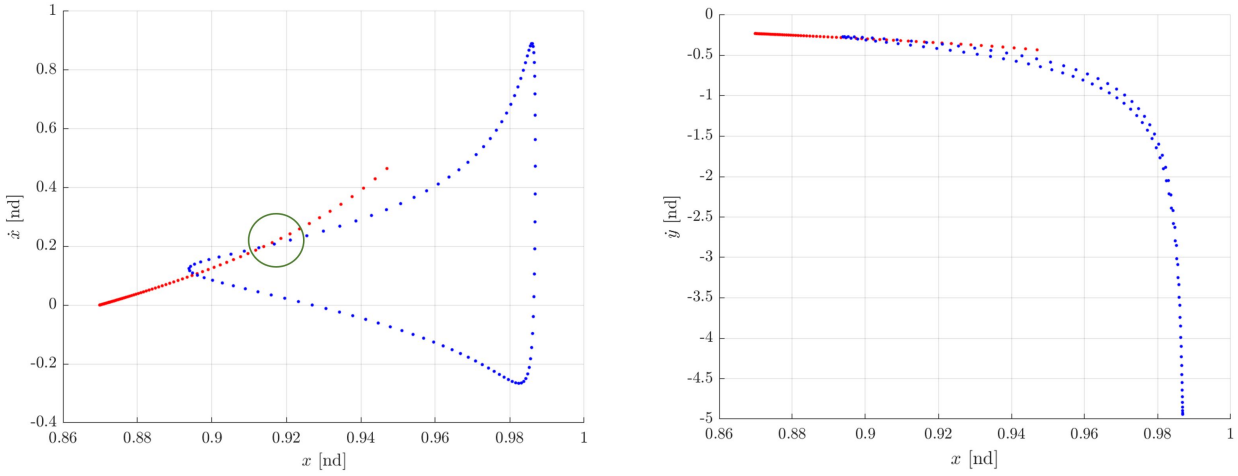

(a) x vs $\dot{x}$ (b) x vs $\dot{y}$

Figure 3.8. Two-dimensional Poincaré maps for L_1 Lyapunov unstable manifold trajectories and L_2 Lyapunov stable manifold trajectories with fixed $C = 3.15$ at crossings of $\Sigma : y = 0$ on the left side of the Moon.

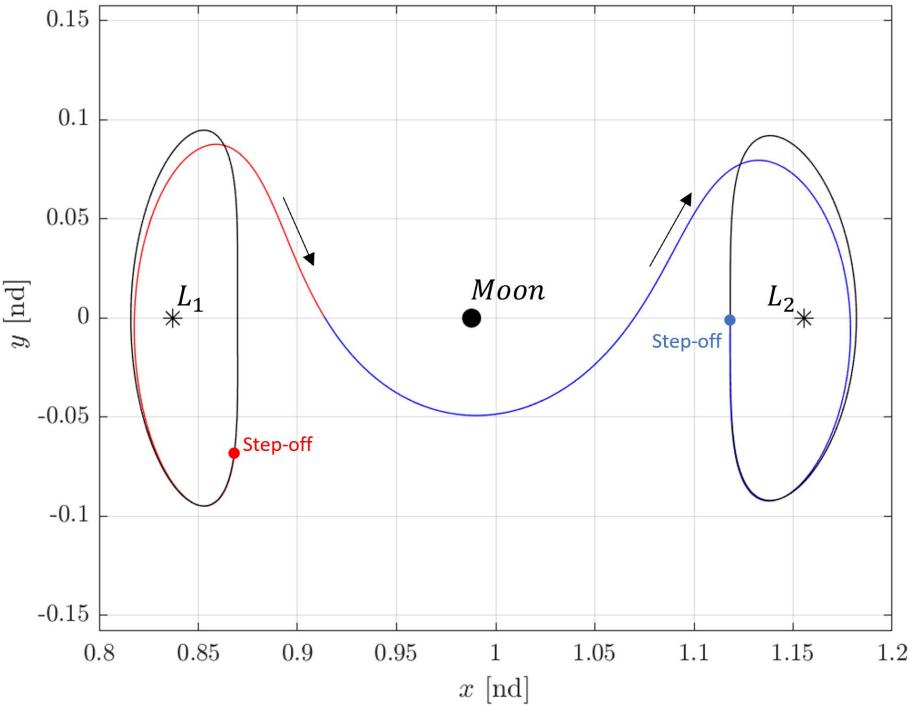

Figure 3.9. L_1 Lyapunov to L_2 Lyapunov heteroclinic transfer for $C = 3.15$ in the Earth-Moon system obtained using $\Sigma : y = 0$.

3.3.3 Transfers Between Orbits with Distinct Jacobi Constant Values

For a planar transfer constructed using manifolds between two orbits with the same Jacobi constant value, a Poincaré map only requires two variables. Because both the stable and unstable manifold trajectories possess the same C value, any intersection in the two-dimensional map serves as an intersection of the full state vectors. Thus, a free transfer is visualized using only two variables. This concept is no longer true if the initial and final orbits possess different Jacobi constant values. Because the orbits exist at different energy levels, a heteroclinic connection is not possible, i.e., $\Delta V_{min} \neq 0$. The Jacobi constant is a function of only the relative position and velocity states, so two distinct values of C can only result from two distinct state vectors. Thus, it is not possible for unstable and stable manifold trajectories with different Jacobi constant values to be continuous in both position and velocity. Despite the lack of a cost-free transfer, a transfer between two periodic orbits with different C values and a small maneuver is still accomplished with a map to reduce the ΔV maneuver cost that is required to overcome the energy gap.

To construct a transfer, determining a close intersection in the planar position and velocity initiates the process. Three variables are displayed on the Poincaré map to produce an initial guess. Recall that the third variable can no longer be deduced from a two-dimensional map due to the variation in Jacobi constant. If an exact intersection of an unstable manifold trajectory and a stable manifold trajectory with different values of C exist on a two-dimensional map, the Jacobi constant equation will produce two distinct values for the final state variable since they manifold trajectories have distinct values of C. Consider a periodic L_1 Lyapunov orbit with $C = 3.15$ and maximum y-amplitude of $0.0948\ [nd] = 36471.6256\ km$ as well as a periodic L_2 Lyapunov orbit with $C = 3.13$ and maximum y-amplitude of $0.1269\ [nd] = 48805.9830\ km$. Let the hyperplane again be defined in configuration space at $x = 1 - \mu$. To emphasize the smoothly evolving curve in the resultant Poincaré map in Figure 3.10, three hundred fixed points along each orbit are employed to propagate the manifolds. As expected, there are no exact intersections of the manifolds due to the disparate values of C; however, a near intersection is corrected for position continuity while allowing a maneuver at the manifold intersection. To accomplish this, the

targeting algorithm detailed in Section 3.2 is used, but only position continuity is enforced at the intersection of the unstable and stable manifold trajectories. The converged transfer in Figure 3.11 includes a maneuver magnitude of 0.01272 $[nd] = 0.01302\ km/s$, located at the green point, and a time-of-flight of 5.8947 $[nd] = 25.6325\ days$. The theoretical minimum ΔV at the manifold intersection is 0.01268 $[nd] = 0.01299\ km/s$ which, as expected for a near intersection of the full state, is only $3.6 * 10^{-5}$ $[nd]$ less than the calculated maneuver. For the maneuver to be equivalent to the theoretical minimum ΔV, the unstable and stable manifold trajectories would need to be tangent at this location which they are not for the given Jacobi constant value and intersection location.

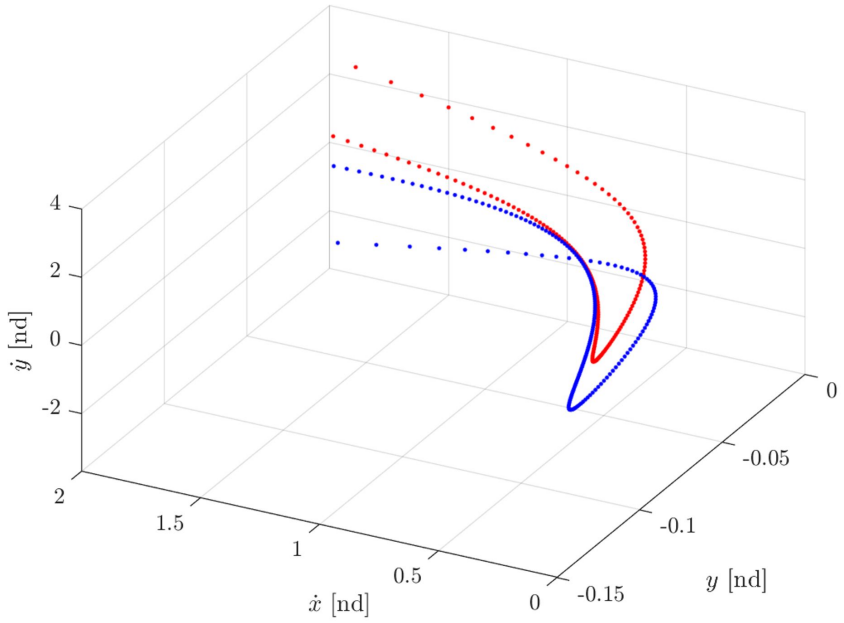

Figure 3.10. Three-dimensional Poincaré map for L_1 Lyapunov unstable manifold trajectories and L_2 Lyapunov stable manifold trajectories with $\Delta C = 0.02$ using $\Sigma : x = 1 - \mu$.

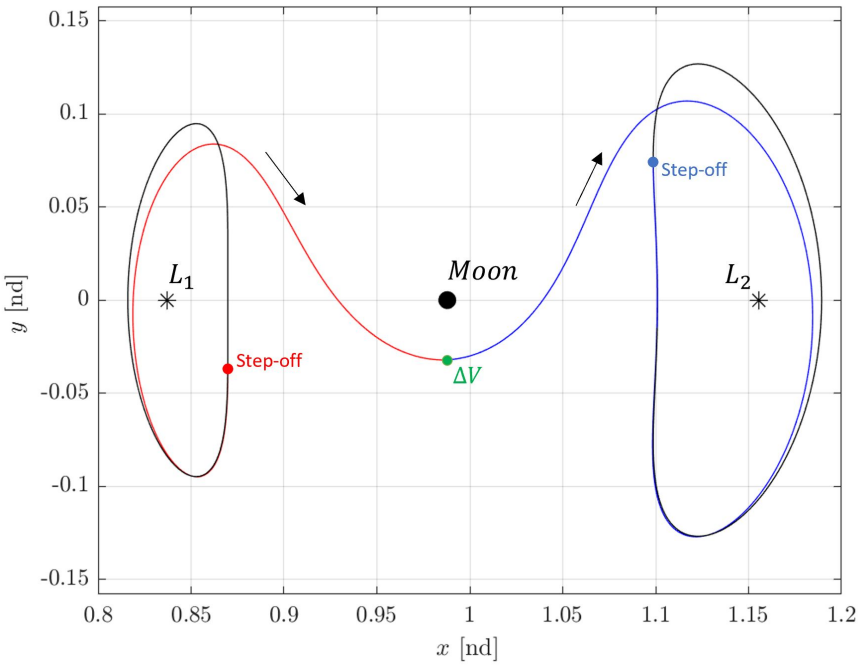

Figure 3.11. Transfer from an L_1 Lyapunov orbit to an L_2 Lyapunov orbit with $\Delta C = 0.02$ in the Earth-Moon system obtained using $\Sigma : y = 0$.

3.4 Spatial Transfers

As opposed to planar transfers, spatial transfers involve the intersection of the full six-dimensional state. Defining a hyperplane in terms of a geometrical location, such as $y = 0$, eliminates one state variable as does a constrained value of the Jacobi constant. Thus, the application of Poincaré mapping reduces the design space from six to four state variables for visualization for a spatial transfer. It is possible to construct a transfer via a map that plots only a subset of the remaining four state variables. For example, a map of the remaining position components allows for the identification of an intersection in position space. Other visualization options, including the use of several maps simultaneously, also allow for an informed and adequate selection of a transfer initial guess. Such approaches, however, do not offer a full visualization or understanding of the available solution space. Only a slice of the design space is available. In the following chapter, the application of different visualization techniques that incorporate three or more state variables on one map are introduced in addition to the application of different sets of variables to highlight the

transfer possibilities given mission constraints. While no one systematic strategy exists to find the ”optimal” transfer between any two orbits, the visualization of the entire state, as explored in the next chapter, allows for a more complete view of the options for a selected hyperplane.

4. HIGHER-DIMENSIONAL POINCARÉ MAPS AND THEIR APPLICATIONS

To construct a favorable transfer, it is important to determine constraints that are imperative to the mission. For example, human spaceflight necessitates minimal time-of-flight due to life support requirements and risk mitigation while CubeSat missions often seek to minimize propellant cost. Mission constraints and desired characteristics inform Poincaré maps to filter the design space and locate transfers of interest. This chapter introduces impulsive maneuvers along periodic orbits to create additional, low time-of-flight arcs for use in trajectory design. Subsequently, higher-dimensional maps using glyphs and color are employed to design spatial transfers involving the 9:2 NRHO. Finally, maps with non-state variables are leveraged to obtain transfers with desired characteristics.

4.1 Mission Design: 9:2 Synodic Resonant NRHO

Near-future lunar missions by NASA center around the L_2 southern 9:2 lunar synodic resonant NRHO. The Gateway, a planned space station that will orbit the Moon, will be located in this nearly stable orbit to minimize stationkeeping costs and provide access to the lunar surface, constant communication, and returns to Earth [34]. The 9:2 ratio indicates that this member of the L_2 southern halo family completes nine orbits in the time the Moon completes two synodic periods. The synodic period of the Moon is calculated as

$$T_s = \frac{2\pi}{\omega_s} \tag{4.1}$$

where ω_s is the Sun's angular rate calculated using SPICE ephemeris data provided by the Jet Propulsion Laboratory [35]. For the calendar year of 2022, the average synodic period is approximately $T_s = 29.4873\ days$. Due to the fixed ratio between orbits of the NRHO and the synodic period of the Moon, a fixed-time multiple shooter with a period of $\frac{2*T_s}{9}$ is utilized to obtain the exact 9:2 NRHO that is shown in Figure 2.11(b). The converged orbit has a Jacobi constant value of $C = 3.0468$ and an apolune radius of about 71,179 km.

The 9:2 NRHO is nearly stable with a maximum stability index, as defined in Equation (2.81), of 1.31. As a result of its stability properties, the unstable and stable manifolds

of this orbit remain close to the orbit for several revolutions before departing the vicinity. In Figure 4.1, the unstable manifolds are propagated for 13 $[nd] = 56.5289$ *days*, and, as apparent, they remain close to their originating orbit for this time.

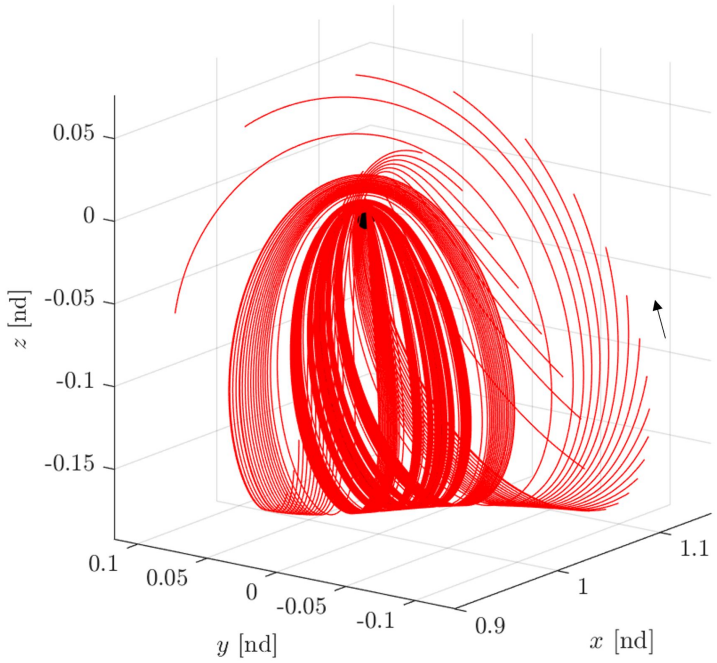

Figure 4.1. Unstable manifolds of the L_2 southern 9:2 synodic resonant NRHO in the Earth-Moon system.

4.2 Impulsive Maneuvers

Invariant manifolds provide pathways through space which leverage natural dynamical motion at no cost. These manifolds are defined by their originating orbit and its Jacobi constant value, i.e., a specific orbit has fixed manifold structures. If it is desired to access different regions of space or change value of Jacobi constant, impulsive maneuvers are used. Previously, an impulsive maneuver was utilized to jump from an unstable manifold onto a stable manifold with a different value of C; however, the potential usage is much wider. For example, if the unstable manifolds of the initial orbit directly intersect the final orbit, an impulsive maneuver can be used to jump directly onto the orbit without the need for stable manifolds. Augmenting this option, an impulsive maneuver can be applied on the initial

orbit to immediately change value of Jacobi constant to that of the final orbit. Both of these options potentially reduce the time-of-flight. Since the 9:2 NRHO is nearly stable, the manifolds do not depart as quickly as the manifolds of an unstable orbit. Instead of utilizing the 9:2 NRHO's unstable manifolds, an impulsive maneuver reduces the time to reach the destination orbit, provided the resultant flow has a desirable geometry.

For this investigation, the magnitude of impulsive maneuvers applied at the initial orbit, the 9:2 NRHO, are such that the resultant arc's Jacobi constant value equals that of the destination orbit. To evaluate the impulsive maneuver options along the initial orbit, the NRHO is discretized and, at each point, the ΔV required to overcome the energy gap is calculated according to Equation (3.5). Thus, a different ΔV is applied at each point, but all maneuvers are tangent to the orbit to leverage the properties of the theoretical minimum ΔV. These ΔVs represent the minimum maneuver magnitude at each point needed to overcome the difference in Jacobi constant value. Because these maneuvers are chosen to be tangential, there is no additional ΔV to overcome a difference in velocity direction. Therefore, these applied ΔVs are the best guess for a maneuver to depart the 9:2 NRHO and change the Jacobi constant value to that of the final orbit.

4.3 Higher-Dimensional Maps

Poincaré maps are used in trajectory design to locate near-intersection of arcs with desired characteristics. Planar scatter plot maps, such as those used to design heteroclinic transfers in the previous chapter, only allow the visualization of two state variables as is sufficient for a planar transfer with a fixed value of Jacobi constant. Spatial scatter plots illustrate three state variables for construction of low-cost planar transfers between two orbits with distinct Jacobi constant values. Augmenting the planar problem with z and $\dot{z}$ results in the spatial problem. Using the traditional scatter plot method of Poincaré maps, it is not possible to visualize the full six-dimensional state, which limits insight when designing transfers. As opposed to using two or more maps simultaneously, which only provide slices of information that are difficult to correlate, this section focuses on higher-dimensional Poincaré mapping

strategies that allow for the visualization of the full state on one map when designing spatial transfers.

4.3.1 Fixed Jacobi Constant Transfers

Consider a transfer between two spatial orbits with the same Jacobi constant value. For the spatial problem, the full state is comprised of six variables as opposed to four for the planar case. Defining a hyperplane at a physical state and constraining the Jacobi constant values of the initial and final orbits to be equivalent eliminates two state variables needed in a Poincaré map. To add two additional variables to a planar map, glyphs, or arrows, are utilized in combination with a scatter plot similar to the method exemplified by Haapala [23]. Assuming a hyperplane at a position state, the remaining two position components are expressed as points on the map. Each point serves as the new origin for an arrow whose direction indicates the orientation of two velocity components, such as $\dot{x}$ and $\dot{y}$, and magnitude corresponds to the magnitude of the same velocity components, i.e., $\sqrt{\dot{x}^2 + \dot{y}^2}$. To ease visualization and comparison, the glyphs are scaled; however, this does not impact the outcome as the objective is to identify two glyphs that, ideally, overlap.

Transfer to a 3:2 Planar Resonant Orbit: Unstable Manifold to Stable Manifold

The range of Jacobi constant values for the 3:2 planar resonant orbit family includes the Jacobi constant value of the 9:2 NRHO, $C = 3.0468$. Thus, it is possible to construct a transfer from the selected 9:2 NRHO to a 3:2 planar resonant orbit with the same value of C. A 3:2 planar resonant orbit is an advantageous destination orbit because it allows for a tour of the system and demonstrates a transfer to a planar orbit. The selected two orbits, shown in Figure 4.2, are nearly perpendicular to each other. The hyperplane is defined at $z = 0$ since the final orbit, and thus its manifolds, are planar. As a result, the entirety of the 3:2 planar resonant orbit stable manifolds are in the hyperplane. The unstable manifolds of the NRHO and the stable manifolds of the 3:2 planar resonant orbit are propagated for $25\ [nd] = 108.709\ days$ and crossings of Σ are plotted in Figure 4.3. In this map, red and blue denote the unstable and stable manifold crossings, respectively, and the glyphs

indicate the magnitude and direction of the in-plane velocity. Recalling that all of the 3:2 planar resonant orbit manifolds are located in the hyperplane, a representative number of the stable manifold states are included in the map. An initial guess is generated from the circled region in Figure 4.3(b), and the resultant transfer in Figure 4.4 has a maneuver magnitude of 0.3229 $[nd] = 0.3307\ km/s$ at the manifold intersection and a time-of-flight of 20.7587 $[nd] = 90.2669\ days$. The plane change required to travel from the 9:2 NRHO to this 3:2 planar resonant orbit as well as the geometry of the stable manifolds present challenges for transfer design. However, since this mapping strategy works for this difficult example, it can successfully locate low cost transfers for most scenarios given appropriate intermediate arcs.

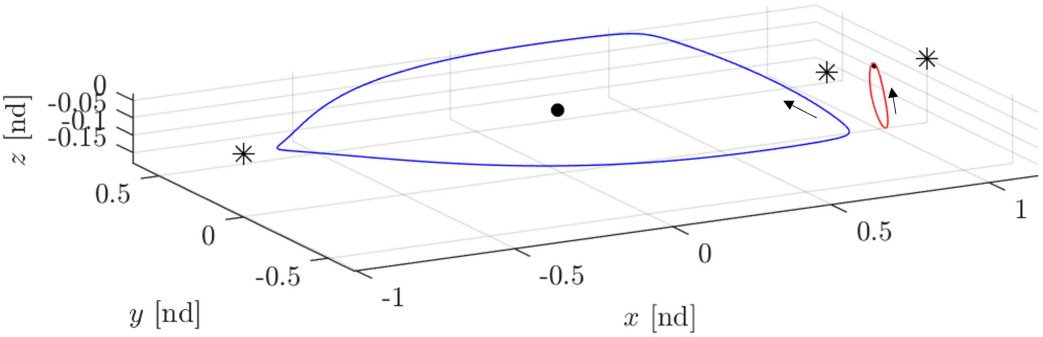

Figure 4.2. 9:2 synodic resonant NRHO and the selected 3:2 planar resonant orbit with $C = 3.0468$.

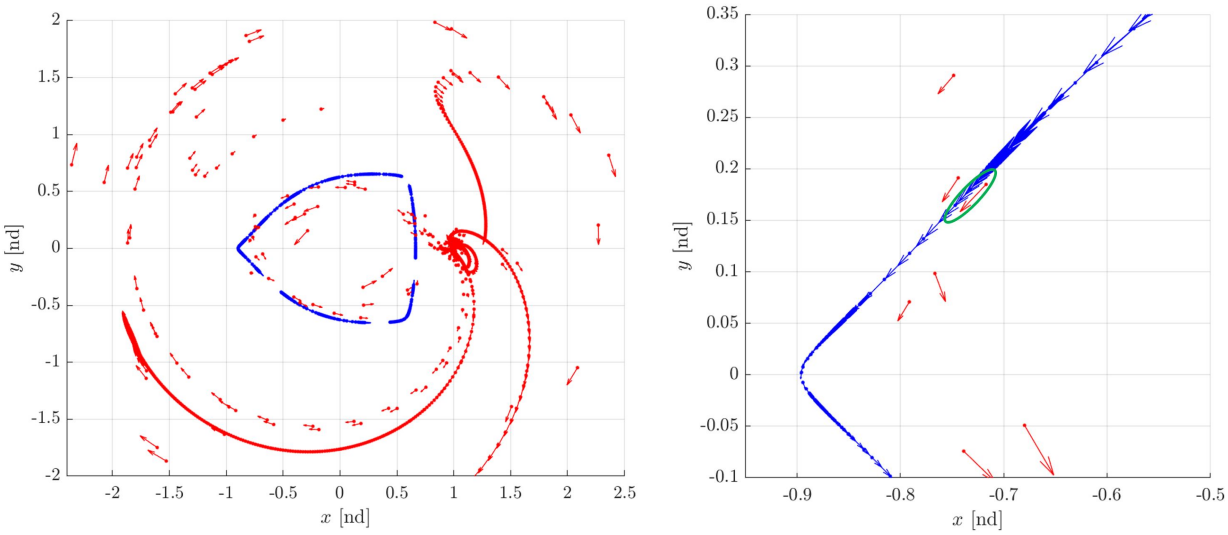

(a) Poincaré map (b) Zoomed-in Poincaré map

Figure 4.3. Glyph Poincaré map for 9:2 NRHO unstable manifold trajectories and 3:2 planar resonant orbit stable manifold trajectories with $C = 3.0468$. Glyphs indicate the magnitude and orientation of the in-plane velocity.

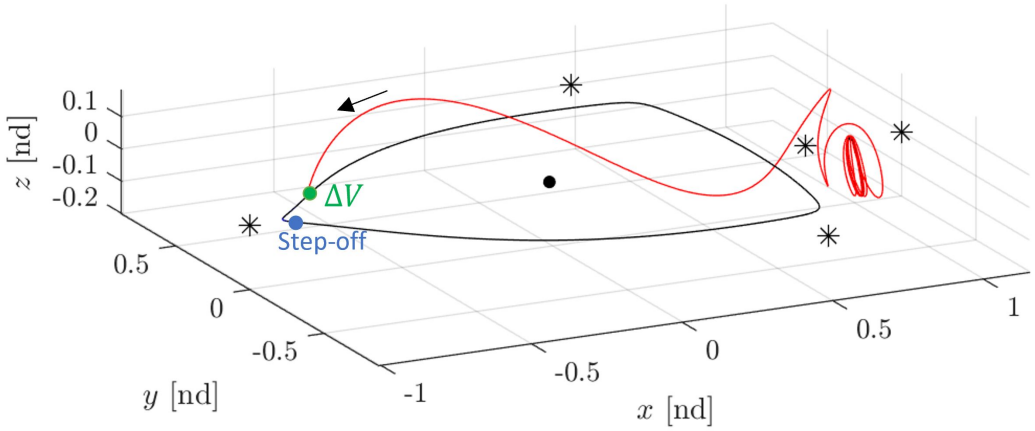

Figure 4.4. Transfer from the 9:2 synodic resonant NRHO to a 3:2 planar resonant orbit with $C = 3.0468$ designed using unstable and stable manifolds.

Transfer to a 3:2 Planar Resonant Orbit: Unstable Manifold Direct to Orbit

To reduce time-of-flight, a singular intermediate arc is used to directly connect to the final orbit instead of leveraging the stable manifolds. Recall that time-of-flight is defined as time along any intermediate segments and does not include time along the initial or final orbits. For convenience, let the intermediate arc be on the unstable manifold surface of the 9:2 NRHO which is propagated to record crossings of $\Sigma : z = 0$. The hyperplane intersections are shown in the map in Figure 4.5 along with the 3:2 planar resonant orbit defined by $C = 3.0468$ to determine if any unstable manifold trajectories pass through the 3:2 planar orbit. The velocity at each point along the 3:2 planar resonant orbit is assumed tangent to the orbit in the direction indicated by the black arrow. The state associated with the circled glyph in Figure 4.5(b) along with the closest state on the destination orbit is used to construct the spatial transfer initial guess. Note that the selected unstable manifold crossing in Figure 4.5(b) is the same as the one in Figure 4.3(b). Instead of using a maneuver to jump onto the stable manifold and then approach the orbit, a ΔV is now used to directly insert into the orbit at that location. The converged transfer using only an unstable manifold trajectory in Figure 4.6 has a maneuver magnitude of $0.3215\ [nd] = 0.3293\ km/s$ and a time-of-flight of $19.3812\ [nd] = 84.2768\ days$. Exploiting map properties and selecting an advantageous hyperplane has resulted in a transfer with a similar geometry but with a shorter transfer time by about six days.

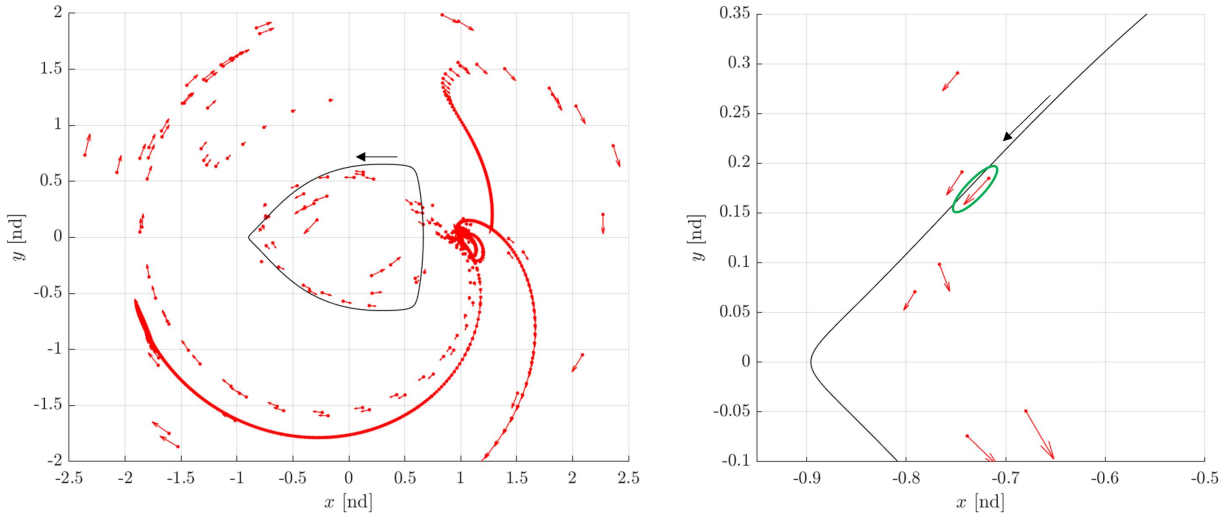

(a) Poincaré map

(b) Zoomed-in Poincaré map

Figure 4.5. Glyph Poincaré map for 9:2 NRHO unstable manifold trajectories overlaid with a 3:2 planar resonant orbit with $C = 3.0468$. Glyphs indicate the magnitude and orientation of the in-plane velocity.

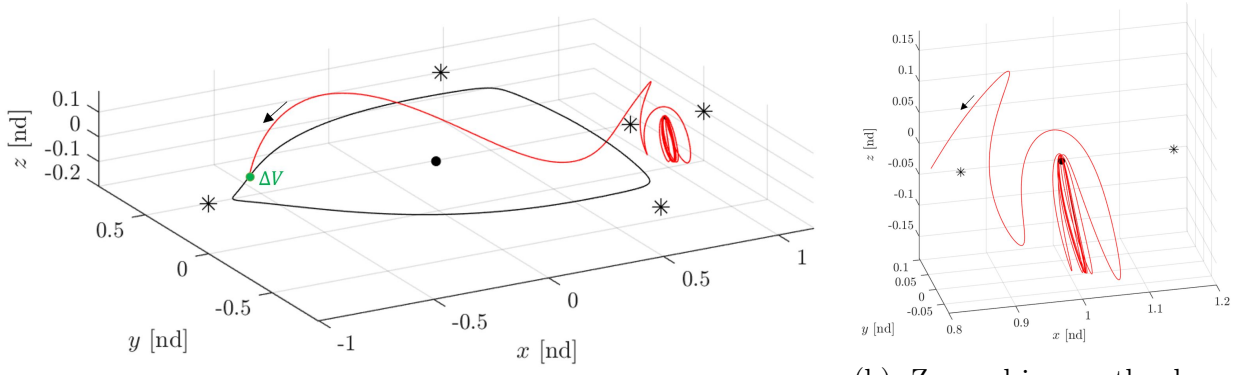

(a) Converged transfer

(b) Zoomed-in on the lunar vicinity

Figure 4.6. Transfer from the 9:2 synodic resonant NRHO to a 3:2 planar resonant orbit with $C = 3.0468$ designed using unstable manifolds.

4.3.2 Distinct Jacobi Constant Transfers

In the previous chapter, a transfer was designed between two planar orbits with different Jacobi constant values, and three state variables were required for the Poincaré map as opposed to two state variables when the orbits possessed the same value of C. The same concept applies to spatial transfers. As demonstrated in the previous section, a spatial transfer between orbits with the same Jacobi constant value requires a map with four state variables, but a transfer between two orbits with distinct Jacobi constant values requires a map with five state variables to visualize the full six-dimensional state. To maintain the relative ease of comparing values on a planar map, this fifth variable is portrayed through color. For example, if the hyperplane is defined at $z = 0$, the point is located at (x, y), and the glyph represents $(\dot{x}, \dot{y})$, then the color of the scatter point will indicate the magnitude and direction of $\dot{z}$. The glyphs are still colored red or blue to indicate the corresponding trajectory lies on an unstable or stable manifold surface, respectively.

Transfer to an L_2 Vertical Orbit: Unstable Manifold to Stable Manifold

An L_2 vertical orbit with $C = 2.90123$ and maximum out-of-plane excursion of about 121,150 km is leveraged to demonstrate a transfer from the 9:2 NRHO to a large out-of-plane orbit which is entirely in the lunar vicinity. The difference in Jacobi constant value between these two orbits shown in Figure 4.7 is $\Delta C = 0.1456$. The chosen vertical orbit only intersects the $\hat{x}$-$\hat{y}$ plane at one point, and, thus, its manifolds intersect the plane close to this point until they depart the vicinity. To encourage more intersections and examine different motion, the hyperplane is defined at $x = x_2$, i.e., the x-coordinate of the L_2 Lagrange point.

After propagating the unstable manifolds of the 9:2 NRHO and the stable manifolds of the selected L_2 vertical orbit, intersections of Σ are plotted in Figure 4.8. Figure 4.9 examines two locations of manifold intersections near the Moon. Clearly, the velocity directions do not align for the three crossings of the stable and unstable manifold trajectories in Figure 4.9(a). Figure 4.9(b) also has three crossings, and only the circled region possesses nearly aligned glyphs. Additionally, at this location, the sign for $\dot{z}$, indicated by the color, is the same for both the unstable and stable manifold trajectories as desired. An initial guess is

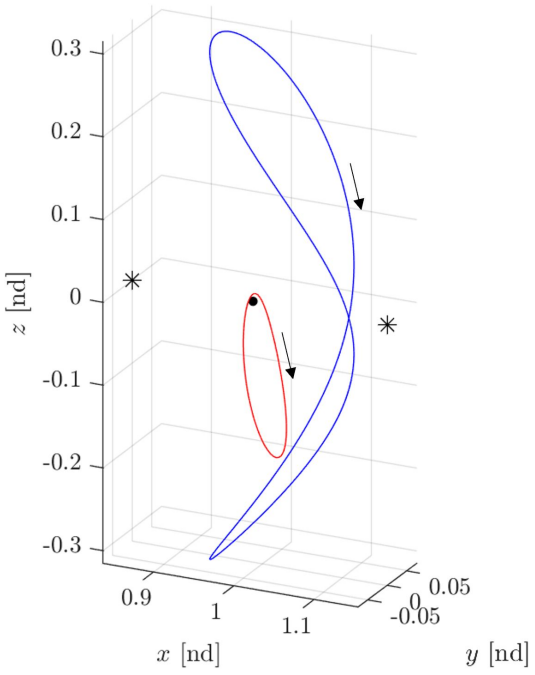

Figure 4.7. 9:2 synodic resonant NRHO with the selected L_2 vertical orbit with $C = 2.90123$.

constructed from states within the green circle, and the transfer targeter outlined in Section 3.2 is applied. Allowing an impulsive maneuver at the manifold intersection to overcome the differences in Jacobi constant value and direction, a converged spatial transfer shown in Figure 4.10 is obtained with a maneuver magnitude of 0.1982 km/s and a time-of-flight of 144.0582 $days$.

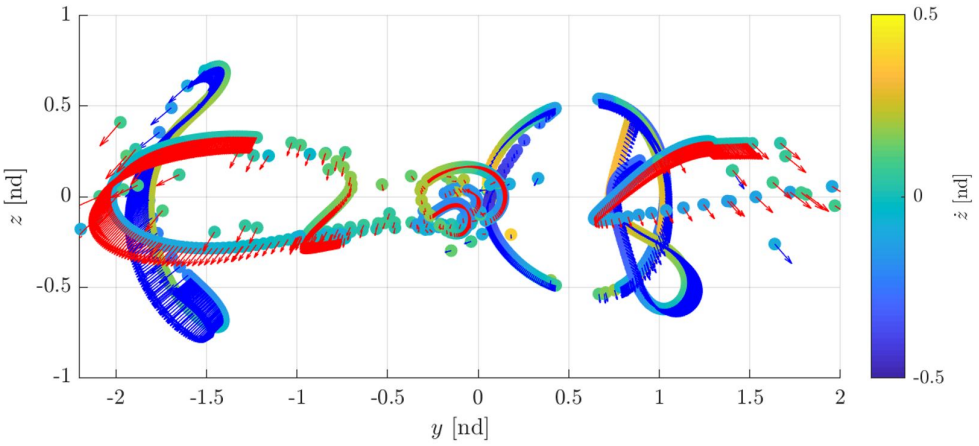

Figure 4.8. Glyph Poincaré map for 9:2 NRHO unstable manifold trajectories and L_2 vertical stable manifold trajectories. Glyphs indicate the magnitude and orientation of the in-plane velocity.

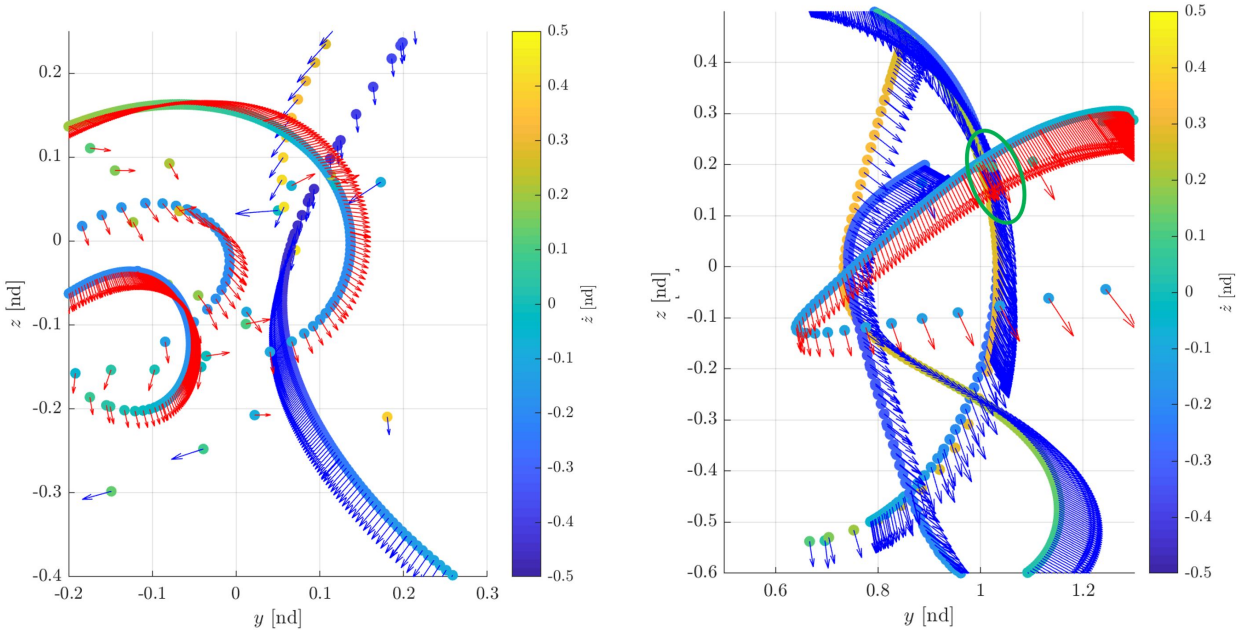

(a) Left (b) Right

Figure 4.9. Zoomed-in glyph Poincaré map for 9:2 NRHO unstable manifold trajectories and L_2 vertical stable manifold trajectories. Glyphs indicate the magnitude and orientation of the in-plane velocity.

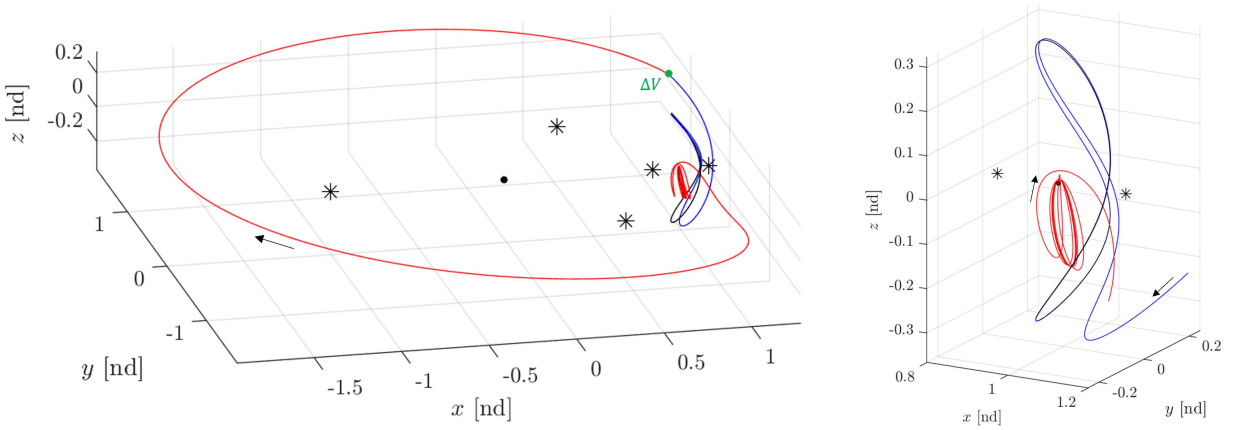

(a) Converged transfer

(b) Zoomed-in on lunar vicinity

Figure 4.10. Transfer from the 9:2 synodic resonant NRHO to an L_2 vertical orbit with $C = 2.90123$ designed using unstable and stable manifold trajectories.

Transfer to an L_2 Vertical Orbit: Impulsive Departure to a Stable Manifold

To reduce time-of-flight, tangential maneuvers are applied at fixed points along the 9:2 NRHO, as outlined in section 4.2. These maneuver magnitudes are plotted in Figure 4.11 where apolune occurs at the initial and final time. Additionally, note that the minimum maneuver magnitude occurs at perilune. Tangential maneuvers are used to seed an ideal initial guess, but a tangential ΔV constraint is not enforced in the differential corrections scheme. The resultant arcs, which no longer remain in the vicinity of the orbit for several revolutions like the unstable manifolds, are then propagated for 4 $[nd]$ and intersections with $\Sigma : x = x_2$ are recorded. The stable manifolds of the L_2 vertical orbit are also propagated and intersections with Σ are recorded. The resulting Poincaré map in Figure 4.12 allows for the visualization of potential transfers utilizing a tangential maneuver to depart the 9:2 NRHO, depicted in red, and a stable manifold trajectory to approach the L_2 vertical orbit, depicted in blue. A closer look at the map in Figure 4.13 reveals the location where states from the tangential departure arcs and stable manifold trajectories are the closest. An initial guess from the circled region is corrected to obtain the converged transfer in Figure 4.14 with a maneuver of 0.1505 $[nd] = 0.1541\ km/s$ to depart the 9:2 NRHO and a ΔV of 0.3254 $[nd] = 0.3333\ km/s$ at the intermediate arc connection. Thus, the total ΔV is 0.4759 $[nd] = 0.4874\ km/s$ with a time-of-flight of 21.7821 $[nd] = 94.7168\ days$.

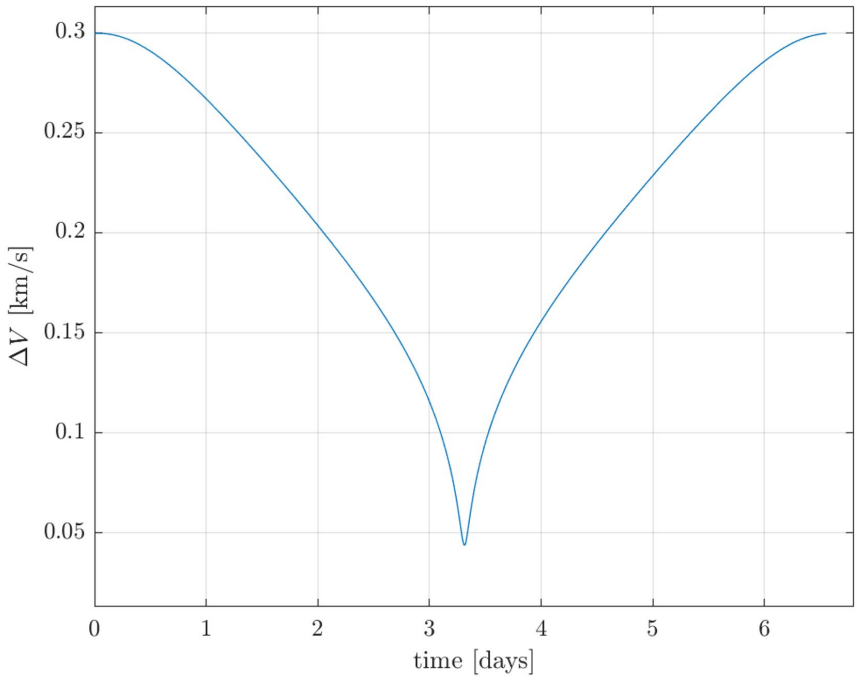

Figure 4.11. Theoretical minimum ΔV to change the Jacobi constant along the 9:2 NRHO to that of the L_2 vertical orbit. Initial and final time are at apolune.

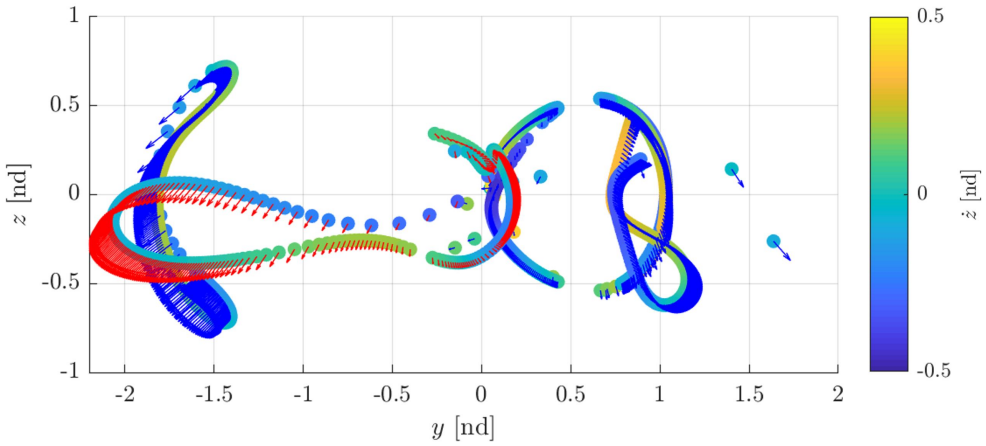

Figure 4.12. Glyph Poincaré map for 9:2 NRHO tangential departure maneuvers and L_2 vertical stable manifold trajectories. Glyphs indicate the magnitude and orientation of the in-plane velocity.

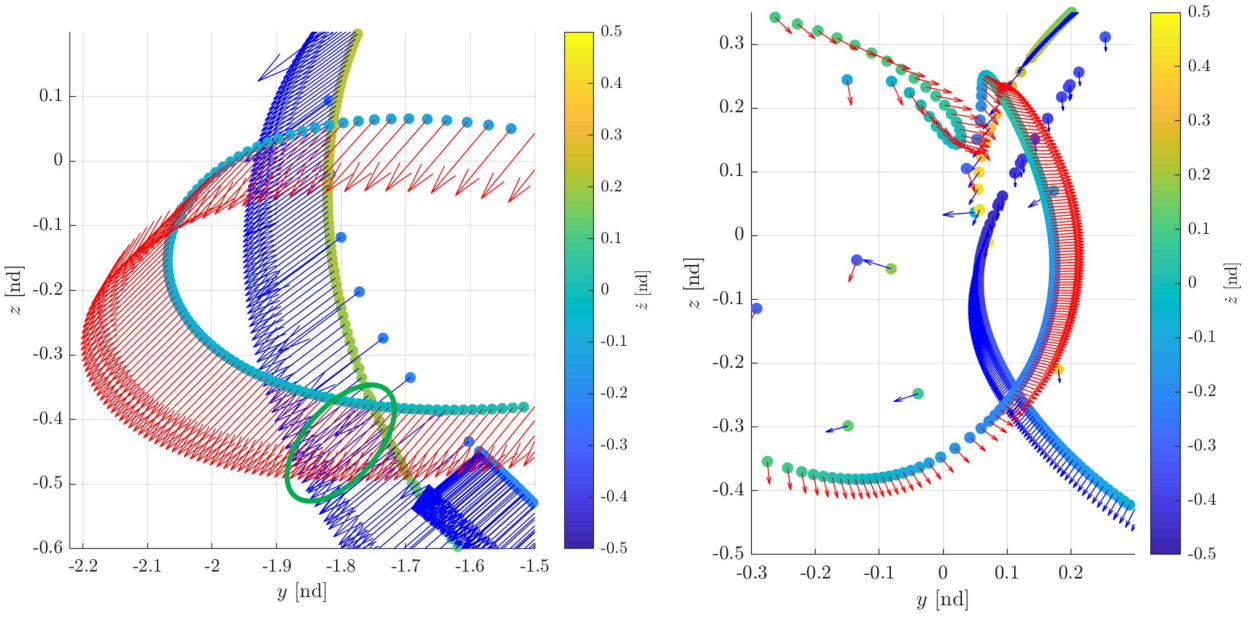

(a) Left (b) Right

Figure 4.13. Zoomed-in glyph Poincaré map for 9:2 NRHO tangential departure maneuvers and L_2 vertical stable manifold trajectories. Glyphs indicate the magnitude and orientation of the in-plane velocity.

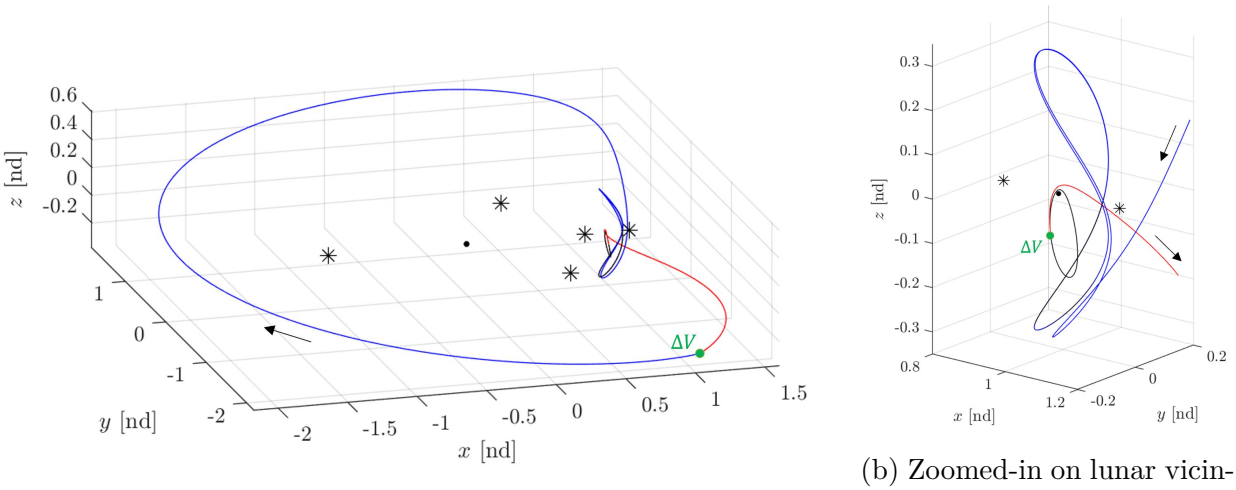

(a) Converged transfer

(b) Zoomed-in on lunar vicinity

Figure 4.14. Transfer from the 9:2 synodic resonant NRHO to an L_2 vertical orbit with $C = 2.90123$ designed using tangential orbit departures and stable manifold trajectories.

4.4 Maps with Non-State Variables

Traditionally, Poincaré maps visualize a subset of state variables at intersections of Σ, regardless of the hyperplane definition. Visualizing velocity components on maps are useful when minimizing maneuver cost. However, what if maneuver cost is not the primary mission constraint? For example, time-of-flight constraints are important for human spaceflight. Additionally, consider the initial and final orbits. It is known that NASA plans to use the 9:2 synodic resonant NRHO as the orbit for the Gateway, so the initial orbit for spatial transfers in this investigation has been defined to be the 9:2 NRHO [5]. The destination orbits for transfers thus far have been arbitrarily selected to demonstrate potential transfer scenarios and mapping applications. Without generating multiple maps for each different final orbit option, the strategies investigated up to this point do not indicate whether a chosen destination orbit provides the best transfer options compared to nearby orbits. In this case, it is advantageous to visualize multiple orbits on one map. This section investigates the benefits of constructing Poincaré maps with non-state variables and untraditional methods for use in trajectory design.

4.4.1 Time-of-Flight

Applying a maneuver to depart the 9:2 NRHO rather than leveraging the unstable manifolds reduces the time-of-flight at the price of ΔV. It is possible to achieve a lower time-of-flight while still utilizing manifolds to reduce maneuver cost. Figure 4.15(a) is a three-dimensional map of the remaining position components and time-of-flight (TOF) for $\Sigma : x = x_2$. The time-of-flight associated with an intersection of the hyperplane is the time spent on the corresponding manifold trajectory from the orbit step off until the hyperplane is reached. Once an unstable and stable manifold trajectory are selected for an initial guess, adding their associated TOFs gives the transfer time-of-flight. To improve convergence properties, a near intersection in position space is desired, so the Poincaré map is constructed with the two remaining position components. A zoomed-in view of the map in Figure 4.15(b) examines the lowest TOFs near the Moon. The projection in Figure 4.15(c) reveals that there are only three intersections of stable and unstable manifold trajectories

in position space. The intersection with the lowest total TOF is circled in green. The converged transfer from the two closest points in the circled region is shown in Figure 4.16 with a maneuver magnitude of 0.3632 $[nd] = 0.3719\ km/s$ at the manifold intersection and a time-of-flight of 23.8115 $[nd] = 103.5415\ days$. Thus, compared to the transfer leveraging impulsive departure maneuvers, the ΔV has been decreased by approximately 0.1 km/s with only the addition of about 9 $days$.

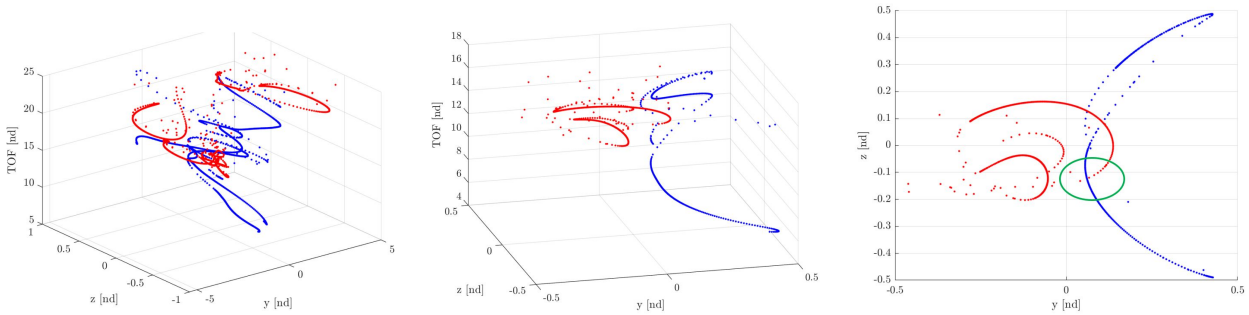

(a) y vs z vs TOF (b) y vs z vs TOF zoomed-in (c) y vs z projection

Figure 4.15. Three-dimensional Poincaré map featuring TOF for 9:2 NRHO unstable manifold trajectories and L_2 vertical stable manifold trajectories using $\Sigma : x = x_2$.

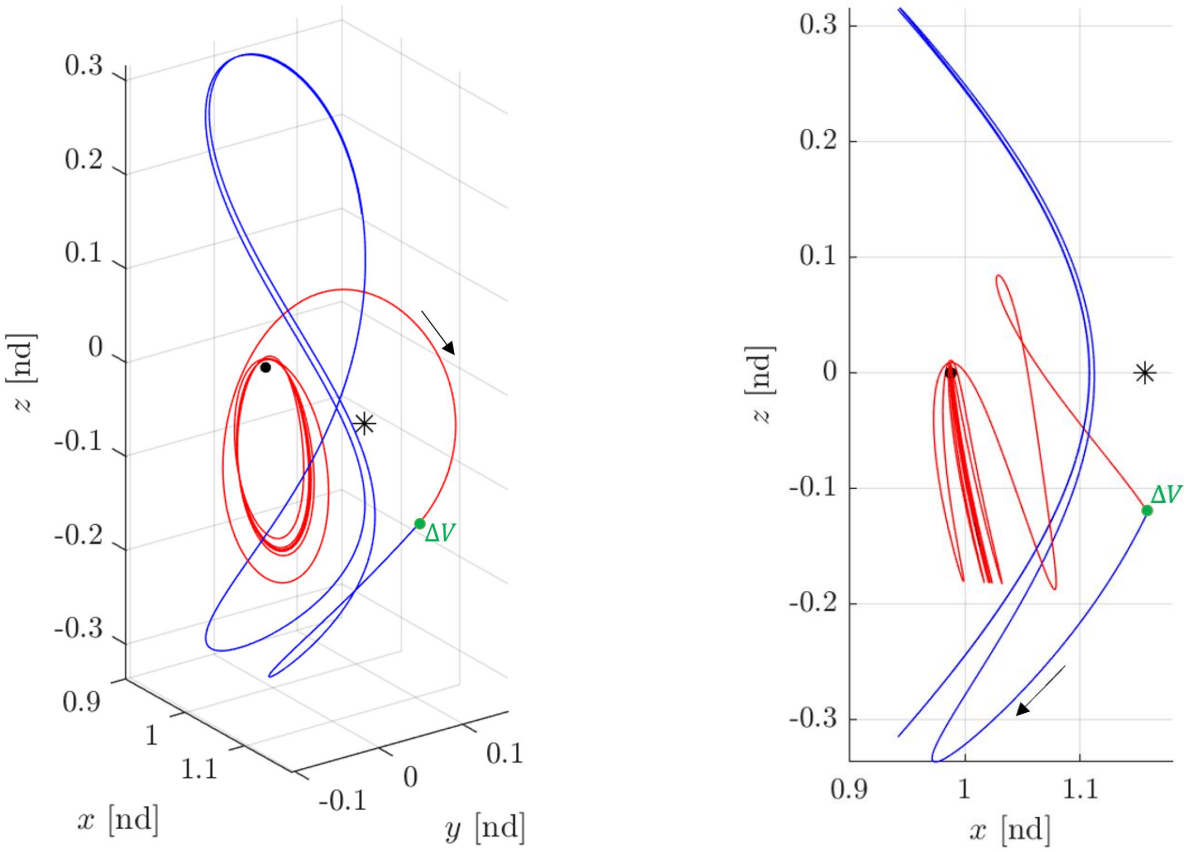

(a) Three-dimensional view

(b) x-z projection

Figure 4.16. Transfer from the 9:2 synodic resonant NRHO to an L_2 vertical orbit using a three-dimensional map featuring time-of-flight.

4.4.2 Angular Momentum

The angular momentum vector for a two-body orbit defines the orbital plane, but, for the CR3BP, it identifies the instantaneous plane of motion. Expanding this concept, if two arcs are continuous in position and velocity, then their angular momentum vectors are equivalent. This idea can be modified for arcs that are only continuous in position. Recall the definition of the theoretical minimum ΔV in Equation (3.5). To derive the theoretical minimum maneuver cost, it was assumed that the arcs meet in position space, i.e., $U_1^* = U_2^*$, and from Equation (3.4) it is clear that the minimum occurs when the arcs are tangent. Further, when two arcs meet in position space, they are tangent if their angular momentum vectors are parallel.

A set of Poincaré maps comprised of a combination of position states and angular momentum components reveals arcs that meet in position space and possess nearly parallel momentum vectors. Recall that the arcs are tangent if they meet these conditions. Thus, the angular momentum vector is calculated for each hyperplane crossing. The equation for angular momentum

$$\bar{H} = \bar{r} \times m\bar{v} \tag{4.2}$$

is the cross product of the position vector with the linear momentum vector. In the CR3BP, the mass of P_3 is assumed much less than the masses of the primaries, i.e., $m_3 << m_1, m_2$, but this does not imply that $m_3 = 0$. To utilize the angular momentum without assuming a mass for P_3, the specific angular momentum is used,

$$\bar{h} = \bar{r} \times \bar{v} \tag{4.3}$$

which is the cross product between the position vector and the specific linear momentum, or velocity vector. Let the components of the angular momentum be defined as $\bar{h} = h_x\hat{x} + h_y\hat{y} + h_z\hat{z}$. Clearly, an increase in $\bar{r}$ or $\bar{v}$ results in an increase in angular momentum per unit mass. Note that the CR3BP position and velocity vectors have an origin at the barycenter and rotating coordinates that are expressed in the Earth-Moon rotating frame.

Consider again an L_1 Lyapunov orbit and an L_2 Lyapunov orbit both with $C = 3.15$. The corresponding unstable and stable manifold trajectories are propagated towards the Moon and crossings of $\Sigma : x = x_2$ are recorded. The y vs $\dot{y}$ maps used in the previous chapter to construct Lyapunov transfers are augmented with $h_{xy} = \sqrt{h_x^2 + h_y^2}$ and h_z in Figure 4.17. As evident in Figures 4.17, all components of the angular momentum vector are approximately zero at the hyperplane because $\bar{r}$ and $\bar{v}$ are almost parallel. Note that the manifolds pass close below the Moon so that the x-coordinate dominates and the position vector relative to the Earth-Moon barycenter is almost along the $\hat{x}$-axis. Because the L_1 and L_2 Lyapunov families are planar, the angular momentum vector calculated at any point along these orbits or their manifolds only has a z-component.

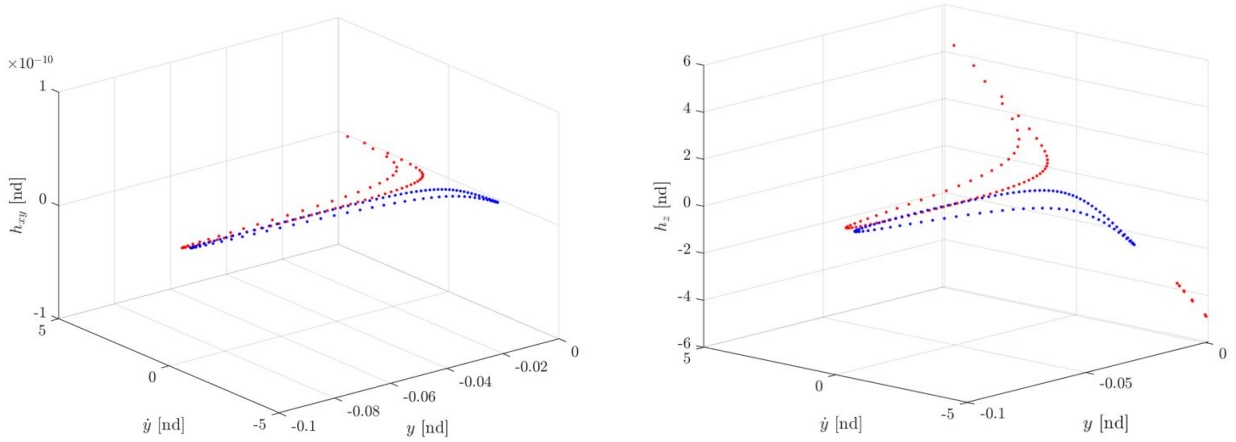

(a) y vs $\dot{y}$ vs h_{xy}

(b) y vs $\dot{y}$ vs h_z

Figure 4.17. Three-dimensional Poincaré maps featuring angular momentum for L_1 unstable manifold trajectories and L_2 Lyapunov stable manifold trajectories using $\Sigma : x = 1 - \mu$.

The same method is applied using the 9:2 NRHO unstable manifolds and the L_2 vertical orbit stable manifolds. Figure 4.18 presents three maps with $|\bar{h}|$, h_{xy}, and h_z on the third axis. Consider the manifold intersection inside the gold circle in Figure 4.19 and the resulting initial guess in Figure 4.20. At this location on the map, the out-of-plane angular momentum component, i.e., h_z, is larger than the other angular momentum components. As discussed for the L_1 to L_2 Lyapunov orbit transfer example, when h_z dominates, the motion is nearly parallel to the $\hat{x}$-$\hat{y}$ plane. This is clearly seen at the manifold intersection in Figure 4.20. Next, an initial guess is selected from the green circled region in Figure 4.19 where the manifold trajectories possess smaller values of h_z. The converged transfer from the 9:2 NRHO to the chosen L_2 vertical orbit is illustrated in Figure 4.21. As expected, both manifold trajectories have a sloped instantaneous plane of motion at their intersection. Additionally, at this location there is a maneuver of magnitude 0.6218 $[nd]$ = 0.6368 km/s and the total time-of-flight along the manifold trajectories is 42.5082 $[nd]$ = 184.8420 $days$. The theoretical minimum maneuver at this intersection point is 0.1212 $[nd]$ = 0.1241 km/s. While these map provides insight into the motion, clearly visualizing the angular momentum components on separate maps does not produce the lowest cost transfers.

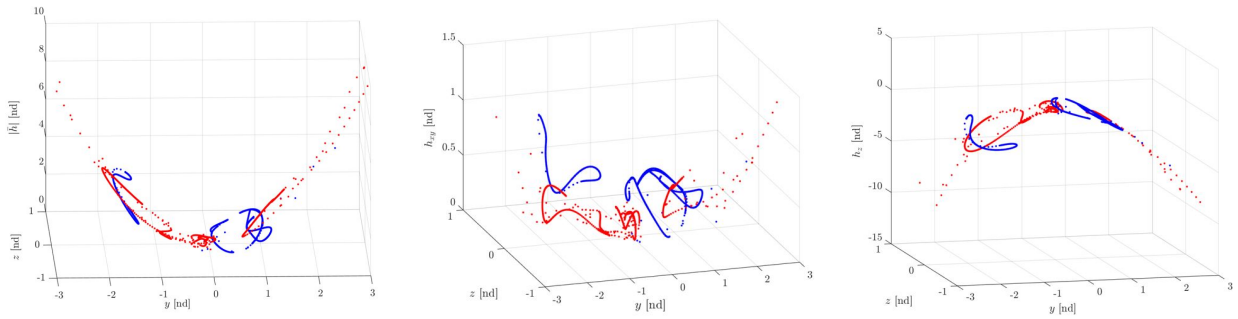

(a) y vs z vs $|\bar{h}|$ (b) y vs z vs h_{xy} (c) y vs z vs h_z

Figure 4.18. Three-dimensional Poincaré map featuring angular momentum for 9:2 NRHO unstable manifold trajectories and L_2 vertical stable manifold trajectories using $\Sigma : x = x_2$.

To visualize all three angular momentum components on one map, glyphs and color are implemented. The axes of the map represent the remaining position states after the physical hyperplane is defined. For the 9:2 NRHO to L_2 vertical orbit transfer example, the Poincaré map, given in Figure 4.22, has axes y and z. The glyphs represent the direction and magnitude of the in-plane angular momentum components, i.e., h_x and h_y, and the color portrays the out-of-plane angular momentum component, i.e., h_z. This map also has the advantage of a planar representation that allows for easier comparison of states and location of intersections. A visual inspection of the map identifies the circled region in Figure 4.22(b) as providing a good initial guess. Allowing for a maneuver where the manifolds meet, the transfer targeter outlined in Section 3.2 converges on the trajectory in Figure 4.23 with $\Delta V = 0.4214\ [nd] = 0.4316\ km/s$ at the manifold intersection and a time-of-flight of $47.6378\ [nd] = 207.1471\ days$. The theoretical minimum maneuver where the manifold trajectories intersect is $0.1203\ [nd] = 0.1232\ km/s$. The calculated and theoretical values are not equal in part due to map selections that are not exactly equivalent in position with angular momentum vectors that are not precisely parallel. However, the calculated maneuver, and thus the difference between the calculated and theoretical minimum ΔV, has been decreased by approximately $0.2\ km/s$ compared to the transfer in Figure 4.21. This mapping strategy that employs glyphs and color to depict the angular momentum presents another method by which to construct transfers with low maneuver cost.

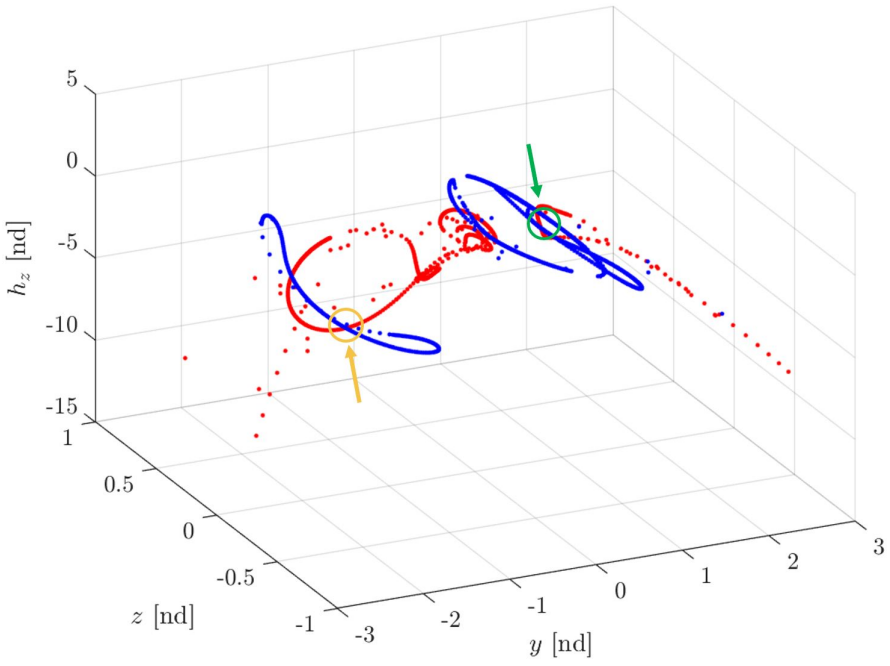

Figure 4.19. Selected points on three-dimensional Poincaré maps featuring angular momentum using $\Sigma : x = x_2$.

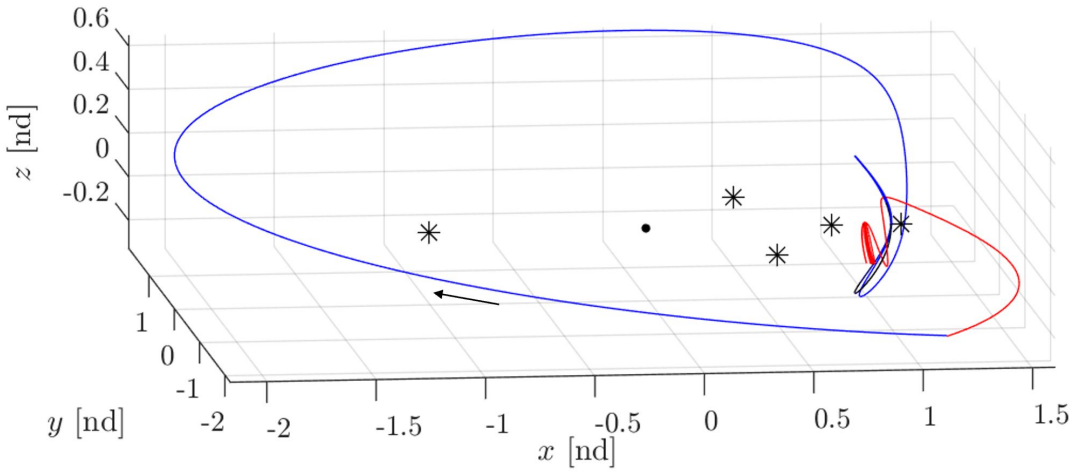

Figure 4.20. Initial guess for a transfer with a dominating z-component at the manifold intersection.

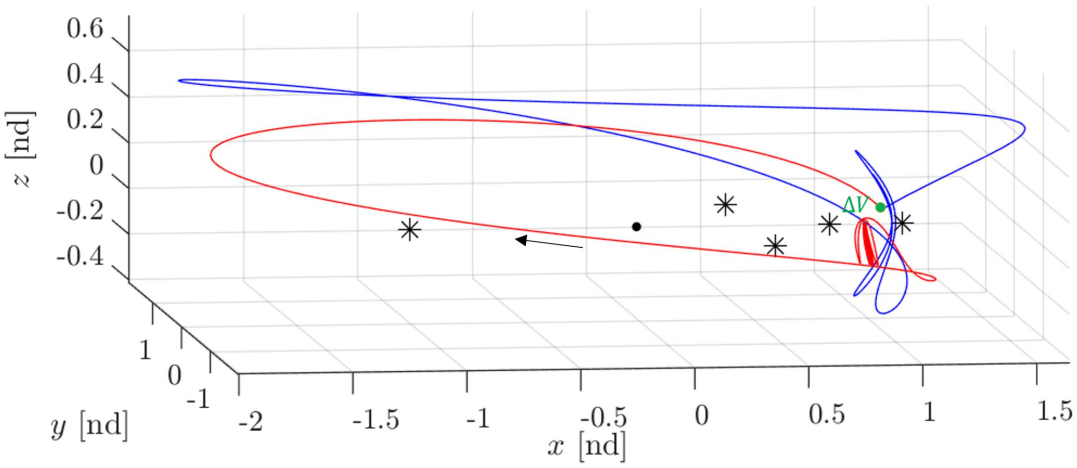

Figure 4.21. Transfer from the 9:2 synodic resonant NRHO to an L_2 vertical orbit using a three-dimensional map featuring the angular momentum.

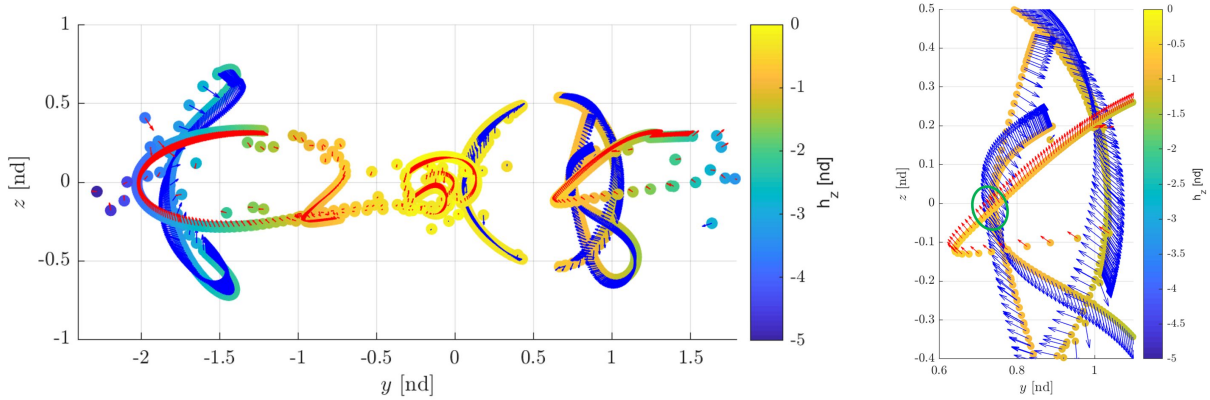

(a) y vs z vs $|\bar{h}|$ (b) y vs z vs h_{xy}

Figure 4.22. Poincaré map featuring angular momentum orientation for 9:2 NRHO unstable manifold trajectories and L_2 vertical stable manifold trajectories using $\Sigma : x = x_2$.

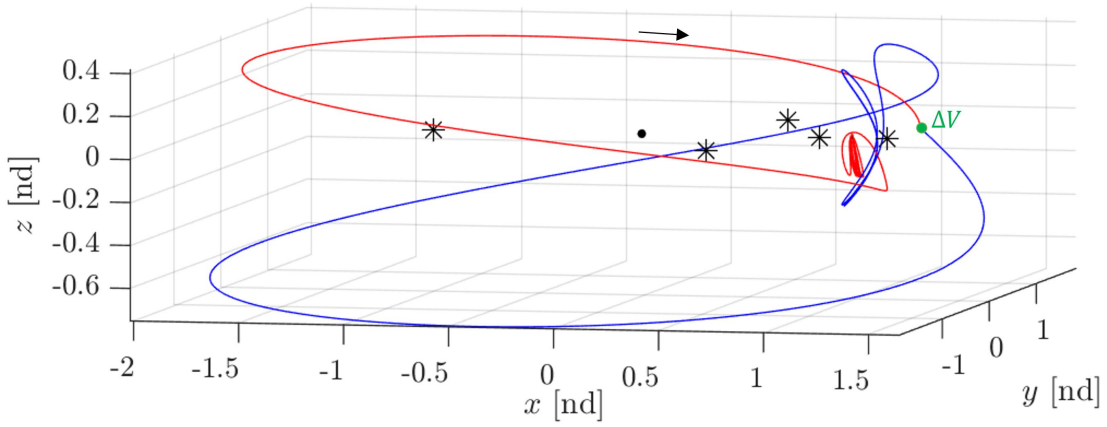

Figure 4.23. Transfer from the 9:2 synodic resonant NRHO to the L_2 vertical orbit obtained using a map with glyphs and color representing the angular momentum components.

4.4.3 Whole families

This investigation thus far has focused on using maps to meet various mission constraints for specified initial and final orbits. However, consider a scenario where it is desired to leave from the L_1 region and arrive at the L_2 region. A specific orbit is not required, but a certain geometry is desired. For example, consider a subset of the L_1 and L_2 Lyapunov periodic orbit families in Figure 4.24 that possess Jacobi constant values between 3.02 and 3.16. For the given range of C, the members of each family possess similar geometries. Figure 4.25 illustrates the result of propagating the unstable and stable manifold trajectories of a subset of these orbits towards the Moon. Clearly, several transfer options are present using manifolds from only four L_1 Lyapunov orbits and four L_2 Lyapunov orbits. Traditionally, to locate such transfers, a map is generated for each initial and final orbit pair. However, including C on a plot to distinguish between the several initial and final orbit allows for certain desirable, and previously unconsidered, characteristics or transfer geometries to be found by examining various family members simultaneously.

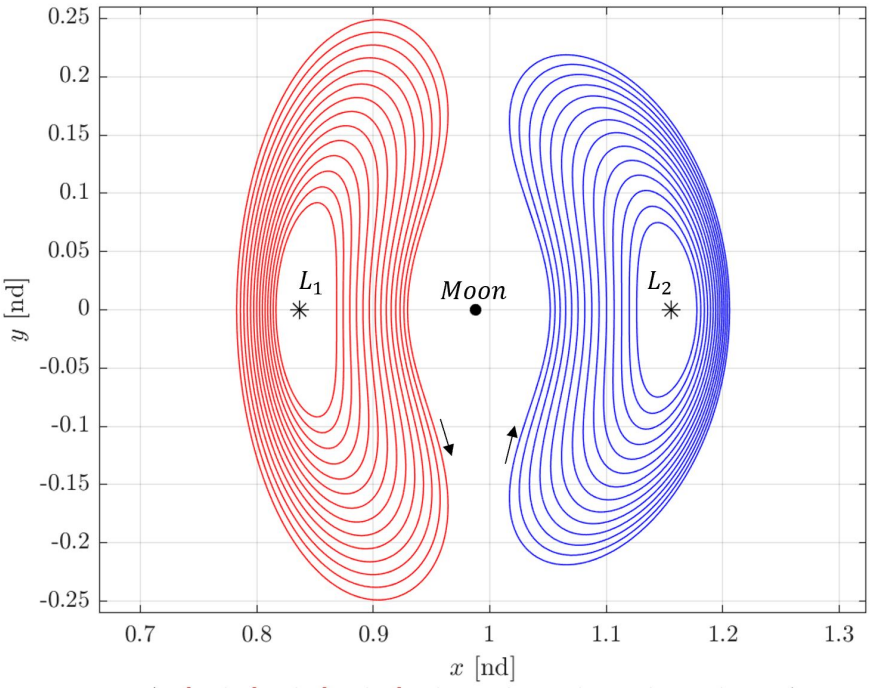

Figure 4.24. A subset of the L_1 and L_2 Lyapunov periodic orbit families.

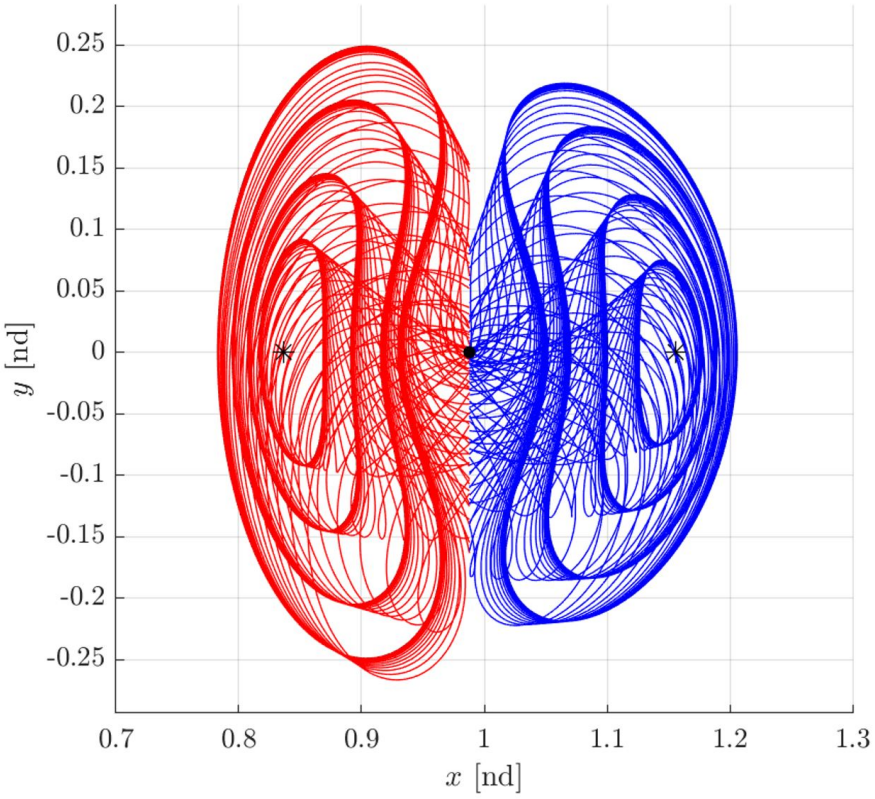

Figure 4.25. A subset of L_1 Lyapunov unstable manifold trajectories and L_2 Lyapunov stable manifold trajectories.

Recall that a map of y vs $\dot{y}$ provided a good initial guess for a transfer from an L_1 Lyapunov orbit to an L_2 Lyapunov orbit. In Figure 4.26, such a map is augmented with C on the third axis. Therefore, a slice of the map at a certain Jacobi constant value corresponds to the unstable manifold trajectories of the L_1 Lyapunov orbit and/or stable manifold trajectories of the L_2 Lyapunov orbit at that energy level. As emphasized in Figure 4.26(c), the manifolds at each value of C outline a smooth curve, and these curves evolve smoothly with Jacobi constant value. This map allows for the identification of manifold intersections in position space across family members. Any gap in Jacobi constant value gives an expected magnitude for ΔV since the position is fully defined.

Suppose the primary mission constraint is a lunar flyby distance or direction. Replacing $\dot{y}$ in the map in Figure 4.26 with TOF results in Figure 4.27. There are still clearly defined, smooth curves at each value of Jacobi constant. Examining the projection of y vs C in

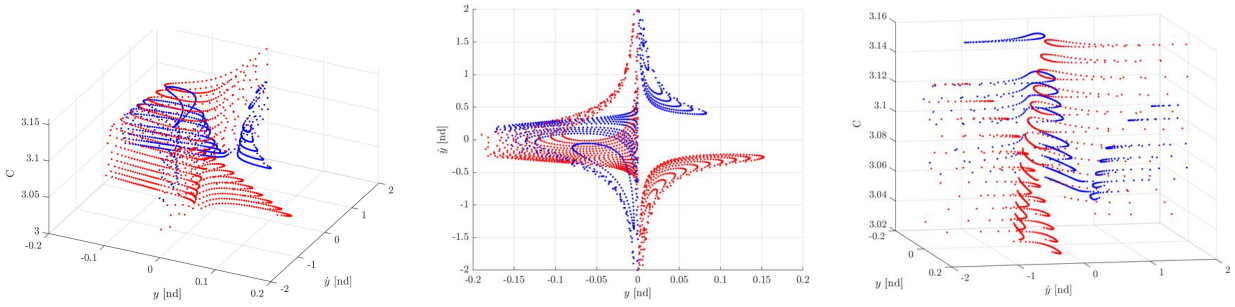

(a) y vs $\dot{y}$ vs C (b) y vs $\dot{y}$ (c) y vs $\dot{y}$ vs C side view

Figure 4.26. Three-dimensional Poincaré map for L_1 Lyapunov unstable manifold trajectories and L_2 Lyapunov stable manifold trajectories for several family members using $\Sigma : x = x_2$.

Figure 4.27(b), it is possible to pick an intersection distance from the Moon. Figure 4.28 identifies a location on the map and the converged transfer for manifolds that intersect relatively far from the Moon at approximately $y = -0.15$ $[nd]$. A maneuver magnitude of 0.4487 $[nd]$ = 0.4595 km/s overcomes the difference in Jacobi constant value of about $2.393 * 10^{-4}$ and velocity direction. Furthermore, one of the few transfers available above the Moon, according to the map for the specified orbits, with approximately $y = 0.025$ $[nd]$ is illustrated in Figure 4.29. A higher ΔV of 1.2747 $[nd]$ = 1.3055 km/s is needed to overcome the natural dynamics and gap in Jacobi constant value of 0.0012. The map in Figure 4.27(a) can also be used to identify low TOF transfer options available between various family members. As seen, including C on an axis to visualize transfer options for several initial and final orbits on one plot allows a wider view of the design space simultaneously.

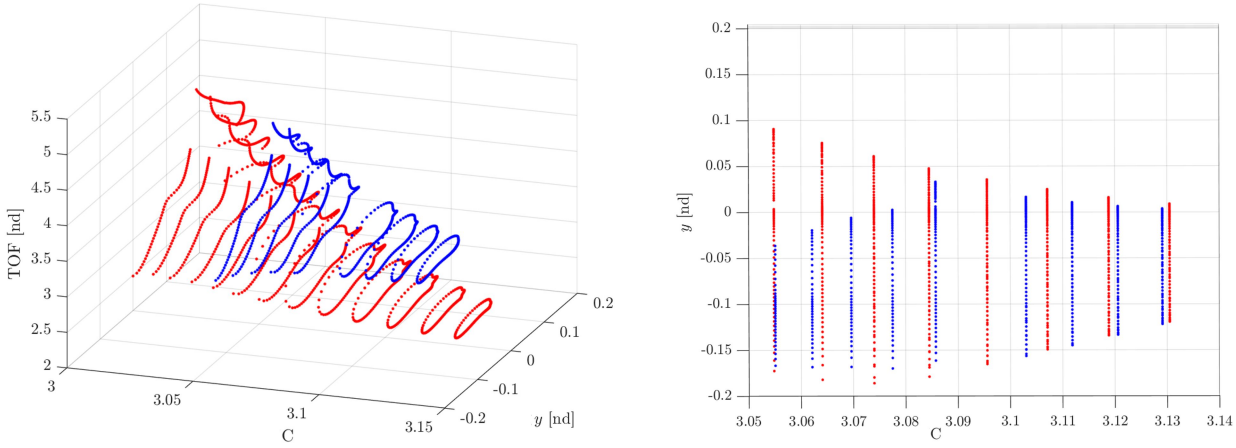

(a) C vs y vs TOF (b) C vs y

Figure 4.27. Three-dimensional Poincaré map featuring TOF for L_1 Lyapunov unstable manifold trajectories and L_2 Lyapunov stable manifold trajectories for several family members using $\Sigma : x = x_2$.

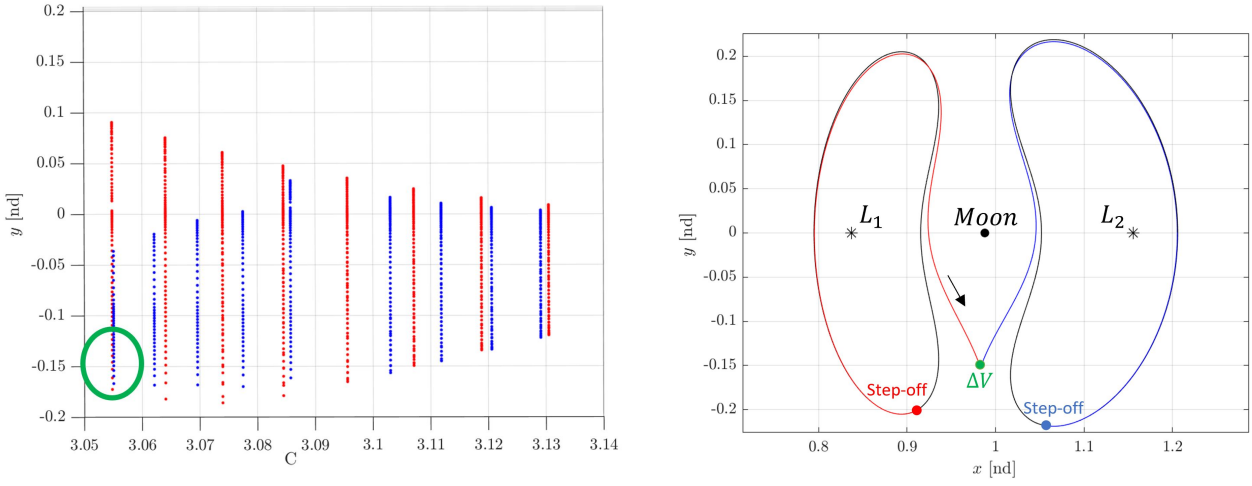

(a) C vs y (b) Converged transfer

Figure 4.28. Transfer from an L_1 Lyapunov orbit to an L_2 Lyapunov orbit with a prograde lunar flyby.

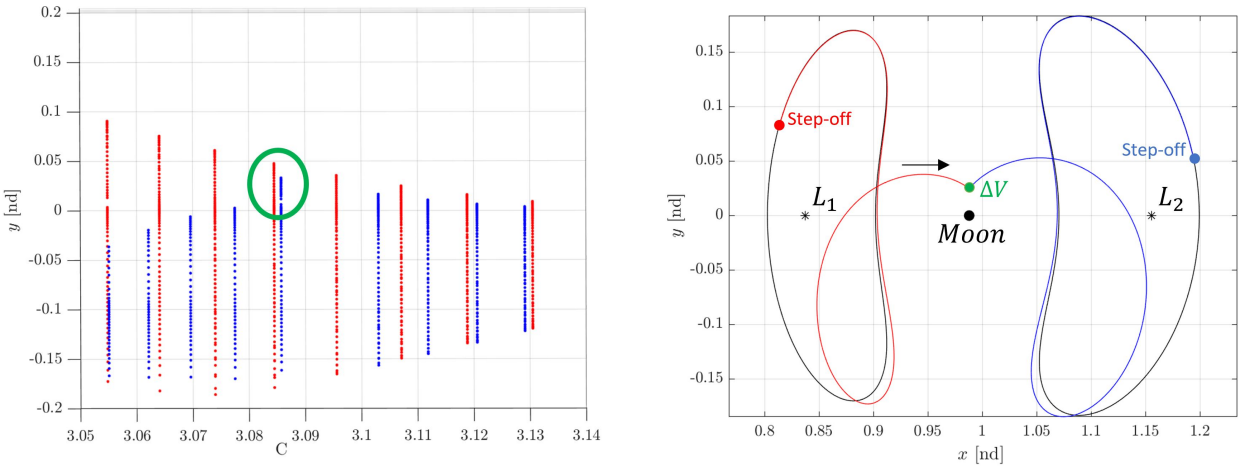

(a) C vs y

(b) Converged transfer

Figure 4.29. Transfer from an L_1 Lyapunov orbit to an L_2 Lyapunov orbit with a retrograde lunar flyby.

5. CONCLUDING REMARKS

5.1 Summary

As humanity continues to pursue its interests in the lunar vicinity and beyond, the need to develop a network of reliable transfers increases. These transfers need to be informed by various mission constraints to provide minimal time, low cost, and other options. The Circular Restricted Three-Body Problem (CR3BP) is utilized to construct and analyze transfers connecting multi-body orbits including the Gateway's 9:2 lunar synodic resonant NRHO [5]. Within the context of the CR3BP, this document introduces Poincaré mapping strategies and outlines the number of state variables needed to visualize an intersection of the full state for various problems, thus, revealing low cost transfers. Poincaré maps are first implemented in the planar problem to establish their use in low cost transfer design between two orbits with equivalent and distinct values of Jacobi constant. The need for higher-dimensional mapping techniques to visualize the full design space is established, and these glyph and glyph with color maps are employed to design multiple low cost transfers with the 9:2 NRHO as the initial orbit. Transfers from the 9:2 NRHO to a 3:2 planar resonant orbit present options for movement into a planar orbit as well as a tour of the Earth-Moon system. Next, transfers from the 9:2 NRHO to an L_2 vertical orbit provide examples of transfers to a large out-of-plane orbit that lies completely within the lunar vicinity. Both external transfers around the system as well as one existing completely within the lunar vicinity are demonstrated to travel from the 9:2 NRHO to the L_2 vertical orbit.

In addition to demonstrating the need and use of higher-dimensional maps to locate low cost spatial transfers, maps depicting time-of-flight, angular momentum, and Jacobi constant are presented and investigated. Rather than focusing on near-intersections of the full state, these maps search for position intersections that possess desirable characteristics. A map featuring time-of-flight easily uncovers a transfer from the 9:2 NRHO to an L_2 vertical orbit that remains completely in the lunar vicinity, reducing the transfer time as desired for crewed missions. To ensure low maneuver costs, a glyph map featuring angular momentum is used since arcs that meet in position space with parallel angular momentum vectors are tangent. This is frequently desirable because, as emphasized in the derivation of the

theoretical minimum ΔV, the lowest maneuver costs for a given location occur at tangential intersections. Finally, maps incorporating multiple family members are generated. Such a map is applicable when a certain geometry is desired but a particular orbit is not required. These maps visualize transfer options between several different orbits rather than creating a map for each initial and final orbit pair. Thus, a wider view of the design space is shown on one plot. Further, the ability to use non-state variables such as time-of-flight in these multiple orbit maps is discussed. There is a lack of research into non-state variable maps, so this investigation represents the beginning of this mapping method.

The transfers constructed with higher-dimensional maps in this investigation are relevant to real-world scenarios. The spatial transfers involving the 9:2 NRHO are specifically relevant to near-future Artemis missions, providing realistic low cost and low time-of-flight options. Additionally, these advanced mapping strategies are applicable to the visualization of any higher-dimensional data set regardless of field. In astrodynamics, these maps are advantageous for designing spatial transfers regardless of orbit and primary system.

5.2 Recommendations for Future Work

This investigation presents a selection of higher-dimensional maps; however, additional methods of visualizing greater than three-dimensions exist. Alternative methods of formulating higher-dimensional maps, such as three-dimensional glyphs, are available for evaluation. Such maps offer the ability to view five or more dimensions. If apse crossings are used to generate a map rather than defining a physical hyperplane location, the dimensionality is still reduced. However, an apse map to locate spatial transfers between two orbits with distinct Jacobi constant values requires a plot of six state variables to visualize the full state. A six-dimensional map representation is needed since an apse is not defined at a specific state variable but rather when a spacecraft's radial velocity relative to a primary is zero. Additionally, the inclusion of other non-state variables into maps will present new transfer opportunities and the ability to incorporate other mission constraints. For example, the inclusion of the closest lunar flyby distance will present options to observe the Moon, leverage the Moon's gravity, or insert into a low lunar orbit (LLO).

The inclusion of Jacobi constant value on a plot axis allowed a wider view of the design space simultaneously by including several initial and final orbits. Reducing the need to create and compare separate maps saves time and reveals options that might not otherwise be considered. This investigation provides a starting place for further research into these types of maps. By utilizing glyphs and other methods, it is possible to visualize full state intersections on these plots. Thus, low cost transfer options between various initial and final orbits will be revealed. Extending this methodology to consider other planar and spatial orbits provides further transfer options.

Another area for continued investigation is the incorporation of different intermediate arcs and orbits. This study utilized manifolds and resultant arcs from impulsive maneuvers for map creation, but this is not an inclusive list of available options. Arcs from periodic orbits represent one possibility that allows the incorporation of known, desired geometries into the transfer design process. Building upon the work in this investigation, enforcing tangential departure maneuvers from the 9:2 NRHO, or at other locations, in the differential correction scheme will result in maneuvers being equal to the theoretical minimum ΔV. Implementing this constraint potentially yields lower cost maneuvers. Additionally, as plans for the lunar vicinity evolve, the analysis of different destination orbits is important to reveal additional accessible pathways for future spacecraft.

REFERENCES

[1] J. B. West, "Historical aspects of the early soviet/russian manned space program," *Journal of Applied Physiology*, vol. 91, no. 4, pp. 1501–1511, 2001.

[2] ISS National Laboratory Center for the Advancement of Science in Space. (2022). "History and timeline of the iss," [Online]. Available: https://www.issnationallab.org/about/iss-timeline.

[3] M. Smith, D. Craig, N. Herrmann, E. Mahoney, J. Krezel, N. McIntyre, and K. Goodliff, "The artemis program: An overview of nasa's activities to return humans to the moon," in *2020 IEEE Aerospace Conference*, 2020, pp. 1–10.

[4] E. M. Z. Spreen, "Trajectory design and targeting for applications to the exploration program in cisllinar space," Ph.D. dissertation, Purdue University, 2021.

[5] D. E. Lee, "White paper: Gateway destination orbit model: A continuous 15 year nrho reference trajectory," National Aeronautics and Space Administration, NASA Johnson Space Center, Houston, TX, Technical Report Document ID: 20190030294, Aug. 2019.

[6] B. R. Goldstein, "Copernicus and the origin of his heliocentric system," *Journal for the History of Astronomy*, vol. 33, pp. 219–235, 2002.

[7] V. Szebehely, "The history and background of astrodynamics," in *Space and Humanity*, L. NAPOLITANO, Ed., Oxford: Pergamon, 1989, pp. 79–81, ISBN: 978-0-08-037877-0.

[8] J. T. Cushing, "Kepler's laws and universal gravitation in newton's principia," *American Journal of Physics*, vol. 50, no. 7, pp. 617–628, 1982.

[9] I. Newton, *The Principia: Mathematical Principles of Natural Philosophy*, trans. by I. B. Cohen and A. Whitman. University of California Press, 1999.

[10] J. Barrow-Green, "Poincaré and the three body problem, history of mathematics," *American Mathematical Society*, vol. 11, 1997.

[11] R. W. Farquhar, "The flight of isee-3/ice: Origins, mission history, and a legacy," *The Journal of the Astronautical Sciences*, vol. 49, no. 1, pp. 23–72, 2001.

[12] D. Folta and T. Sweetser, "ARTEMIS mission overview: From concept to operations," in *AAS/AIAA Astrodynamics Specialist Conference*, Paper No. AAS 11-510, Girdwood, Alaska, July, 2011.

[13] M. W. McElwain, L. D. Feinberg, R. A. Kimble, et al., "Status of the james webb space telescope mission," in *Space Telescopes and Instrumentation 2020: Optical, Infrared, and Millimeter Wave*, International Society for Optics and Photonics, vol. 11443, 2020, pp. 173–181.

[14] K. C. Howell, "Three-dimensional, periodic, 'halo' orbits," *Celestial Mechanics*, vol. 32, no. 1, pp. 52–70, 1984.

[15] K. C. Howell, "Families of orbits in the vicinity of the collinear libration points," *The Journal of the Astronautical Sciences*, vol. 49, pp. 107–125, 2001.

[16] W. S. Koon, M. W. Lo, J. E. Marsden, and S. D. Ross, "Heteroclinic connections between periodic orbits and resonance transitions in celestial mechanics," *Chaos: An Interdisciplinary Journal of Nonlinear Science*, vol. 10, no. 2, pp. 427–469, 2000.

[17] T. M. Vaquero Escribano, "Spacecraft transfer trajectory design exploiting resonant orbits in multi-body environments," Ph.D. dissertation, Purdue University, 2013.

[18] J. S. Parker, K. E. Davis, and G. H. Born, "Chaining periodic three-body orbits in the earth-moon system," *Acta Astronautica*, vol. 67, no. 5, pp. 623–638, 2010.

[19] M. Vaquero and K. C. Howell, "Design of transfer trajectories between resonant orbits in the earth-moon restricted problem," *Acta Astronautica*, vol. 94, pp. 302–317, 2014.

[20] C. D. Geisel, "Spacecraft orbit design in the circular restricted three-body problem using higher-dimensional poincaré maps," Ph.D. dissertation, Purdue University, 2013.

[21] P. A. Patsis and L. Zachilas, "Using color and rotation for visualizing four-dimensional poincaré cross-sections: With applications to the orbital behavior of a three-dimensional hamiltonian system," *International Journal of Bifurcations and Chaos*, vol. 4, pp. 1399–1424, 1994.

[22] M. J. Bolliger, "Cislunar mission design: Transfers linking near rectilinear halo orbits and the butterfly family," Purdue University, 2019.

[23] A. F. Haapala, "Trajectory design in the spatial circular restricted three-body problem exploiting higher-dimensional poincaré maps," Ph.D. dissertation, Purdue University, 2014.

[24] A. F. Haapala and K. C. Howell, "Representations of higher-dimensional poincaré maps with applications to spacecraft trajectory design," *Acta Astronautica*, vol. 96, pp. 23–41, 2014.

[25] D. C. Davis, "Multi-body trajectory design strategies based on periapsis poincaré maps," Ph.D. dissertation, Purdue University, 2011.

[26] S. Bonasera and N. Bosanac, "Unsupervised learning to aid visualization of higher-dimensional poincaré maps in multi-body trajectory design," 2020.

[27] S. Bonasera and N. Bosanac, "Applying data mining techniques to higher-dimensional poincaré maps in the circular restricted three-body problem," *Celestial Mechanics and Dynamical Astronomy*, vol. 133, no. 11, pp. 1–32, 2021.

[28] J. L. Lagrange, *Essai sur le problème des trois corps*. Prix de l'Acade'mie Royale des Sciences de Paris, 1772, vol. IX.

[29] S. Vutukuri, "Spacecraft trajectory design techniques using resonant orbits," Purdue University, 2018.

[30] A. E. Roy and M. W. Ovenden, "On the occurrence of commensurable mean motions in the solar system: The mirror theorem," *Monthly Notices of the Royal Astronomical Society*, vol. 115, pp. 296–309, 1955.

[31] E. M. Zimovan, K. C. Howell, and D. C. Davis, "Near rectilinear halo orbits and their application in cis-lunar space.," in *3rd IAA Conference on Dynamics and Control of Space Systems, People's Friendship University of Russia, (RUDN University), Moscow, Russia*, May 30th – June 1st 2017.

[32] J. D. Hadjidemetriou and S. Ichtiaroglou, "A qualitative study of the kirkwood gaps in the asteroids," *Astronomy and Astrophysics*, vol. 131, pp. 20–32, 1984.

[33] H. Poincaré, *Les Méthodes Nouvelles de la Mécanique Céleste*. Gauthier-Villars, 1892, vol. 1.

[34] E. M. Zimovan, "Characteristics and design strategies for near rectilinear halo orbits within the earth-moon system," Purdue University, 2017.

[35] Jet Propulsion Laboratory. (2022). "Navigation and ancillary information facility – spice date," [Online]. Available: https://naif.jpl.nasa.gov/naif/data.html.